IMPACT ON WIND TURBINE BLADE DESIGN AND AERODYNAMIC PERFORMANCE USING INTEGRAL VORTEX GENERATORS

By

Amool A Raina

Submitted to the graduate degree program in Aerospace Engineering and the Graduate Faculty of the University of Kansas School of Engineering in partial fulfillment of the requirements for the degree of Doctor of Philosophy.

Committee:

_____

Dr. Saeed Farokhi, Chairperson

_____

Dr. Ray Taghavi, Committee Member

_____

Dr. Shawn Keshmiri, Committee Member

_____

Dr. Zhongquan Zheng, Committee Member

_____

Dr. Mario Medina, Committee Member

Date Defended: _____

The Thesis Committee for Amool A Raina certifies that this is the approved version of the following dissertation

IMPACT ON WIND TURBINE BLADE DESIGN AND AERODYNAMIC PERFORMANCE USING INTEGRAL VORTEX GENERATORS

Committee:

_____

Dr. Saeed Farokhi, Chairperson

_____

Dr. Ray Taghavi, Committee Member

_____

Dr. Shawn Keshmiri, Committee Member

_____

Dr. Zhongquan Zheng, Committee Member

_____

Dr. Mario Medina, Committee Member

Date Defended: _____

Dedicated to Mom and Dad

Acknowledgments

I would like to take this opportunity to thank my advisor and mentor Dr. Saeed Farokhi for his support and guidance throughout my Masters and Doctoral work. Without his support, I would not have achieved this academic milestone. It has been an honor to work under his guidance. Through the past seven years that flew by, Dr. Farokhi has been a source of constant motivation, helping and guiding me through the tough phases of my life. Very few people are fortunate to find a guru who can teach and enlighten ones approach towards life. I consider myself lucky to be Dr. Farokhi's student and I am sure that for many years to come, I will continue to seek his advice and guidance on matters both personal and professional.

I would also like to thank Dr. Ray Taghavi for his constant support and help during my doctoral work. I would also like to thank Dr. Shawn Keshmiri, Dr. Charlie Zheng and Dr. Mario Medina for their timely contributions towards my research dissertation.

I would like to thank Dr. Kyle K Wetzel, for giving me the opportunity to work at Wetzel Engineering Inc. I appreciate all the hard work and efforts taken by you to educate me in the field of Wind Energy. Working with you has always been a wonderful experience. Under your tutelage, over the past years, I have not only enhanced my theoretical knowledge but have also developed my professional skills to a great extent.

I would also like to thank Dr. Wang and the Aerospace Engineering department staff for their support concerning help regarding financial and administrative tasks.

I would also like to thank my colleagues Ryan Barnhart, Alex Tran, Alejandra Escalera and others at Wetzel Engineering Inc. for the long hours of discussions that I have had with them. Their inputs and ideas have been valuable to my analysis.

My friends and family have always played a key role in my success. I would like to take this opportunity to thank my friends Dr. Himanshu Dande, Dhaval Mysore, Chandra Tourani and Anirudh Pochiraju for their help and support throughout my graduate education. I would also like to thank Dr. Shiban and Dr. Nancy Raina for their continuous guidance and words of encouragement.

I would also like to express my gratitude towards my colleagues and friends at the University of Kansas for making my stay in Lawrence a memorable one.

Finally I would like to thank my parents and in-laws, my brother and my lovely wife for their love, affection and patience which was very crucial to the completion of my dissertation.

Abstract

This dissertation is aimed at understanding the impact on performance, loads and cost using integral vortex generators on wind turbine blade designs. In order to investigate the possibility of this new design space, an optimization analysis is carried out. Three configurations are designed as a part of this dissertation. The current phase of work consists of creating a baseline blade that spans 56m in length. In order to determine the effectiveness of vortex generators on airfoils used on the 56m blade design, a verification and validation study of CFD tools is carried out. For this exercise, the LS(1)-0417MOD airfoil is used. STAR CCM+ software is used for performing the CFD analysis on the clean and vortex generator configurations of the LS(1)-0417MOD airfoil. Satisfactory results are obtained from the CFD analysis. A CFD analysis of a 47% thick airfoil is performed as well. This data has been used in the design of the 56m blade. Further, finite span airfoils incorporating vortex generators for the FB47 and NACA63621 airfoils are analyzed. This data is then used to evaluate the improvement of aerodynamic performance of the add-on 56m blade configuration. Vortex generators are incorporated in the post design phase of the clean 56m blade design and the improvement in performance in recorded. It is observed that a 0.4% improvement in AEP along with a 1.2% increase in loads and 2.13% increase in cost of energy is seen. Thereafter, the optimization and design of the 56m blade with integral vortex generators is carried out. Finally a full blade design of the 56m blade with integral vortex generators is carried out and the key performance metrics are recorded. A 1.7% increase in aerodynamic performance is recorded for the integral vortex generator case. This increase in performance also results in a 15.3% increase in blade root bending

moment. However, a reduction in the total cost of energy is obtained as compared to the baseline blade design.

Table of Contents

List of Tables

List of Figures

Nomenclature

Latin Letters

A ..... Area ..... m^2

a ..... Speed of sound ..... ms^{-1}

$\dot{m}$ ..... mass flow rate ..... kgs^{-1}

p ..... Static Pressure ..... kPa

R ..... Universal Gas Constant ..... $J\ kmol^{-1}\ K^{-1}$

U ..... Velocity ..... ms^{-1}

a ..... Axial induction factor ..... ~

a' ..... Angular induction factor ..... ~

C_p ..... Coefficient of power ..... ~

c_l ..... Coefficient of lift ..... ~

c_d ..... Coefficient of drag ..... ~

η ..... Efficiency ..... ~

F_T ..... Thrust Force ..... N

r ..... Radius of annular stream tube ..... m

R ..... Radius of rotor ..... m

Q ..... Rotor Torque ..... Nm

F_N ..... Normal force ..... N

F_D ..... Incremental drag force ..... N

Re ..... Reynolds Number ..... ~

u ..... Velocity ..... ms^{-1}

E ..... Energy ..... J

Greek Letters

α ..... Angle of Attack ..... deg

ω ..... Angular speed imparted to rotor ..... rpm

Ω ..... Rotor angular speed ..... rpm

ρ ..... Density ..... kgm^{-3}

ϕ ..... Angle of relative wind ..... deg

θ_p ..... Section pitch angle ..... deg

$\theta_{p,0}$ ..... Blade pitch angle ..... deg

θ_T ..... Section twist angle ..... deg

λ ..... Tip speed ratio ..... ~

τ ..... Shear Stress ..... Nm^{-2}

Abbreviations and Acronyms

2D,3D ..... Two or Three Dimensional ..... ~

AOA ..... Angle of Attack ..... deg

BEM ..... Blade Element Momentum ..... ~

CFD ..... Computational Fluid Dynamics ..... ~

HAWT ..... Horizontal Axis Wind Turbine ..... ~

NREL ..... National Renewable Energy Laboratory ..... ~

RANS ..... Reynolds-Averaged Navier-Stokes ..... ~

SA ..... Spalart-Allmaras ..... ~

SST ..... Shear Stress Transport ..... ~

VAWT ..... Vertical Axis Wind Turbine ..... ~

NACA ..... National Advisory Committee on Aeronautics ..... ~

FB .....Flatback .....~

IEA .....International Energy Agency.....~

VG .....Vortex Generator.....~

IVG.....Integral Vortex Generator .....~

DSV ..... Dynamic Stall Vortex.....~

OEM .....Original Equipment Manufacturer.....~

COE .....Cost of Energy.....~

AEP..... Annual Energy Production.....~

FEA.....Finite Element Analysis.....~

LaRC.....Langley Research Center.....~

NWTC. .....National Wind Technology Center .....~

WEI..... Wetzel Engineering Inc.....~

FF. .....Fiber Failure.....~

IFF. ..... Inter Fiber Failure .....~

IEC.....International Electrotechnical Commission.....~

1. Introduction

Renewable energy is defined as energy which is directly or indirectly produced from inexhaustible natural sources like sun, wind, tides, rain, etc. [1]. As per the IEA World Energy Outlook [2], the projected growth of the world's primary energy needs is expected to be around 56% between 2005 and 2030. The rate of growth per year is estimated to be 1.8%. Although fossil fuels continue to be a dominant source of primary energy; with growing concerns over critical environmental issues, the focus is now being turned to the development and use of renewable energy as an alternative source to meet the growing energy demands across the globe.

The use of wind turbines as a source of energy production can be dated back to the early nineteenth century. In the early 1900's, companies like Brush (USA) and LaCour (Denmark) developed 12kW DC windmill generators for electricity production. In the twentieth century, Smith-Putnam wind turbine built in 1941 became the first operational full-span pitch control machine whose steel rotor blades spanned 53m in diameter [3]. However this machine failed catastrophically in 1945 due to a structural failure in the spar of the blade. In years to come, with rising fuel prices and the need for alternative sources of energy led to significant development in the wind turbine industry. Wind turbines can be classified into two main categories namely, Horizontal Axis Wind Turbines (HAWT's) and Vertical Axis Wind Turbines (VAWT's). These turbines can either be two bladed or three bladed depending on their design. In the present day, wind turbines range from small utility scale machines (~10kW- 750kW) to large MW sized machines [4]. The current global trends are leading more designers to push the envelope of wind turbine blade design towards large scale rotors of the order of 200m rotor diameter machines which can produce energy up to 10MW of power.

1.1. Wind Energy – Current Global Developments

With the development of unique tools for analysis and better manufacturing capabilities, wind turbine designers are now focusing their efforts towards larger wind turbine blades. By the end of 2015, 147,771MW of power was produced across Europe with most of the power being produced by MW scaled off-shore wind turbines [5]. On the other hand by the end of December 2014, the U.S. wind industry now totals 65,879 MW of cumulative wind capacity. The U.S. wind industry has added over 35% of all new generating capacity over the past 4 years, second only to natural gas, and more than nuclear and coal combined. Today, U.S. wind power capacity represents more than 20% of the world's installed wind power. In Asia, China was the largest market in 2010 with 114,604 MW of installed wind power generation capacity. Other countries like India, Japan and South Korea have recorded installed capacities of 22,465 MW, 2,794 MW and 610 MW respectively. [6]

Wind energy is a low density source of power. In order to achieve maximum efficiency from these machines, it is important to understand the factors affecting the aerodynamic performance of these wind turbine blades. In the recent years, the trends of the present industry have shifted from solely focusing on new turbine technology to studying and implementing strategies to improve (to recover lost aerodynamic performance in some cases) performance and lengthen the life of their wind assets. One of the routes taken to recover lost performance is to adapt readily available aviation technology and use it on wind turbine blades. For e.g. stall strips, riblets, vortex generators, plasma jets, microtabs, etc. are some the proposed technologies to be used on ageing or even new wind turbine blades. The problem with this approach

is that not all factors are taken into account while using such technology on wind turbines i.e. the impact of dynamic inflow (pitching and plunging motion, turbulence levels during operation) on these devices, the impact on overall system loads are not taken into consideration.

The objective of this work is to explore the existing design space as well as develop a new design space in multi-disciplinary system optimization of wind turbine blades. Specifically, the feasibility of introducing vortex generators at different stages in the wind turbine design process is studied. The impact on performance and cost will be addressed in a multi-disciplinary approach as a part of this dissertation. The proposed work has been subdivided into three major tasks. Task 1 includes the development of an optimization code which is used for the optimization and design of a 56m blade. Task 2 looks at the verification and validation of an airfoil in steady and unsteady flow conditions. Once the methodology of CFD analysis has been verified, airfoils pertaining to the 56m blade will be analyzed with and without vortex generators. Task 3 consists of optimizing a 56m blade with integral vortex generators (introduced during the design process) and comparing the design to the baseline (clean) configuration and upgraded design (post-design VGs added) configuration. Additional work pertaining to the characterization of flatback airfoils with integral vortex generators is considered as a part of this analysis.

2. Aerodynamics of Wind Turbines

This section treats the operation of Horizontal Axis Wind Turbine (HAWT) machines. The conversion of wind energy to electricity is not obtained directly but through several mechanical systems which convert the extracted wind energy into mechanical energy and thereafter into electrical energy. In airscrew theory, lift force is considered as the main driving force which is then converted into mechanical torque. The shaft transfers the torque from the blades to the generator which is finally output as electric energy. There are three types of wind turbine setups namely [7]:

- A classical wind turbine with gearbox. A gearbox with typically 3 steps connects the rotor shaft to the generator shaft, which is directly connected to the electrical grid and therefore has a fixed rotational speed.
- A turbine without a gearbox i.e. the axle is directly connected to the generator. This concept is more popular as compared to the earlier concept since this concept can be incorporated with a large multi-pole generator which allows the shaft to rotate with the low speed of the rotor.
- A hybrid concept which combines the ideas of the previous two concepts. This concept is usually realized by using a small generator and a step- gearbox for matching the requested angular speed.

Apart from the mechanical concepts mentioned above, wind turbines can be classified into two major types. They are:

1. Fixed-Speed Wind Turbines
2. Variable-Speed Wind Turbines

Fixed-Speed Machines:

Fixed-speed machines are generally referred to as machines which operate with a fixed rpm. These machines usually incorporate a direct drive setup with no components for variable transmission i.e. their speed cannot be regulated given a specific operating condition.

Variable-Speed Machines:

A variable-speed wind turbine is defined as a machine that has the capability to operate at different rotor speeds in order to achieve the maximum performance from the machine. The setup for variable-speed wind turbines is generally costlier as compared to fixed-speed machines since they have additional components that are used to regulate the rotor speed. Hence a variable-speed wind turbine is much more effective in terms of power capture as compared to a fixed-speed machine.

Wind turbines usually operate in a given range of wind speeds. The startup velocity also known as cut-in speed is about 3-5m/s. As the wind speed increases, the power production increases till the rated power is reached. After having reached the rated power at a given wind speed, the power has to be regulated for higher wind speeds. At a fixed value of wind speed known as cutoff which is typically around 25m/s, the turbine stops. For wind speeds above cutoff, the turbine is kept in parked position i.e. the rotor is left stationary so as to avoid high thrust loads. Until the rated power is reached, the wind turbine is ideally operated so as to capture maximum energy. In order to optimize the energy capture, different control systems schemes are implemented namely stall control and pitch control. These two systems are briefly discussed.

- Stall control:

  Stall control describes a passive method of controlling the power output of a wind turbine. The blades are designed in such a way that they work with optimum angle of attack at the average wind speeds, whereas at higher speeds, the flow angle increases which leads to separation and hence an increase in drag accompanied with a significant reduction in lift. The exceeding loads are completely dissipated and no possible control on the efficiency can be achieved in the low-speed operating range. It should be noted that no rotational speed control is available in this model.

- Pitch control

  In a pitch controlled machine, the blades can be pitched, i.e. turned around their axes by means of electrical motors. In this case, the flow angle can be adjusted so as to increase the net power production of the machine. With new age technology in place, these machines now have the capability of individual pitch control.

2.1 Aerodynamic Models

Over the last two decades, the size of commercial wind turbines has grown enormously from approximately 750kw to 5MW as shown in Figure 1. With higher power ratings, the focus of the wind industry is slowly shifting towards offshore development of these large machines. On the technological front, wind turbine design has evolved rapidly over the last 25 years. New computational techniques are now used to study the flowfield characteristics and predict the performance of these machines. As a result of improved simulation techniques, wind turbines are now more reliable, cost effective and quieter. However, the cost effectiveness of MW-scaled wind turbines still remains questionable.

There are several aerodynamics analysis techniques which are presently used in the wind turbine industry today. Some of the models used by wind turbine blade designers are:

- Blade Element Momentum theory (BEM)
- Lifting line, panel and vortex-lattice methods
- Actuator disk methods
- Navier-Stokes solvers (in CFD-based approach)

In this document, two main methodologies namely, BEM and Navier-Stokes solvers (CFD) are discussed.

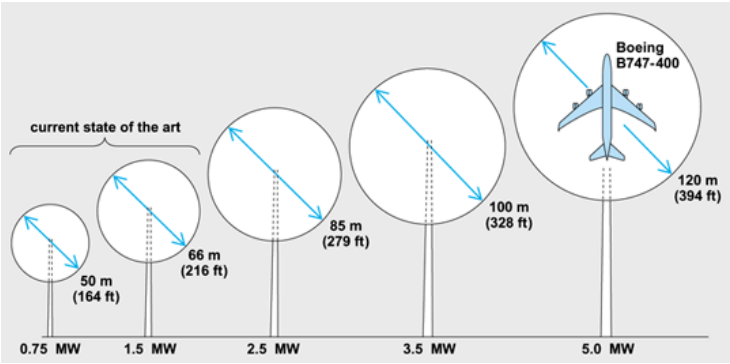

Figure 1: Representative dimensions and power rating of wind turbines [8]

2.2 One Dimensional Momentum Theory

In 1926, Betz developed a simple model which was used to determine the power from an ideal turbine rotor along with the thrust force acting on the rotor. This model was based primarily on the linear momentum theory that was developed in the early 1900's to predict the performance of propellers [4].

The analysis for this theory was based on a control volume approach. In a defined control volume as shown in Figure 2, the boundaries are defined as the surface of a stream tube and two cross sections were taken upstream and downstream of the

rotor. In this case, infinite number of blades were assumed i.e. the rotor was modeled as a uniform "actuator disk" which creates a discontinuity in flow properties, e.g., static pressure and swirl, upstream and downstream of itself. The infinite number of blades are assumed that creates an axisymmetric flow downstream of the rotor. The flowfield was assumed to be steady (in the rotor frame of reference), homogenous and incompressible. No frictional drag was assumed during the analysis. Also a uniform thrust force acting over the rotor disk was assumed (similar to propeller theory) [4].

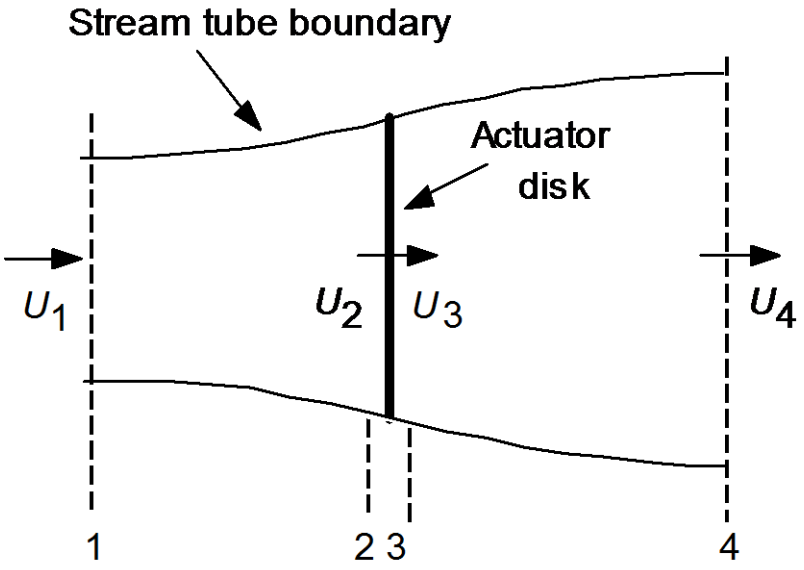

Figure 2: Basic control volume assumed for linear momentum theory [4]

Using the principles of conservation of linear momentum and applying them to the control volume, the net force on the actuator disk is calculated. That force is equal and opposite to the thrust, F_T, which is the force of the fluid on the wind turbine. This thrust is approximated as equal and opposite to the change in momentum of the air stream as given by equation 1.

$$F_T = U_1\left(\rho AU\right)_1 - U_4\left(\rho AU\right)_4 \tag{1}$$

Using equation 2, we calculate the thrust. Since the thrust is positive, the velocity downstream of the rotor is less than that of the freestream value. Since no external work is done on the fluid on either side of the rotor, we can use Bernoulli's principle for the two control volumes upstream and downstream of the rotor. Equation 3 and 4 give the relations upstream and downstream of the rotor.

$$F_T = \dot{m}\left(U_1 - U_4\right) \tag{2}$$

$$p_1 + \tfrac{1}{2}\rho U_1^{\,2} = p_2 + \tfrac{1}{2}\rho U_2^{\,2} \tag{3}$$

$$p_3 + \tfrac{1}{2}\rho U_3^{\,2} = p_4 + \tfrac{1}{2}\rho U_4^{\,2} \tag{4}$$

As a part of this calculation, we assume that the pressure far upstream and downstream are equal i.e. $p_1=p_4$ as well as the axial velocity on either side of the rotor are assumed to be the same i.e. $U_2=U_3$ following the continuity of incompressible fluid. The thrust can also be expressed as the net pressure force acting on the actuator disk; namely

$$F_T = A_2\left(p_2 - p_3\right) \tag{5}$$

Using equations 3-5, we get

$$F_T = \tfrac{1}{2}\rho A_2\left(U_1^{\,2} - U_4^{\,2}\right) \tag{6}$$

From these equations, we calculate the velocity U_2 at the disk to be the average of the far up- and down-stream of the rotor, i.e.

$$U_2 = \frac{U_1 + U_4}{2} \tag{7}$$

To simplify the calculations, we define the fractional decrease in wind velocity between the freestream and the rotor plane as the axial induction factor 'a' as given in equation 8.

$$a = \frac{U_1 - U_2}{U_1} \tag{8}$$

$$U_2 = U_1(1-a) \tag{9}$$

$$U_4 = U_1(1-2a) \tag{10}$$

Using the above relations and substituting the values for the axial induction factor in the equation for power we get,

$$P = \frac{1}{2}\rho A_2\left(U_1^{\,2} - U_4^{\,2}\right)V_2 = \frac{1}{2}\rho A_2 U_2\left(U_1 + U_4\right)\left(U_1 - U_4\right) \tag{11}$$

$$P = \frac{1}{2}\rho A U^3 4a(1-a)^2 \tag{12}$$

The coefficient of power is then calculated using the definition in equation 13 and expressed in terms of induction factor in equation 14.

$$C_P = \frac{P}{\frac{1}{2}\rho U^3 A} \tag{13}$$

$$C_P = 4a(1-a)^2 \tag{14}$$

The maximum C_p is defined by differentiating the RHS of equation 14 and setting it to zero. The maximum, also known as ***Betz limit*** is equal to 0.5925 i.e. only 59.25% of energy from the stream can be extracted as rotor energy. The total output power is then calculated using equation 15

$$P_{out} = \frac{1}{2}\rho A U^3 \left(\eta_{mech} C_P\right) \tag{15}$$

Having calculated the power, we can also calculate the forces acting ~~in~~ on a wind turbine blade using the principles of conservation of momentum. We consider the axial and angular induction factors to be functions of the radius of the disk, r as shown in Figure 3.

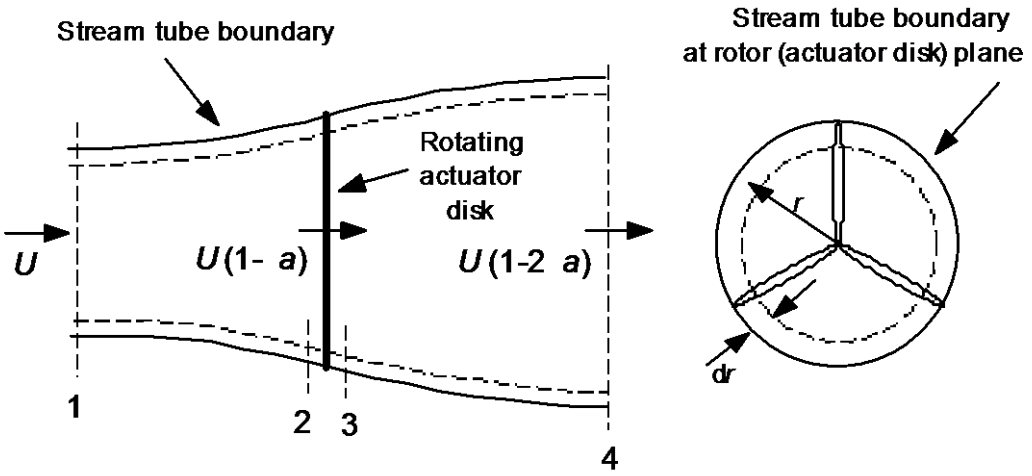

Figure 3: Schematic representation of the control volume used for analysis [4]

Applying the conservation of linear momentum to the control volume of radius r and thickness d*r*, we get the differential thrust and torque as given by equations 16-17 [4].

$$dF_T = \rho U^2 4a(1-a)\pi r dr \tag{16}$$

$$dQ = 4a'(1-a)\rho U \pi r^3 \Omega \, dr \tag{17}$$

2.3 Blade Element Theory

The forces acting on the blade are mainly caused due to lift and drag forces. These lift and drag forces are a function of the angle of attack as seen by every section of the blade during its operation. In blade element theory, we assume that the blade consists of N sections. Also, each of these elements is assumed to have independent aerodynamic characteristics i.e. there is no interaction between two elements. Figure 4 shows a representation of the Blade Element theory.

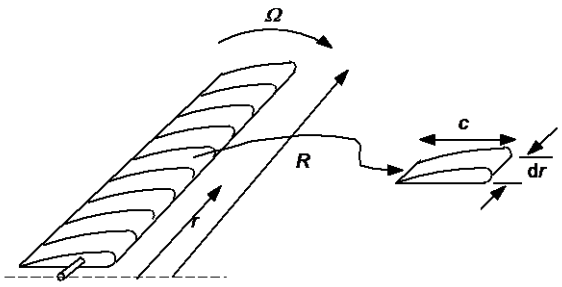

Figure 4: Schematic representation of Blade Element Theory [4]

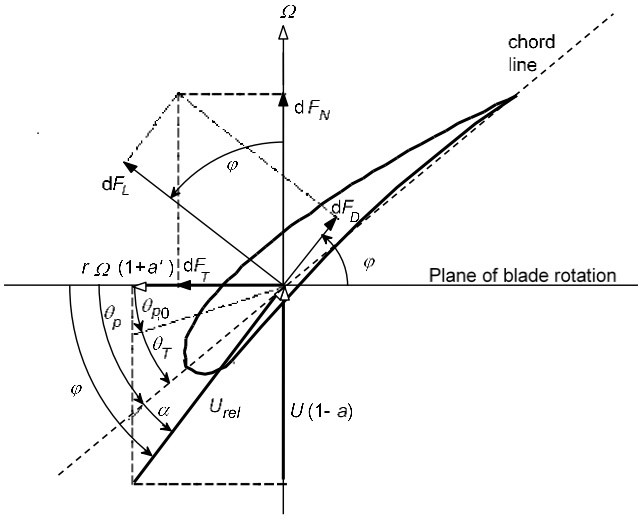

Figure 5: Sectional Representation of Blade Geometry [4]

Using the definition sketches, we get the following relations as given by equations 18-23 [4].

$$\tan\varphi = \frac{U\left(1-a\right)}{\Omega r\left(1+a'\right)} = \frac{1-a}{\left(1+a'\right)\lambda_r} \tag{18}$$

$$U_{rel} = U\left(1-a\right)/\sin\varphi \tag{19}$$

$$\mathrm{d}F_L = C_l \tfrac{1}{2}\rho U_{rel}{}^2 c\ \mathrm{d}r \tag{20}$$

$$\mathrm{d}F_D = C_d \tfrac{1}{2}\rho U_{rel}{}^2 c\ \mathrm{d}r \tag{21}$$

$$\mathrm{d}F_N = \mathrm{d}F_L\cos\varphi + \mathrm{d}F_D\sin\varphi \tag{22}$$

$$\mathrm{d}F_T = \mathrm{d}F_L\sin\varphi - \mathrm{d}F_D\cos\varphi \tag{23}$$

For a rotor with X number of blades, we calculate the normal force and the torque given by equations 24-25 [4].

$$dF_N = X \frac{1}{2} \rho U_{rel}^{\ 2} \left(C_l \cos\varphi + C_d \sin\varphi \right) c dr \tag{24}$$

$$dQ = X \frac{1}{2} \rho U_{rel}^{\ 2} \left(C_l \sin\varphi - C_d \cos\varphi \right) cr dr \tag{25}$$

These equations are used to determine the loading on the blades and hence serve as a measure for performance calculations during wind turbine blade design. In the present day, there are several codes available to predict the performance of wind turbines based on the above methodology. For this dissertation, in-house developed and commercial codes like WT-Perf were used for estimating the energy capture for a given blade design.

2.4 CFD Techniques

Computational Fluid Dynamics is based on the fundamental conservation laws governing fluid flow, i.e., conservation of mass, momentum and energy. Computational Fluid Dynamics has been used as a method for fluid flow simulation extensively in past century for predicting and understanding the flow physics for various complex problems. CFD however has not been a very popular technique in the field of wind energy. This is primarily due to the rapid rate of development and the dependence of wind turbine engineers on simple prediction methods like BEM. However, in the recent past, the scenario has changed with major international companies and research labs employing the techniques of CFD for prediction and performance estimation of wind turbine blades. The approach of CFD has been used primarily for small blades. In this dissertation, CFD is used to generate and study the performance parameters for airfoil sections used for the design of the 56m blade.

The equations representing conservation of mass momentum and energy are shown in tensor notation in equations 26-28.

$$\frac{\partial \rho}{\partial t} + \frac{\partial \left(\rho u_j \right)}{\partial x_j} = 0 \tag{26}$$

$$\frac{\partial \left(\rho u_i \right)}{\partial t} + \frac{\partial}{\partial x_j} \left(\rho u_i u_j + \partial_{ij} p - \tau_{ij} \right) = 0 \tag{27}$$

$$\frac{\partial \left(\rho E \right)}{\partial t} + \frac{\partial}{\partial x_j} \left(\rho H u_j + q_j - \tau_{ij} u_i \right) = 0 \tag{28}$$

In the above equations, ρ is the fluid static density, p is the static pressure, u_i is the velocity component, E is the total energy per unit volume which is equal to the sum of total internal energy and kinetic energy per unit volume, H is total enthalpy per unit volume which is equal to the sum of total internal energy and pressure-volume work, τ_{ij} is the stress tensor and q_j is the heat flux vector. Owing to the range of operational Reynolds number, flow may exist either in laminar or turbulent state. The solution approach towards both these states depends on the modeling of the transport equations. Flows in the laminar regime are completely described by the continuity and momentum equations. On the other hand, turbulent flows are characterized by the existence of random fluctuation in the fluid motion that give rise to “apparent stresses” in the fluid. Since turbulent flow is mainly associated with the presence of different length scales, different turbulence models are developed and used to accommodate these varying length scales. In addition to the wide range of length and time scales and the associated computational cost, the governing equations of fluid dynamics contain a non-linear convection term and a

non-linear and non-local pressure gradient term. These coupled nonlinear differential equations must be solved simultaneously with the appropriate boundary and initial conditions. [9] Some of the commonly used turbulence models are Spalart-Allmaras (S-A), k-ε 2-equation model, k-ω 2-equation model and 7 equation RANS model. Based on the several available models, the nature of the problem and guidance from references from existing literature in wind turbine simulation, k-ω SST turbulence model was chosen. The choice of turbulence model is further discussed in the analysis section.

2.4.1 k-ω SST

In the k- ω turbulence model, the equation of the specific rate of dissipation of turbulent kinetic energy is solved together with the transport equation of the kinetic energy. The Shear Stress Transport model (SST) was developed by Menter to effectively blend the accurate near wall flow formulation of the k- ω model with the free stream independence of the k- ε model in the far field. The SST k- ω turbulence model is quite similar to the k- ω turbulence model except that it includes several features that make the SST model much more robust for a wide range of flow regimes like adverse pressure gradient flows, airfoils, transonic shock waves, etc. Some of the added features as compared to the standard k-ω model are the inclusion of a blending function so that the model can have the properties of both k-ω and k-ε models depending on the near field or farfield regions of the computational domain. The SST model also incorporates the definition of the turbulent viscosity so that it is modified to account for the transport of the turbulent shear stress. The SST k-ω model equations are given as follows [9]:

$$\frac{\partial}{\partial t}(\rho k)+\frac{\partial}{\partial x_i}(\rho k u_i)=\frac{\partial}{\partial x_j}\left(\Gamma_k \frac{\partial k}{\partial x_j}\right)+\tilde{G}_k-Y_k+S_k \quad (29)$$

$$\frac{\partial}{\partial t}(\rho \omega)+\frac{\partial}{\partial x_i}(\rho \omega u_i)=\frac{\partial}{\partial x_j}\left(\Gamma_\omega \frac{\partial \omega}{\partial x_j}\right)+G_\omega-Y_\omega+S_\omega+D_\omega \quad (30)$$

Where,

$\tilde{G}_k$	=	represents the generation of turbulence kinetic energy due to mean velocity gradients
G_ω	=	represents the generation of ω
Y_k , Y_ω	=	represent the dissipation of k and ω
S_k , S_ω	=	user defined source terms
Γ_k , Γ_ω	=	represent the effective diffusivity of k and ω
D_ω	=	represents the cross diffusion term
ω	=	Specific dissipation rate

3. Literature Review

3.1. Optimization and Design Techniques for Wind Turbine Blades

Several aero-structural optimization techniques have been developed for wind turbine blade optimizations. These include models developed by DOE-NREL [10], which consist of aero-structural optimization techniques. However, this code is currently being developed and consists of high-fidelity models that are computationally expensive. Other models developed include genetic algorithm-based optimization routines and other such models, which are sensitive to the input design parameters. A final feasible design however may not result from such an optimization analysis. [11-13]. So far, no one has evaluated the possibility of adding vortex generators into the multi-disciplinary optimization and design phase of wind turbine blades. During a conversation with one of the leading OEMs, it was discovered that vortex generators are incorporated immediately after the manufacturing phase but not during the optimization or design phase of the blade [14]. The next section reviews the literature on vortex generators specifically in the context of available data for verification and validation of CFD tools with existing steady and dynamic flow wind tunnel test data.

3.2. Vortex Generators – Steady Inflow Characterization

Due to energy redistribution associated with instability of boundary layers and their potential separation, flow control remains an important area of research for many technological applications [15-16]. Vortex generators – specifically their performance and flow characteristics – have been studied extensively in a steady environment [15-44]. This area of research was initiated in the aerospace domain and in recent years has gradually migrated into the wind energy domain. Wind turbine airfoils designed

by NREL have been tested with vortex generators [42]. Also smart vortex generators have been studied and tested mainly for aircraft applications. Smart VGs, however, have not found their place in wind turbine applications yet. [43-44] Different combinations of flow control devices have been empirically studied with an aim of increasing the performance of wind turbine systems [45]. Impact of turbulent flows dominated by curvature effects has been studied in detail by Farokhi, et.al. [46-47]. Also, propeller theory has been addressed in reference 48. Conventional, vane-type, passive vortex generators (VGs) with device height, h; on the order of the boundary-layer thickness, δ; have long been used to control flow separation by increasing the near-wall momentum through the momentum transfer from the outer (freestream) flow to the wall region. First introduced by Taylor [16] in the late 1940s, these devices consisted of a row of small plates or airfoils that project normal to the surface and are set at an angle of incidence, b; to the local flow to generate an array of streamwise trailing vortices. These conventional VGs have been used to delay boundary-layer separation [17], to enhance aircraft wing lift [18, 19], to tailor wing-buffet characteristics at transonic speeds [19, 20], to reduce after-body drag of aircraft fuselages [21], and to avoid or delay separation in subsonic diffusers [22]. A wide variety of conventional VGs are in use, and numerous aircraft successfully employ them for separation control. Many aerodynamics applications, however, use these relatively large (δ-scale) VGs to control a localized flow separation over a relative short downstream distance. These VGs may incur excessive residual drag through conversion of aircraft forward momentum into unrecoverable turbulence in the aircraft wake. Therefore, a more efficient or optimized VG design could be achieved

for certain applications where the separation location is fairly fixed and does not require covering a large downstream distance by these devices. In the early 1970s, Kuethe [22] developed and examined non-conventional wave-type VGs with h/δ of 0.27 and 0.42 that use the Taylor–Goertler instability to generate streamwise vortices within the boundary layer. These low-profile devices successfully reduce the intensity of acoustic disturbances in the wake region by suppressing the formation of the Karman vortex street and reducing the area of velocity deficit in the wake [22]. From research performed in the late 1980s, an exploratory separation control study by Rao and Kariya [20] suggests that submerged VGs with $h/\delta \leq 0.625$ have the potential of exceeding the performance of conventional VGs with $h/\delta \sim 1$; due to the much lower device (or parasitic) drag. Subsequently, several researchers since then show that by using low-profile VGs with the device height only a fraction of the conventional vane-type VGs, these generators (i.e. $0.1 \leq h/\delta \leq 0.5$) can still provide sufficient wall-ward momentum transfer over a region several times their own height for effective flow separation control. In addition to lower device drag, the low-profile VGs offer other advantages when compared with the larger conventional VGs due to their compact size, such as allowing the devices to be stowed within the wing when not needed (e.g., on slotted flaps) and lower radar cross section. Several different configurations of VGs have been analyzed over the years. A brief list of these VGs and their characteristics are presented in table 1.

3.3. Performance Characterization of Airfoils in Dynamic Inflow Conditions

Dynamic stall is a nonlinear phenomenon that occurs on lifting surfaces such as airfoil in unsteady motion with angles of attack exceeding post stall. The aerodynamic forces and moments overshoots are usually associated with the

formation of an energetic dynamic stall vortex (DSV), which first appears at the leading edge of the lifting surface (in this case it is an airfoil) and travels along the lifting surface until it separates from the airfoil at the trailing edge. However, after the DSV detaches from the airfoil and moves into the wake, the lift decreases abruptly. Some researchers relate these overshoots to the delay of the separation rather than the formation of the dynamic stall vortex [34]. The unsteady aerodynamic characteristics resulting from the rate of change in angle of attack and can be significantly different from those of the static case. Under oscillatory or transient motion, the vortices which are created at the leading edge change strength and position as a function of time-varying angle of attack. Therefore, the location of vortex breakdown, if it occurs, will likewise become time dependent. These changes in the vortex flow do not take place instantaneously with the dynamic motion, due to the convective time lag of adjusting flowfield. Over the past three decades, the dynamic stall phenomenon has been investigated through experimental and numerical approaches and a significant progress has been made to understand the general features of the dynamic stall. Examples of experimental and numerical works can be found in references 34 - 40. These numerical studies have analyzed the dynamic stall phenomenon in laminar and turbulent flow conditions. Until recently, most of these studies were concentrated in the thin airfoil regime (< 18% t/c airfoils). However, recently researchers have investigated the flow characteristics around thick flatback airfoils operating in a dynamic inflow condition [41].

3.4. Vortex Generators – Dynamic Inflow Characterization

Janiszewska performed experimental studies to characterize the flow around a 3D airfoil and wing (details provided below) in the Ohio State Wind tunnel [45]. The

author's study is unique in the detailed documentation of the behavior of an oscillating finite wing (or turbine blade) together with the related steady-state in both two-dimensional and three-dimensional model configurations. The pressure distributions across the span provide information on the effect of the tip vortex in the different types of flows. In addition, the influences of vortex generators as passive boundary-layer control devices were also investigated. The main purpose of this study was to investigate a three dimensional wing or wind turbine configuration with and without vortex generators for both steady state and unsteady flows. The goal of this study was to capture the flow characteristics in a dynamic inflow environment since the data for such a problem is not available in literature. The numerous pressure distributions obtained across the span provide an insight into the flow characteristics around a three dimensional airfoil model. The data available in the literature generally do not contain pressure distributions, while those that are included are very limited and usually do not include sufficient spanwise data making the validation of the computational codes difficult. The current tests carried out by the author provide pressure data for both baseline two dimensional and three dimensional model configurations, i.e. clean model condition without roughness or vortex generators. The airfoil model for this study was designed as a simplified wing, with no twist and a constant chord to isolate the 3D effects from the more complicated flow fields of a general wing. In this study a multitude of different vortex generators shapes were tried in order to increase the maximum lift coefficient with a minimum drag penalty and to control the hysteresis loop in unsteady flows. Another part of the author's research dealt with the surface degradation of the wind turbine blades and wings due

to insect accumulation or age of the surface, this data are mostly only available for small grit strips (like zigzag tape trip strips) but not for a full severe contamination. Both types of data, with slight and severe roughness are required to understand the effect of grit on the aerodynamic characteristics especially after the vortex generators are applied to the surface of the wings. The surface roughness was simulated for these experiments were reproduced from an actual pattern which occurred on a wind turbine in the field. The main focus of the author's work is unsteady flow characteristics of the 3D wing section with both the vortex generators and surface roughness. The data presented in the literature are mostly limited to 2D configuration and also in type of oscillation, the amplitude, the frequency or the mean angle of attack.

All the experiments performed for this study confirm that it is difficult to predict the flow response to the vortex generators, especially in 3D unsteady flow. The author notes that only those vortex generators are presented in this work which gave very consistent results and were not affected as much by changes in position or shape.

3.5. Airfoil Details

The LS(1)-0417MOD airfoil, which is 17% thick, was used for these experiments. It is an unclassified NASA profile, designed for general aviation with an original design lift coefficient of 0.4. The trailing edge on this airfoil was modified to a finite thickness for easier manufacturing. Figure 1 shows the airfoil shape. This airfoil was tested in a dynamic inflow condition with and without vortex generators. [45]

3.6. Test Matrix used for experimental study

Many different shapes and sizes of vortex generators were designed and tested for this exploratory study in an attempt to find the correct ones for increasing lift and

decreasing drag. Based on the various configurations studied, the author chose four types of vortex generators. These are classified as type A and type B vortex generators. Type B vortex generator was derived from Type A vortex generator design.

The author generated a test matrix for her study and analyzed the flow parameters with and without vortex generators. The matrix highlighting her selections are provided in table 2. [45]

Table 1. Summary of research on boundary layer flow-separation control effectiveness for low profile VGs

				Most effective VG parameters examined				
Test Bed	**Type of Study**	**Flow Parameters**	**VG Type**	**h/δ**	**e/h**	**Δz/h**	**β(deg)**	**$\Delta X_{VG}/h$**
Backward-facing ramp	Wind Tunnel	U_∞ = 132ft/s	Doublets	0.1	13	8	25	20
Backward-facing ramp	Wind Tunnel	U_∞ = 132ft/s	Wishbones	0.2	3	4	23	10
Backward-facing ramp	Wind Tunnel	U_∞ = 132ft/s	Counter-rotating rectangular vanes	0.2	4	9	25	10
Backward-facing ramp	Wind Tunnel	U_∞ = 140ft/s	Co-rotating trapeziodal vanes	0.2	4	12	23	12, 19
Bump	Wind Tunnel	U_∞ = 20ft/s	Counter-rotating delta vanes Forward wedges	0.3	10	12	14	52
Shock Induced separation over flat plate	Wind Tunnel	M_∞ = 1.56	Doublets	0.36	10	6.4	19	50
Shock Induced separation over flat plate	CFD	M_∞ = 1.40	Ramps	0.33	14	6	14	50
Flat Plate	Wind Tunnel and CFD	U_∞ = 33ft/s to 98ft/s	Counter-rotating vanes	0.5	10		14	
			Forward wedge	0.5	10		14	
			Backward wedge	0.5	10		14	
			Single Vane	0.5	10		10, 20, 30, 45	
Flat Plate	Wind tunnel	U_∞ = 112ft/s	Single Rectangular vane	0.2	7		10, 16, 23	
Flat Plate	CFD	U_∞ = 112ft/s	Single trapezoidal vane	0.2	7		10, 23	

Table 2. Test Matrix used for experimental study

Parameter	Without Vortex Generators	With Vortex Generators
Re number	0.75m, 1m, 1.25m	1m
AOA range	-20° < α < 10° (2° steps) 20° < α < 40° (2° steps) 10° < α < 20° (1° steps)	0° < α < 30°
Amplitudes of pitch oscillation	± 5.5° , ± 10°	± 5.5° , ± 10°
Mean Angles for oscillations	8°, 14°, 20°	8°, 14°, 20°
Frequencies	0.6Hz, 1.3Hz, 1.8Hz	0.6Hz, 1.3Hz, 1.8Hz

Figure 6: LS(1)-0417MOD airfoil model

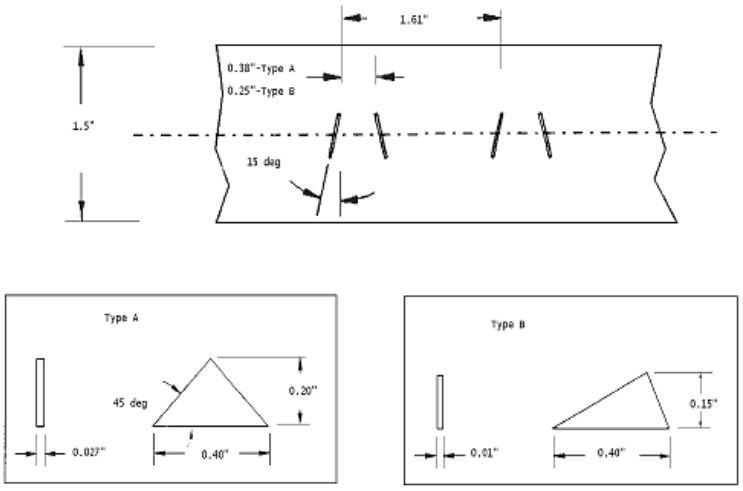

Figure 7: Type A and Type B Vortex Generators used for the study

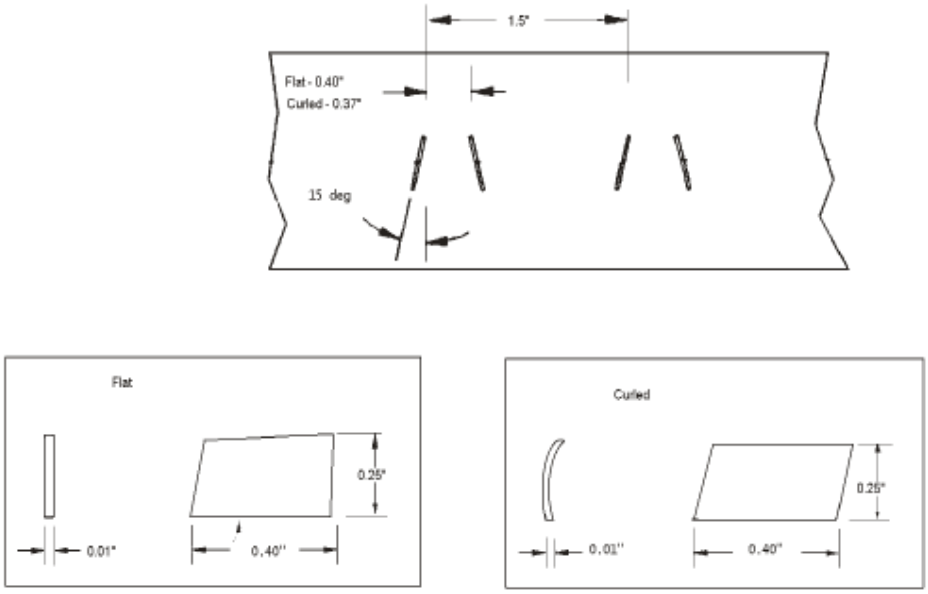

Figure 8: Flat and Curled Vortex Generators used for the study

3.7. Results and Conclusion from Wind Tunnel Testing

Below is the summary of the results and conclusions from Janiszewska's study [45].

The LS(1)-0417MOD airfoil model was tested under an extensive range of conditions in order to obtain aerodynamic characteristics for 2D and 3D flows with and without vortex generators and leading edge grit roughness in steady and unsteady conditions. The testing included angles of attack up to 30° for steady state tests and ±10°, ±5.5° pitch oscillations for 0.6, 1.3 and 1.8 Hz; all these tests were conducted for 0.75, 1.0, 1.25 million Reynolds numbers. The 2D tests, which were conducted as a baseline, had a lift coefficient increase of 12% due to the application of the Flat vortex generators when compared to the clean case, unfortunately the drag coefficient also increased by 25%. The lift coefficient with the vortex generators increased because of the "injection" of the higher momentum flow from the outer layer into the boundary layer. The mixing changes the thickness of the boundary

layer and the displacement thickness, therefore keeping the boundary layer attached at higher angles of attack. The main penalty of an increase in the lift is the increase in the drag due to the presence of the vortex generators. Even though the Curved vortex generators did increase the lift more than Flat vortex generators, the drag increase was too high for useful applications, especially at the low angles of attack. The author notes that the flow's response to the application of the vortex generators, their position or even their shape was difficult to predict, mostly due to our inability to "calculate" the outer flow influx into the boundary layer and the response of the boundary layer to that influx. From the tests performed for the 2D and 3D model conditions, the data show that placing the vortex generators between 0.07 and 0.15 of the chord increases the lift coefficient significantly while keeping the drag in check. The position of the vortex generators at 0.07 and 0.15 of the chord corresponds to the approximate location of the pressure peak at lower angles of attack. In placing the vortex generators close to the pressure peak allows the mixing of the injected outer flow and the boundary layer flow to occur before reaching the adverse pressure gradient. Additionally for 2D testing only shifting the vortex generators location rearwards by approximately 10% chord increased the lift coefficient to a higher value. However, these tests were predominantly for a 3D wing and the vortex generators' position was optimized for these tests. Therefore the location was kept forwards due to the lower lift curve slope for the 3D in comparison with the 2D cases.

The vortex generators were successful in increasing the lift coefficient at both the wall station and the tip station and shifting the stall angle of attack by approximately 5° to 7°. The Flat vortex generators increased the lift coefficient at the wall by 26% and at the tip by 33%. The vortex generators at the tip had to be positioned closer to the leading edge to

counteract the effect of the tip vortex. The application of the leading edge grit roughness produced a significant loss of lift and increase in drag, due to the added turbulence in the boundary layer. This type of grit roughness is very severe and especially at the leading edge of the airfoil it is almost the height of the boundary layer thickness. The decrease in lift could not be totally countered with the application of the vortex generators most likely due to their height. The author comments that it is possible that taller vortex generators would have more effect in mixing the outer flow, which is less affected by the roughness, with the boundary layer flow. The Flat vortex generators still increased the lift coefficient by approximately 25% for both the tip and wall stations and shifted the stall angle of attack by 5°. The slope of the 3D integrated data was always lower than the 2D cases, as theory predicted. The 3D integrated data did not reach the same lift coefficient as the 2D clean case, but with the application of the vortex generators the 3D integrated case surpassed the 2D case with vortex generators lift. The application of roughness to this case caused the maximum lift coefficient to decrease without vortex generators and increase significantly over the 2D clean case with the vortex generators applied. The total drag on the wing became equal at high angles of attack no matter what condition was tested. This suggests that the induced drag from the tip vortex dominates in the calculations and the viscous drag is only a small part of the total as should be expected from wing theory. The lift coefficient increased by approximately 50% for the 2D unsteady cases, unfortunately the unsteady flow experiences large hysteresis loops with hysteresis lift coefficients 60% lower than the upswing. The increase in the lift is due to the delayed stall which occurs because of the changes in the boundary layer due to the oscillations. The boundary layer becomes thinner on the upswing of the oscillation and stays attached until higher angles of attack. After

separation the boundary layer characteristics do not return to those of the upswing, thus creating the hysteresis loop, in which a different displacement and boundary layer thickness exist. These changes produce an unsteady stress on the structure of the wing and have to be incorporated into the design, and they depend on the frequency, the type of oscillation, the amplitude of the oscillation and the Reynolds number. The application of the grit roughness increases the size of the hysteresis loops, whereas the hysteresis lift coefficients are approximately 62% lower than the upswing values. This severe roughness causes changes in the boundary layer behavior, because the particles produce the excessive turbulence which in turn increases the thickness of the boundary layer and also increases its ability to separate. The lift coefficient for the 0.6 Hz frequency case for all Reynolds numbers shows a much lower maximum lift coefficient with approximately the same size hysteresis loop. The 1.8 Hz frequency cases have a maximum lift coefficient up to 100% higher than the steady state case but also have the largest hysteresis experienced, especially for the ±10° mean angle of attack. The pitching moment coefficients show a larger hysteresis loop occurring around the stall angle of attack, which happens earlier for the grit applied cases. The application of the vortex generators to the 2D clean case increases the hysteresis lift slightly for both the frequencies, the 0.6 Hz and 1.8Hz, but also they cause a sharp decrease in the pitching moment close to the stall angle of attack. The application of the vortex generators to the gritted model in a 2D setup has very little effect on all the aerodynamic parameters. The 3D unsteady cases exhibit the same characteristic lower lift curve slope and the larger stall angle of attack as did the 3D steady state case. In the 3D cases the wall station in the 0.6 Hz frequency cases obtains almost the same maximum lift coefficient as the 2D case but at a higher angle of attack. However, this phenomena does not occur in the

higher frequencies cases, where the maximum lift is lower than 2D model condition. Stronger interaction between the tip vortex and the oscillations occur, especially in the higher frequency. The pitching moment and pressure drag are not affected much by the 3D conditions. The tip station exhibits a strong effect of the tip vortex; therefore the lift curve slope and the maximum lift coefficient are much lower than the wall station and the 2D cases. From the six stations across the span, only the tip station displays small hysteresis loops for all the unsteady cases, due to the cross flow from the tip vortex, which is strongest at the tip station. Even though the tip station exhibits small hysteresis loops, the effect of the unsteady flow is manifested in the pressure coefficient with a higher maximum peak on the upswing and lower on the downswing. Also the pressure drag coefficient doubles at the tip station in comparison to the 2D clean data. The hysteresis loops were eliminated from the unsteady case with the application of the vortex generators for all frequency and Reynolds numbers at 8° and 14° mean angles of attack. The pressure distributions for cases with vortex generators applied and clean are the same for the same values of the lift coefficient, therefore the vortex generators in the 3D cases are exactly the right height and shape to mix the outer flow with the boundary layer. Usually only the wall section obtained with the vortex generators in steady state and unsteady the same lift coefficient, both the lift curve slope and the maximum lift are equal in the two cases. This suggests that the addition of the correct vortex generators to the unsteady cases, removes the oscillating behavior of the boundary layer and makes the system behave as steady state up to stall. After the wall section stall in steady state, the hysteresis loop appears back in the data as seen from the 20° mean angle case. The steady state data with the vortex generators at the tip station reached the same stall angle of attack but a slightly lower

maximum lift coefficient. The pitching moment and the pressure drag coefficients are both reduced for both the tip and wall stations with the application of the vortex generators. It is possible to reduce or remove the hysteresis loop with the application of the vortex generators from the unsteady data only up to the angle of attack where the steady state data stalled. The application of the leading edge grit roughness with the vortex generators returned the hysteresis loop to almost the same size as the clean 3D cases, especially at the wall station, however the tip station had still smaller hysteresis loop and higher maximum lift coefficient than with the grit only. Overall there was little change in the induced angle of attack due to the application of the vortex generators to the unsteady flow; however the induced angle of attack was increased at the tip station for the downswing. The hysteresis loop in the induced angle of attack was much larger at the wall station than at the tip station, but the induced angles of attack were generally lower for the wall station. The integrated induced drag was found to be higher for the steady state than for the unsteady flow, clean or with vortex generators. The vortex generators cases had the lower induced drag, especially at the higher angle of attack, than the clean wing condition, which exhibited a large hysteresis loop in the drag.

4. Problem Description for Proposed Dissertation

Based on the available literature, the following problem description is proposed for this project. With larger rotors being deployed on MW-scale machines, blade performance and loads have now become a key driver for product design. Vortex generators are currently used as a post design upgrade during different life stages of a wind turbine systems. OEMs deploy vortex generators immediately after the manufacturing process before field installation whereas wind turbine owners and operators incorporate VGs during the first ten years of turbine deployment. So far no one has evaluated the impact on performance and cost on the design of the blade if vortex generators are included during the optimization and multi-disciplinary design process, i.e., *integral vortex generator*. Further, flatback airfoils are now being commonly used in the design of rotor blades. However, there is a severe lack of flow characterization data for thick flatback airfoils (in an unsteady inflow environment). As noted earlier, in order to recover lost performance in the field, vortex generators are being actively deployed on rotor blades without understanding the impact of the dynamic inflow conditions on the performance and flow behavior of these airfoils. Hence, present research will study and characterize the flow behavior of a 47% thick flatback airfoil and will evaluate the impact on performance and cost for different design configurations on a multi-disciplinary basis. Specifically, three configurations are studied as a part of this dissertation namely clean configuration (no VGs), add-on design (VGs installed before field deployment) and VG-Opt configuration (integral VGs included during the multi-disciplinary optimization process). The steps to be undertaken moving forward are as follows:

1. Develop a multi-disciplinary optimization code for aero-structural and cost optimization of wind turbine blades.

2. Use the multi-disciplinary optimization tool to design a 56m blade (clean configuration).
3. Use CFD tools to model the 2D flow over an airfoil in steady and dynamic inflow conditions. CFD tools will be used to model the flow over a 2D wing section with vortex generators to understand and simulate the flow physics characteristics in a dynamic inflow condition. This will be based on the Janiszewska's study and results will be used to validate the method and approach used for the analysis of the thick Flatback airfoil.
4. Using CFD, the characteristics of a 47% thick Flatback airfoil and NACA 63621 airfoil with integral vortex generators is subjected to steady inflow conditions and the flow physics of these airfoils are studied in detail. A performance map for both these airfoils is created to identify the best vortex generator – airfoil configuration. This data is then used in the next step for blade design and analysis.
5. Based on the optimal vortex generator configuration obtained, two blade design configurations are studied. These are the 'Add-on VG' configuration and 'Integral VG' configurations.
6. A full blade multi-disciplinary optimization and design using integral vortex generators is carried out and the aerodynamic performance is highlighted.
7. Finally, a comparison between the three blade designs is made and the conclusions are drawn pertaining to the best blade design configuration in multi-disciplinary design space.

5. Wind Turbine Blade Optimization

As a part of this dissertation and ongoing work at Wetzel Engineering, an optimization routine for system optimization is developed and is used for the optimization and design of a 56-m blade for a 2.0 MW wind turbine. This section provides an overview of the multi-disciplinary optimization process used for determining the optimal configuration for the 56m blade design for a variable speed 2.0 MW wind turbine. A design feasibility analysis is performed in order to determine the optimal blade configuration for a rotor blade length of 56-m and the ideal operational parameters for the given turbine rating of 2.0 MW. The design optimization provides the results to understand the tradeoffs between different design disciplines like Maximum Blade Root Bending Moment (M_{XY}), Blade Mass, Blade Cost, Annual Energy Production (AEP) and Cost of Energy (COE). The design requirements are specified before the optimization process by WEI. These are used as inputs into the optimization process to generate the necessary blades.

5.1. Multi-Disciplinary Optimization Setup

The following steps are performed as a part of the multi-disciplinary optimization analysis.

- The design requirements are established by WEI, as described in Table 3.
- The optimization was carried out for:
    - Rotor Blade Length: 56m
    - Wind Class: III-A (as per GL 2010)
    - Rated Power: 2.0 MW
    - Shaft Speed: 12.5 rpm
    - Spar Cap Material: H-Glass

- Table 4 - Table 6 summarizes the inputs used for the optimization analysis carried out for the 2.0 MW turbine.
- DU-NACA airfoil family is considered as a primary airfoil family for this optimization. (See Table 4 and Table 5).

Table 3. Summary of Design Requirements for the 2.0-MW Wind Turbine Rotor

Design Wind Class	III-A (GL 2010)
Blade Mass	≤ 12.5tons
Blade Cost	(Minimize)
Extreme Root Bending Moment Load Margin, M_{XY}	≤ 10,000 kNm
Rated Power	2.0 MW
Blade Length	56m
Hub Height	80 m
Rated Shaft Speed	12.5rpm
Blade Primary Material	H-Glass

Table 4. Nominal Airfoil Thickness and Airfoil Designation

Airfoil Designation	Airfoil Thickness-to-Chord Ratio
WEI-FB47	47.29%
DU-W-405LM	40.50%
DU99-350	35.09%
DU97-W-300LM	30.00%
DU91-W2-250LM	25.00%
NACA63621	21.00%

Table 5. List of Design Variables for the 2.0-MW Rotor Blade Optimization Study

Design Input Variable	Choice of Selection	Comments
Airfoil Family	WEI-FB, DU and NACA family	WEI-FB, DU and NACA airfoil family consisted of FB-47, DU 40, DU35, DU30, DU25, NACA 63621 airfoils.
Thickness distributions	No. of thickness distributions = 8	8 distributions are defined to cover the entire design space. This selection is defined to accommodate both high aerodynamic performance blades as well as structurally efficient blade designs.
Chord Distributions	Max chord variation: From 2.5 to 3.5 m	A spanwise distribution based on the maximum chord variation was defined to obtain different blade planforms. The matrix of chord combinations and thickness distributions equated to approximately 1.7million blade designs in the rotor optimization
Materials	H-Glass	-

Table 6. Summary Table of Airfoil Thickness Distribution for the Optimization Study

Radial Station	Airfoil Thickness-to-Chord Ratio Distribution							
r/R	**AF-1**	**AF-2**	**AF-3**	**AF-4**	**AF-5**	**AF-6**	**AF-7**	**AF-8**
r_{hub}/R	100.00 %	100.00 %	100.00 %	100.00 %	100.00 %	100.00 %	100.00 %	100.00 %
25.00%	40.00%	40.00%	40.00%	40.00%	40.00%	58.30%	47.00%	47.20%
30.00%	37.50%	35.00%	32.50%	37.50%	36.50%	44.70%	40.00%	44.70%
40.00%	35.00%	30.00%	27.50%	32.50%	30.00%	40.00%	35.00%	40.00%
50.00%	32.50%	27.50%	25.00%	30.00%	27.50%	35.00%	30.00%	35.00%
60.00%	30.00%	25.00%	22.50%	27.50%	25.00%	30.00%	25.00%	30.00%
70.00%	27.50%	22.50%	21.50%	25.00%	23.00%	25.00%	21.00%	25.00%
80.00%	25.00%	21.00%	21.00%	22.50%	21.00%	21.00%	21.00%	21.00%
94.00%	22.50%	21.00%	21.00%	21.00%	21.00%	21.00%	21.00%	21.00%
100.00 %	21.00%	21.00%	21.00%	21.00%	21.00%	21.00%	21.00%	21.00%

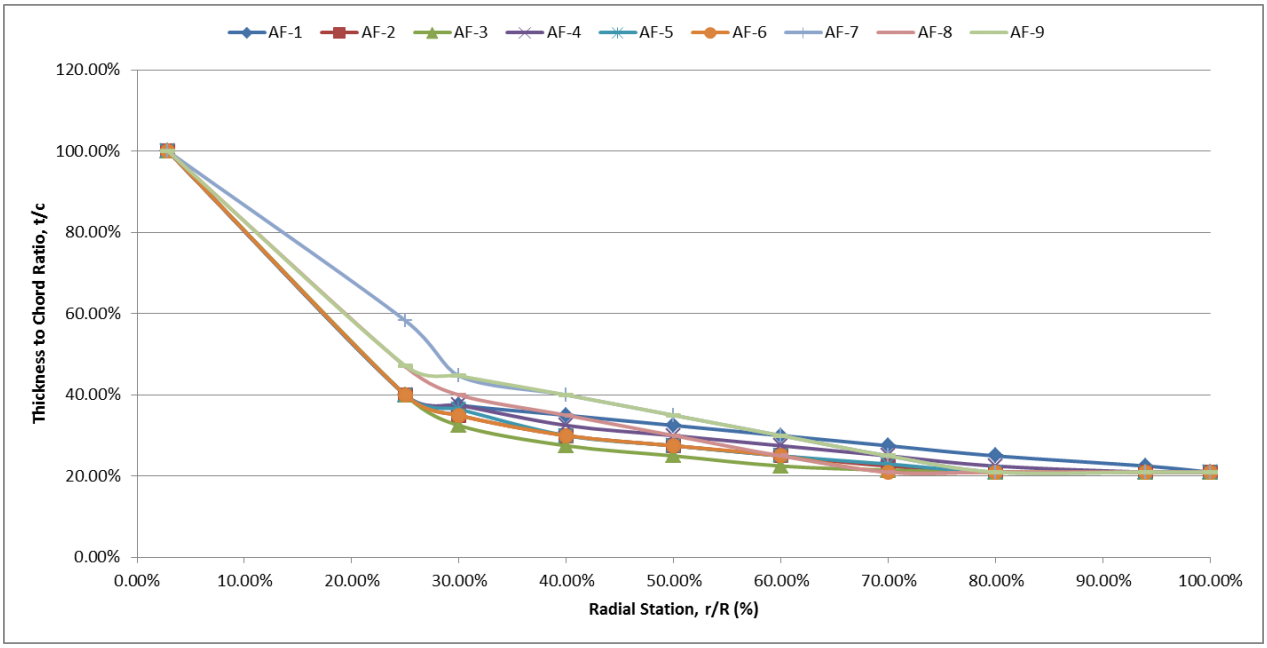

Figure 9. Thickness-to-Chord Ratio Plot of Airfoil Thickness Families for Optimization

5.2. Aero-Structural Optimization Techniques

In order to study and evaluate various designs, it is essential to determine a design space which is based on constraints determined for this blade design.

To understand the contribution from several parameters defined in the multi-disciplinary design space, it is essential to develop and study the various trend lines obtained from different configurations. BladeOpt is used to generate and plot these trend lines or cloud plots. BladeOpt is a tool which allows a blade designer to pick a design space as a preliminary estimate for the design of a wind turbine blade. The overall goal of the BladeOpt is to optimize the blade design taking into account the aero-structural properties and cost of the entire system.

BladeOpt is a multi-disciplinary code and consists of the following modules that are used to define the optimal blade design:

- Aerodynamics Module
- Structural Module
- Loads Module
- Cost Module

Once the cloud plots are generated, the chosen design space is evaluated primarily based on four main aspects namely:

- Cost of Energy, COE
- Maximum Root Bending Moment Loads, M_{XY}
- Annual Energy Production, AEP
- Aerodynamic Coefficient of Performance, C_p

A schematic of the multi-disciplinary optimization code is shown in Figure 10. Representative cloud plots are shown in Figure 11. Based on these four criteria, a suitable blade design space is selected. Thereafter, a refined stage of optimization is carried out for a restricted design space. Sample representative optimal planforms are then defined and the blade layout is initiated by fine tuning the chosen optimal planforms in order to define a smooth profile for thickness and chord distributions. For advanced concepts like TBC, a structural optimization is undertaken, after the optimal planform has been defined, to determine the optimal internal structure for the blade.

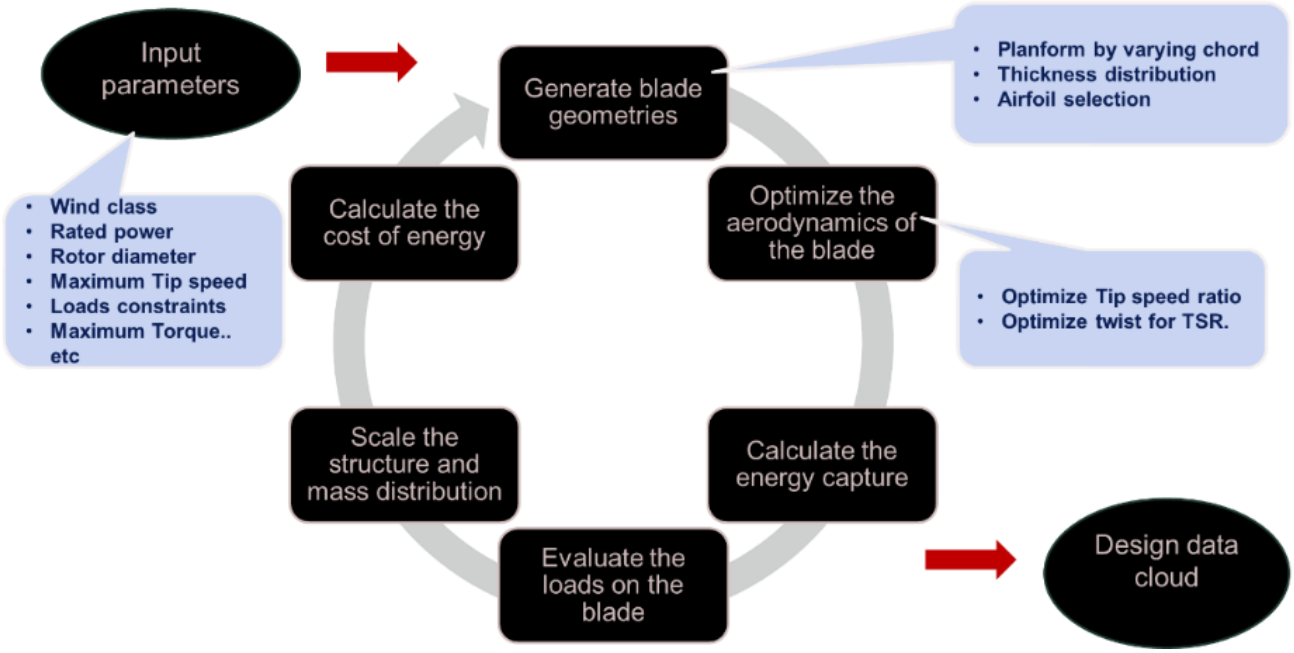

Figure 10. Schematic of BladeOpt

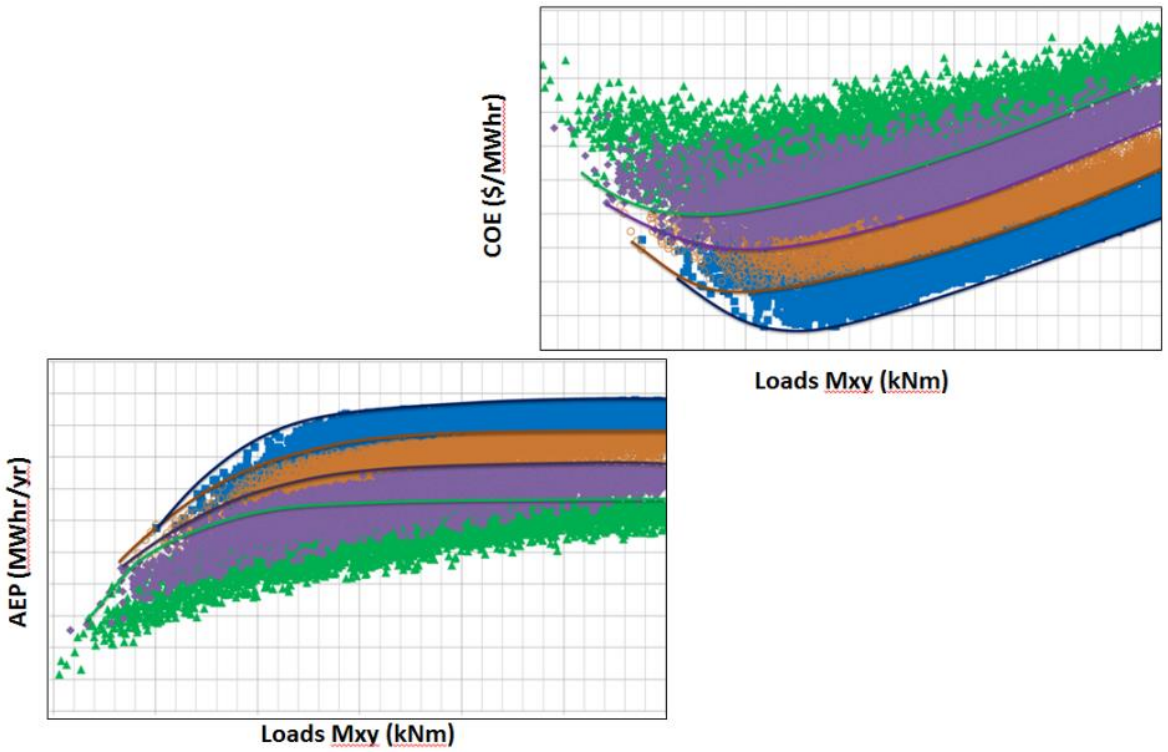

Figure 11. Representative Cloud Plots from BladeOpt

5.2.1. Aerodynamics Module

The aerodynamics module in BladeOpt is based on the Blade Element Momentum (BEM) Theory. In order to generate a cloud plot, several combinations of input parameters are defined. These input parameters include thickness and chord distributions, choice of airfoil families, blade length and material definitions. For this study, the parameters are used as listed in Table 4 to Table 6.

A detail description of the optimization process is as follows. As discussed earlier, the aerodynamic optimization is based on blade momentum theory. In order to evaluate various configurations, a matrix of chord and twist distributions is created. For both the chord and twist distributions, five stations along the blade are chosen. These stations are r/R = 25%, 40%, 60%, 80% and 94%. For each station, a minimum and maximum value

is provided and the number of intervals are specified. In order to evaluate different airfoil families, a matrix of thickness distribution is provided. Typically, 6 to 10 airfoil thickness distributions are specified. The thickness distribution is specified at 10 stations along the blade span at 10% intervals. Using the chord, thickness and twist distributions, and a matrix is created which defines the various planform configurations.

Once the different geometries are created, a performance analysis is performed. As a part of this performance analysis, the sectional performance is calculated and integrated along the blade span for each wind speed. Performance data for each wind speed include power rating, optimal tip speed ratio, optimal twist and coefficient of power. Other loads related metrics like rotor thrust and other forces are calculated as a part of this analysis. Finally, the energy captured at different wind speeds for a given configuration is used to calculate the overall annual energy capture using a probability density function. Either Rayleigh or Weibull distribution can be used for the annual energy capture calculation. Upon completion of the aerodynamic calculations, loads analysis and structural design is carried out.

5.2.2. Structural Module

Structures module defines the internal structure of the blade. The design philosophy here is to use appropriate scaling laws to create a structural definition for each blade being generated during the optimization process. Scaling laws are applied to a baseline blade. The choice of baseline blade is very critical to the accuracy of the results. The scaling laws used for this model are developed from the in-house expertise based on the structural design carried out for several blades. Some of the design laws are as listed in

Table 7. At the present stage, the final structure for a chosen optimal blade is not output as a part of the optimization routine. As an example, for a given optimal blade that incorporates sweep or pre-bend, the amount of curvature required to achieve the loads constraint or to achieve the tower clearance constraint, respectively, is not explicitly defined as a part of the optimization routine. However, once a particular planform is chosen, the internal structure is optimized in which the amount of curvature, material layout, laminate definitions, etc. is defined.

Table 7: Scaling Laws for the Structural Module.

Parameter	Scaling Factor
Girder Thickness	***f* (Moment, Blade thickness, Blade Length)**
Girder width	***f* (Baseline girder width)**
Shell Skin	***f* (Moment, Blade thickness, Girder Thickness)**
Shell Core	***f* (Baseline shell core thickness)**
Web skin	***f* (Baseline web skin thickness)**
Web height	***f* (Baseline web height, Blade thickness)**
Web core	***f* (Baseline web core thickness)**
Root Reinforcement thickness	***f* (Baseline root reinforcement thickness, Sectional arc length)**

Although some secondary effects, e.g., internal layup, is not automated/included in the model, the current approach does give a reasonable estimate for the optimal blade design that meets the given design constraints.

5.2.3. Loads Module

The aerodynamic loads are calculated based on a steady BEM model. The resulting moment is calculated as the vector sum of aerodynamic moments and gravity loads. Based on extensive loads analysis carried out in the past, several correlation factors have

been generated and are used for the loads analysis. The loads analysis being carried out are not a time dependent based calculation as seen in full dynamic calculators. The extreme loads are calculated based on various DLC cases that are built into the optimization routine. These DLC cases include NTM load cases at rated wind speed and cutout, Extreme Operating Gust (EOG) (both 1 year and 50 year extreme) at V_{rated}, $V_{rated+2}$, $V_{rated-2}$ and V_{cutout}, Extreme Coherent Gust and Direction Change (ECD) for V_{rated}, $V_{rated+2}$ and $V_{rated-2}$, etc. Apart from the operating loads, the parked loads are calculated for DLC 6.1, 6.2 & 6.4 parked rotor cases (IEC Guidelines) as well. The highest obtained loads are reported as the maximum loads for the particular blade design. Load cases are also post-processed for maximum blade deflection calculation in the structural routine. The highest obtained loads are reported as the maximum loads for the particular blade design. It should be noted that a safety factor, as per GL guidelines, is used during the loads calculation.

5.2.4. Cost Module

The cost module determines the Cost of Energy (COE) based on the entire system cost. The cost of the system includes the blade, tower and turbine costs. The blade cost is calculated based on the material and labor cost of a given blade. A mass estimation tool is used to determine the mass of each component which then translates into the material cost and hence the total cost of the blade. The turbine cost is the sum of all component costs. Cost of each component is either fixed or scales as a function of loads, power or other turbine parameters. The cost module also accounts for the facilities costs and costs incurred towards blade tooling. Based on these costs, the cost of energy is calculated. An

overview of the formulation of the cost module is given in Table 8. Figure 12 shows a schematic of the cost analysis module used in the BladeOpt code.

Table 8: Cost Estimate Module Formulation for Rotor Optimization.

Parameter Cost	Cost Function
Blade	***f*** **(Mass of Shell, Web, Girder, TE Girder, Root reinforcement, Adhesive, Paint, Resin)**
Labor	***f*** **(Hours required for Tool prep, Lamination, Bagging, Infusion/Curing, Cleanup, Assembly, Demolding, Cleanup, Paint, Finish, etc)**
Facilities	***f*** **(Blade Length, Fixed Price /number of blades manufactured per year)**
Tooling Amortization	***f*** **(Blade Length)**
Gearbox	**Baseline cost*** ***g*** **(Torque)**
Hub, Pitch system, Main Shaft, Main Bearings	**Baseline cost*** ***g*** **(Mxy)**
Mainframe and Yaw Bearing	**Baseline cost*** ***g*** **(Mxy)**
Tower and Foundation	**Baseline cost*** ***g*** **(Mxy)**
Balance of Station and Project Development	**Fixed cost assumed**
Cost of Energy	**{(0.1*Total Initial Capital Cost + Total Annual O&M)/Net Annual Energy Production} + Land Lease**

f = Function (Component Cost); g = Function (Component Load/Torque)

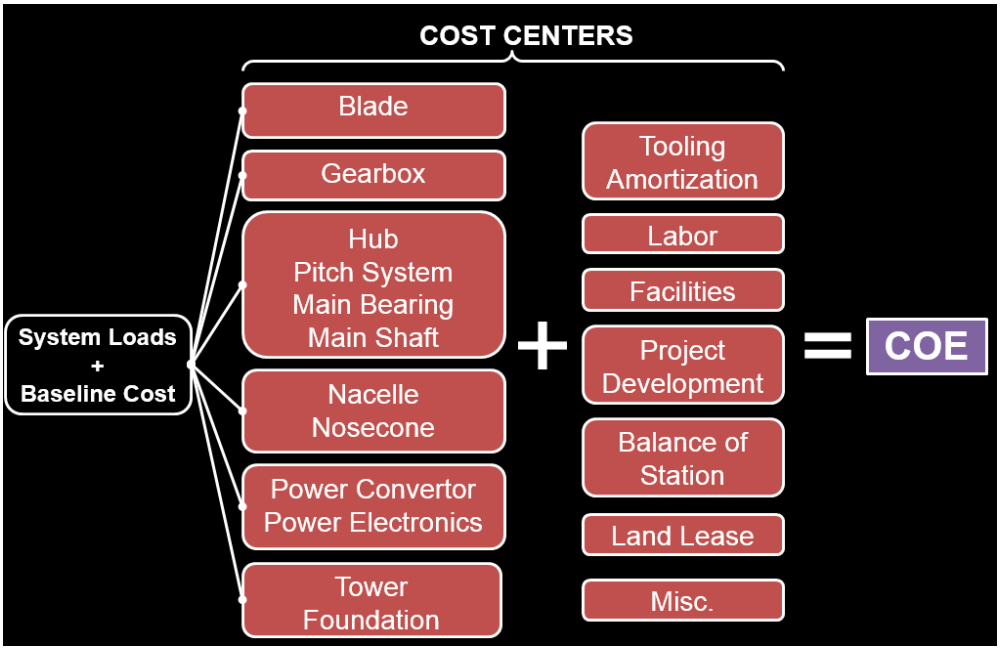

Figure 12: Schematic of Cost Module

5.3. Optimization Analysis Results

This section gives details about post processing the results obtained from the BladeOpt. After imposing the weighting criteria provided in the next section, the design space is further narrowed down and the optimal blade is selected from the down selected blades. Section 5.4 and 5.5 discusses overall post processing approach whereas Figures 5.6 and 5.7 have details on specifics used in post processing different designs for a blade variable speed 2.0-MW turbine.

5.4. Design Constraints

Out of 1,676,808 blades obtained from the BladeOpt, only the blades that would satisfy the design constraints specified in would be considered for further examination. All design constraints established earlier are applied. The cost functions are calculated for each of these blades and the top 3 blades with the lowest cost functions are selected for a final optimal blade selection.

5.5. Cost Functions

The cost function of each blade is a function of various blade parameters, their ranges, the relative distance of the value of the parameters from the corresponding parameters of the blade with the lowest COE in the design space, and the weight assigned to the parameters. The parameters considered are the M_{XY}, AEP, Blade Mass, Blade Cost, and COE. Other parameters can be added if required. If any of the parameters are not to be included, then their weight is assigned equal to zero.

The normalized weights are assigned to each of the parameters based on their relative importance. This quantification of relative importance, or weights, depends on several factors such as the market, blade manufacturer, customer, application, etc. Since there are

multiple possibilities, several possibilities are considered and thus different sets of weights are used.

Depending on the weights assigned to each of the parameters, there are different sets of cost functions. All these different sets of cost functions are calculated for each blade. Then the blade with the lowest cost function for each different set of cost function is identified. Out of these, one of them is selected as the optimal blade. In this report, blades that have the lowest cost function are presented, and only a recommendation is made for the final blade to be selected as the optimal blade.

5.6. Weights for Properties used for 2.0-MW Wind Turbine

The weights used for the parameters examined for the current blade, i.e. the 2.0MW wind turbine are given in Table 9. A total of four different sets were examined.

Table 9. Weight for each property and different sets of weights for the design space

Sl. No.	Property	Set 1	Set 2	Set 3	Set 4
1	M_{XY}	0.00%	35.00%	35.00%	25.00%
2	AEP	35.00%	0.00%	0.00%	0.00%
3	Blade Mass	45.00%	65.00%	35.00%	25.00%
4	Blade Cost	20.00%	0.00%	30.00%	25.00%
5	COE	0.00%	0.00%	0.00%	25.00%

5.7. Blades with the Lowest Cost Function under each Set of Weights

The blades with the lowest cost function under each set and its properties are given in Table 10. Table 10 shows that there are only three blades within the design space that has the lowest cost function depending on the weight sets given in Table 9. A final recommendation of AF7-6812 blade design is made due to high performance, low blade

weight and low blade root bending moment, M_{xy} values. It should be noted that we would expect a +/- 5% margin on the blade root bending moment.

Table 10. Blades with the Lowest Cost Function

Set No.	Blade Name	Maximum Root Bending Moment, M_{XY} (kNm)	Annual Energy Production, AEP (MWh/yr)	Coefficient of Power, C_p	Blade Mass (tons)	Cost of Energy, COE (US$/MWh)
1	AF4-6788	8610	9161	0.4797	12.14	37.33
2	AF7-7167	8344	9120	0.4734	11.33	37.14
3	AF7-6812	8317	9162	0.4805	12.10	37.25

6. Design of the 56-m Blade

6.1. Blade Aerodynamic Design Data Summary & Blade Planform Design

This section consists of the aerodynamic design of the 56m blade. Based on the optimal design selection from the previous task, the aerodynamic design is carried out. The aerodynamic design and performance estimation is carried out using in-house BEM based codes at WEI. Table 11 provides the summary of the planform characteristics of the 56m blade. Detailed information can be provided under request. The aerodynamic performance, based on steady inflow conditions, of the 56m blade is given in Table 12. Maximum Aerodynamic Power Coefficient, C_{pmax} = 0.4805 is achieved whereas an Annual Energy Production based on IEC Class III Rayleigh distribution, AEP = 9,165MWhr. Figure 15 shows the tip speed ratio and shaft speed schedule for the 56m blade. Figure 16 shows the coefficient of performance distribution vs wind speed for this configuration. Figure 17 shows the electric and aerodynamic power curves for the designed configuration.

Table 11. Summary of the Aerodynamic Design of the 56-m blade

Radial Station		Spanwise Station	Chord	Solidity	Twist	Sectional thickness	Thickness-to-Chord Ratio	Airfoil
r	r/R	$s = r - r_{hub}$	c	σ	θ	t	t/c	**Used for Aerodynamic Modelling Purposes
(m)		(m)	(m)		(°)	(m)		
1.500	2.6%	0.000	2.215	0.705	0.00	2.215	100.0%	Cylinder
11.500	20.0%	10.000	3.460	0.144	10.75	1.630	47.1%	47.1% t/c Transition Flatback Airfoil
28.750	50.0%	27.250	1.960	0.033	2.05	0.645	32.9%	32.9% t/c Interpolated DU-99-350 & DU97-W-300LM
57.500	100.0%	56.000	0.075	0.001	1.00	0.016	21.0%	NACA63621

Table 12. Performance for Prated=2.0 MW, assume Drivetrain Efficiency of (Peak 90%)

ROTOR PERFORMANCE OUTPUT PARAMETERS								
Wind Speed	Shaft Speed	Tip Speed Ratio	Pitch Angle	Aero Power Coefficient	Aero Power	Electric Power	Aero Power	Electric Power
V (m/s)	Ω (rpm)	X (~)	β (°)	C_{paero} (~)	P_{aero} (kW)	P_{elec} (kW)	P_{aero} (MW)	P_{elec} (MW)
3.50	6.50	11.18	0.00	0.483	131.63	118.47	0.13	0.12
4.00	6.98	10.50	0.00	0.485	197.55	177.80	0.20	0.18
4.50	7.85	10.50	0.00	0.485	281.30	253.17	0.28	0.25
5.00	8.72	10.50	0.00	0.485	385.88	347.29	0.39	0.35
5.50	9.59	10.50	0.00	0.485	513.60	462.24	0.51	0.46
6.00	10.46	10.50	0.00	0.485	666.80	600.12	0.67	0.60
6.50	11.33	10.50	0.00	0.485	847.77	763.00	0.85	0.76
7.00	12.21	10.50	0.00	0.485	1058.85	952.96	1.06	0.95
7.50	12.50	10.04	0.00	0.481	1290.50	1161.45	1.29	1.16
8.00	12.50	9.41	0.00	0.468	1523.41	1371.07	1.52	1.37
8.50	12.50	8.85	0.00	0.449	1755.04	1579.54	1.76	1.58
9.00	12.50	8.36	0.00	0.427	1981.12	1783.01	1.98	1.78
9.50	12.50	7.92	0.00	0.404	2202.59	1982.33	2.20	1.98
10.00	12.50	7.53	3.45	0.350	2226.91	2004.22	2.23	2.00
10.50	12.50	7.17	5.45	0.3017	2221.67	1999.50	2.22	2.00
11.00	12.50	6.84	6.90	0.2630	2227.20	2004.48	2.23	2.00
11.50	12.50	6.54	8.20	0.2293	2219.05	1997.14	2.22	2.00
12.00	12.50	6.27	9.30	0.2022	2223.29	2000.96	2.22	2.00
12.50	12.50	6.02	10.35	0.1788	2221.36	1999.22	2.22	2.00
13.00	12.50	5.79	11.33	0.1591	2223.36	2001.03	2.22	2.00
13.50	12.50	5.58	12.28	0.1417	2218.61	1996.75	2.22	2.00
14.00	12.50	5.38	13.15	0.1274	2223.92	2001.53	2.22	2.00
14.50	12.50	5.19	14.00	0.1147	2223.94	2001.55	2.22	2.00
15.00	12.50	5.02	14.83	0.1035	2221.78	1999.60	2.22	2.00
15.50	12.50	4.86	15.63	0.0937	2219.04	1997.14	2.22	2.00
16.00	12.50	4.70	16.38	0.0854	2226.65	2003.99	2.23	2.00
16.50	12.50	4.56	17.15	0.0777	2219.16	1997.25	2.22	2.00
17.00	12.50	4.43	17.88	0.0711	2223.66	2001.29	2.22	2.00
17.50	12.50	4.30	18.60	0.0652	2222.38	2000.14	2.22	2.00
18.00	12.50	4.18	19.33	0.0598	2219.01	1997.11	2.22	2.00
18.50	12.50	4.07	20.03	0.0551	2218.83	1996.95	2.22	2.00
19.00	12.50	3.96	20.70	0.0510	2223.66	2001.29	2.22	2.00
19.50	12.50	3.86	21.38	0.0471	2221.67	1999.50	2.22	2.00
20.00	12.50	3.76	22.03	0.0437	2222.66	2000.39	2.22	2.00
20.50	12.50	3.67	22.68	0.0405	2217.81	1996.03	2.22	2.00
21.00	12.50	3.58	23.30	0.0377	2220.43	1998.38	2.22	2.00
21.50	12.50	3.50	23.93	0.0351	2216.89	1995.21	2.22	2.00
22.00	12.50	3.42	24.53	0.0328	2220.67	1998.60	2.22	2.00
22.50	12.50	3.35	25.13	0.0306	2219.14	1997.22	2.22	2.00
23.00	12.50	3.27	25.70	0.0288	2226.93	2004.23	2.23	2.00
23.50	12.50	3.20	26.30	0.0268	2215.19	1993.67	2.22	1.99
24.00	12.50	3.14	26.88	0.0252	2214.10	1992.69	2.21	1.99
24.50	12.50	3.07	27.43	0.0238	2224.04	2001.64	2.22	2.00
25.00	12.50	3.01	28.00	0.0223	2215.22	1993.70	2.22	1.99

***Note: Blade aerodynamic performance analysis results assume clean performance of airfoil sections and steady power.**

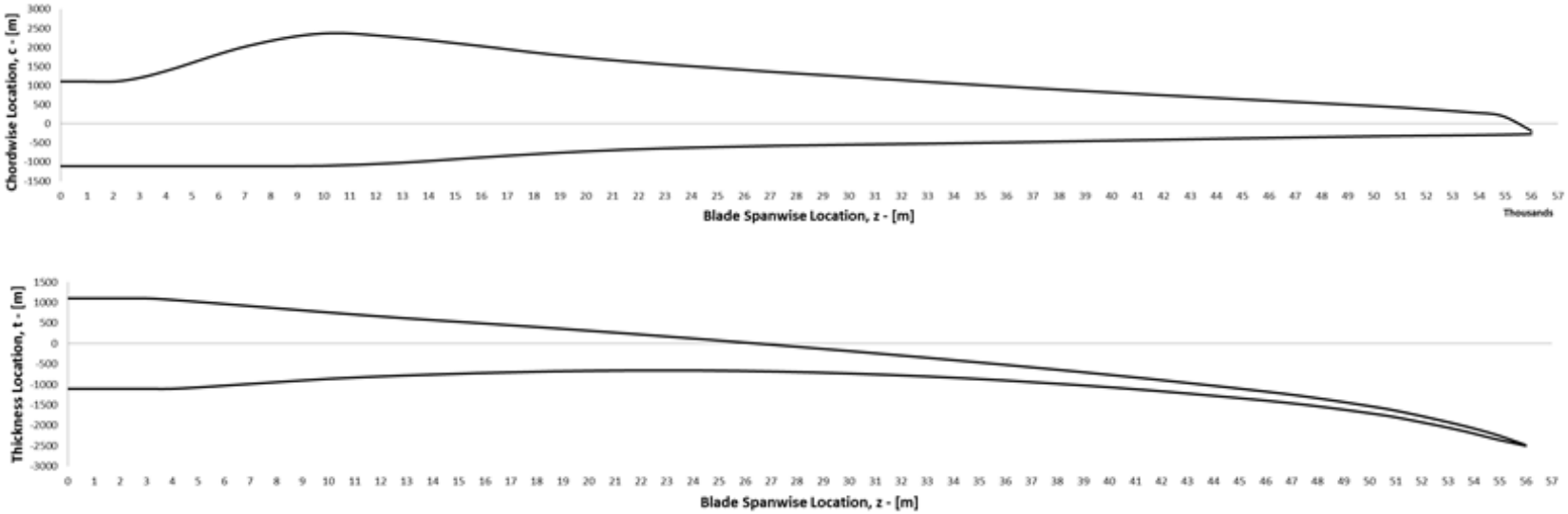

Figure 13. Planform definition for 56m blade

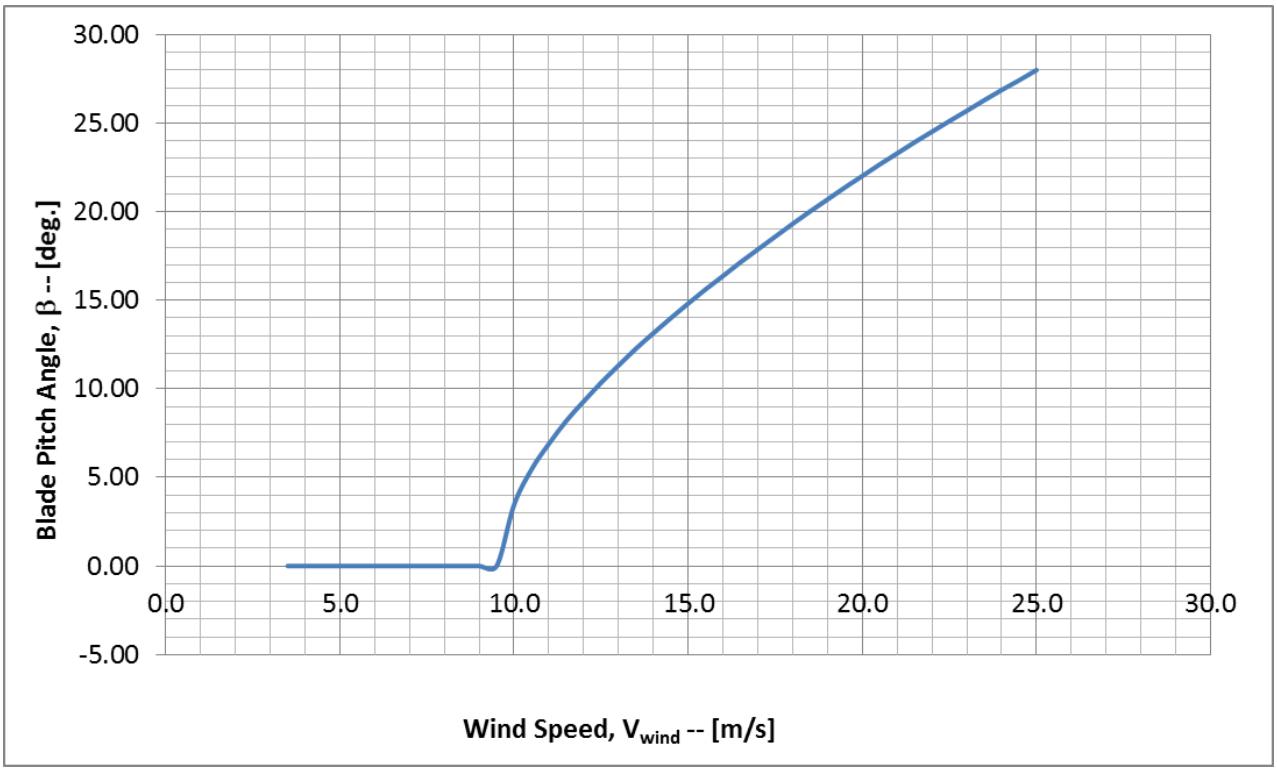

Figure 14. Blade Pitch Angle-Speed Schedule for 56m blade

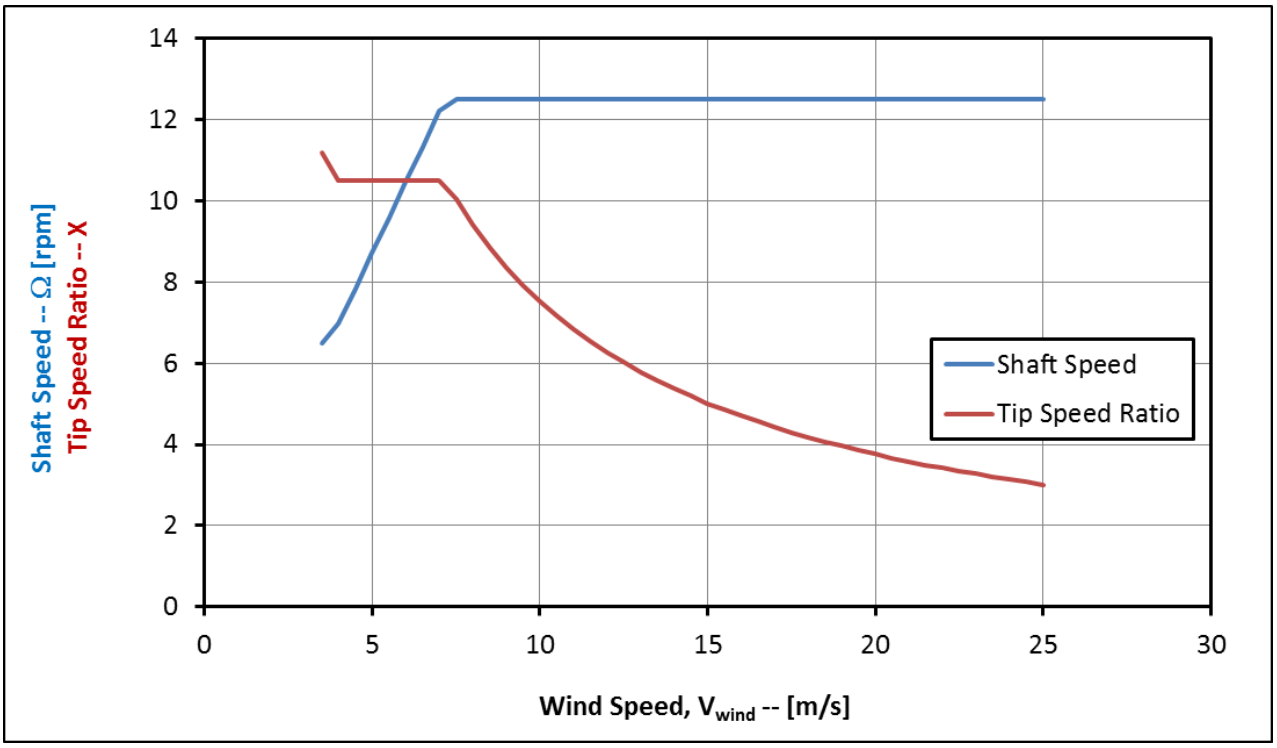

Figure 15. Shaft Speed Schedule and Tip Speed Ratio for the 56m blade

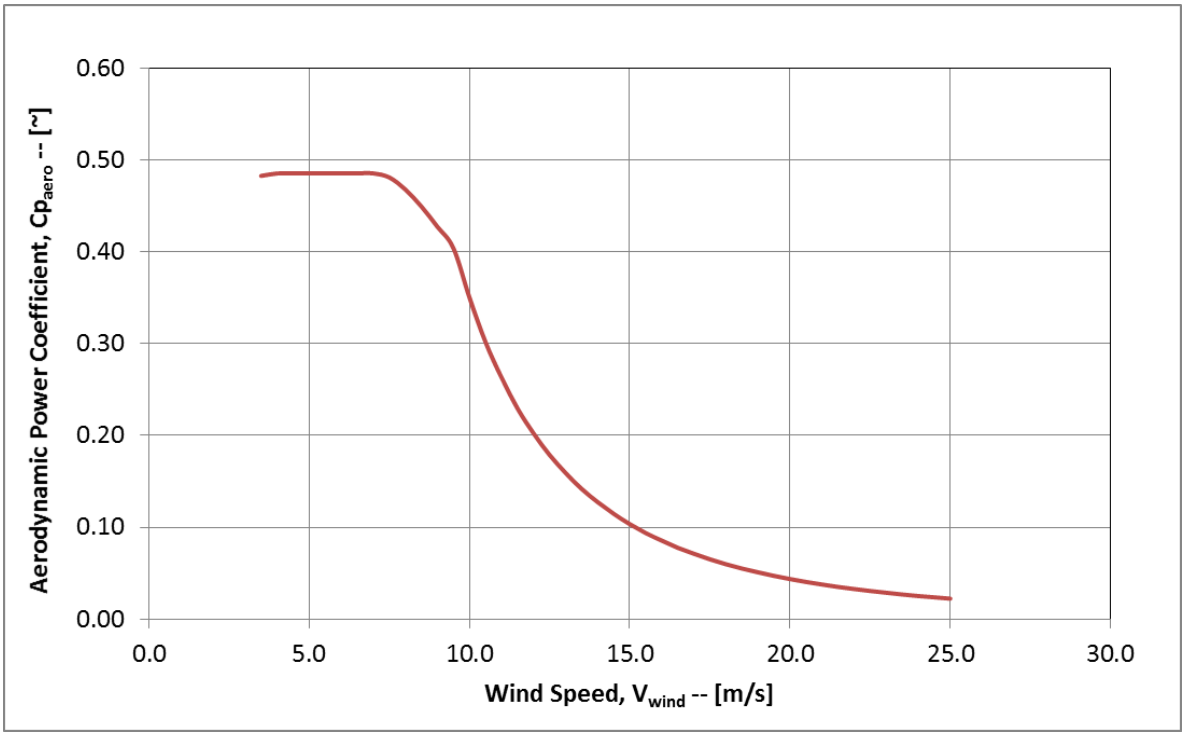

Figure 16. Aerodynamic Power Coefficient for 56m blade

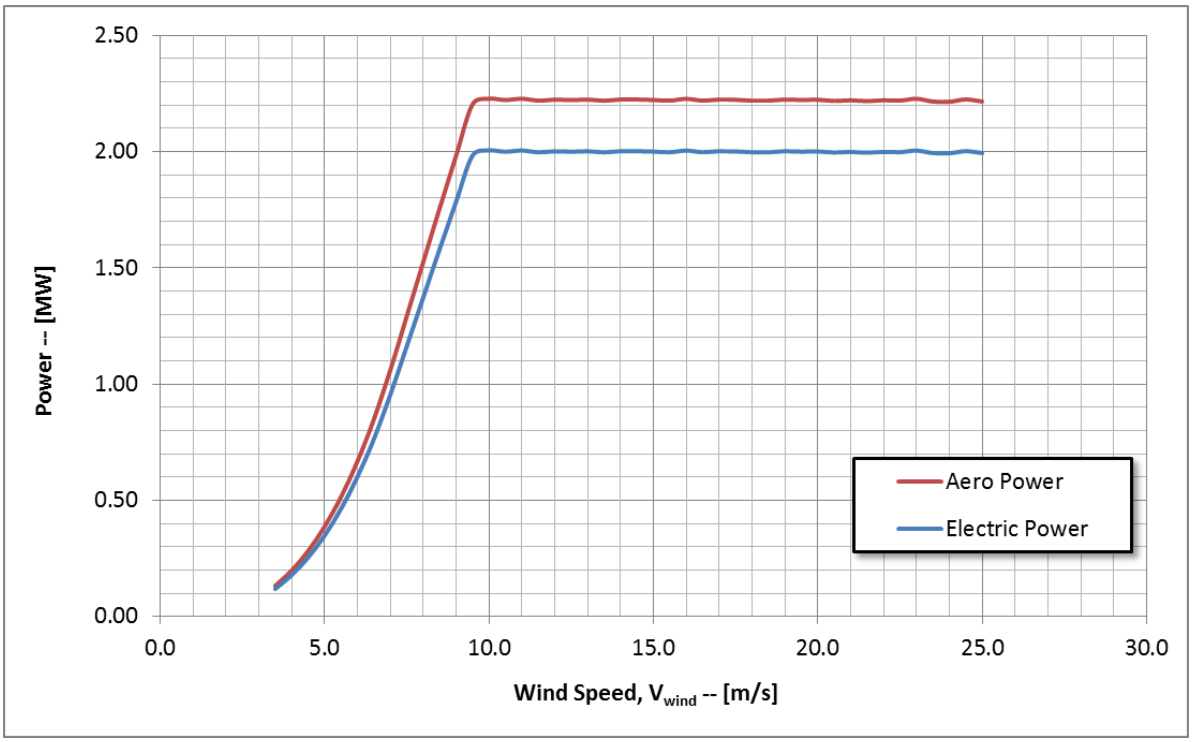

Figure 17. Power Curves for the 56m blade

6.2. Airfoil Aerodynamics of Blade Sections

6.2.1. Airfoil Sections in Outboard Blade Region

The airfoil sections of the rotor blade were designed using commercially available airfoils with reliable aerodynamic lift and drag data. These airfoils are: DU-W-405LM, DU99-350, DU97-W-300LM, DU91-W2-250LM and NACA 63621. These airfoils have been wind tunnel tested and proven to deliver well-behaved aerodynamic characteristics for good overall rotor performance. [49] An in-house aerodynamic-structural optimization code is used to determine a combination of chord lengths and selection of airfoil sections so as to optimize for maximum energy capture given the rotor design constraints. The aerodynamic lift and drag data for the airfoils used in the design of the blade (from the maximum chord location to blade tip) are presented in this section.

6.2.2. Airfoil Data Interpolation

Based on prior experience, we have noticed that the interpolation of airfoil data using GH-Bladed has led to dynamic instability issues during rotor blade aero-elastic simulations. The reason for the same remains unknown. In order to avoid this problem, we interpolate the airfoil data for the outboard sections using the pure airfoil sectional data as given below. A simple weighted interpolation technique is used to perform this exercise which simply calculates the performance of a given section based on interpolation of data from adjacent pure airfoil stations. So, for a section on the blade which contains a blend of two pure airfoils, we use a weighted average of the pure airfoil stations' properties to obtain those for the chosen section which lies in between the two pure airfoil stations. For example, as per the Table 11 above, (37.77% t/c_Interpolated_DU-W-405LM & DU99-350) results from a blend obtained from its

adjacent pure airfoils on either side i.e. DU-W-405LM & DU99-350. The resulting lift and drag properties at each corresponding angle of attack for the airfoil hence contains 49.5% of DU-W-405LM and 50.5% of the DU99-350 pure airfoil's characteristics, respectively.

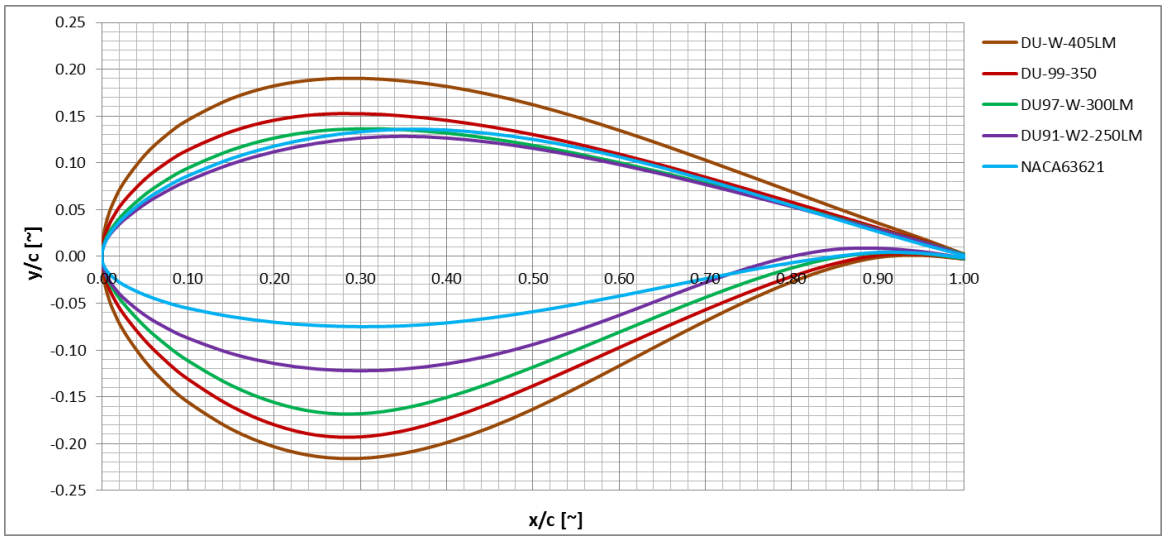

Figure 18. Airfoil Coordinates for Blade Airfoil Sections

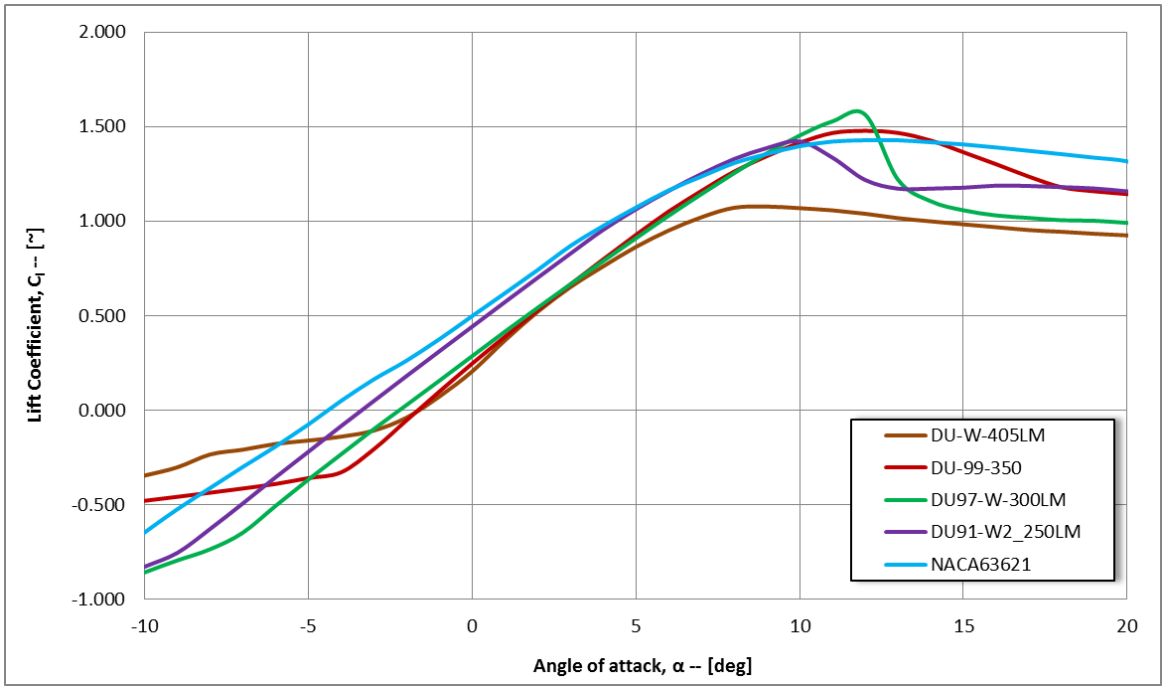

Figure 19. Aerodynamic Lift Curves for Blade Section Airfoils (Reduced Range)

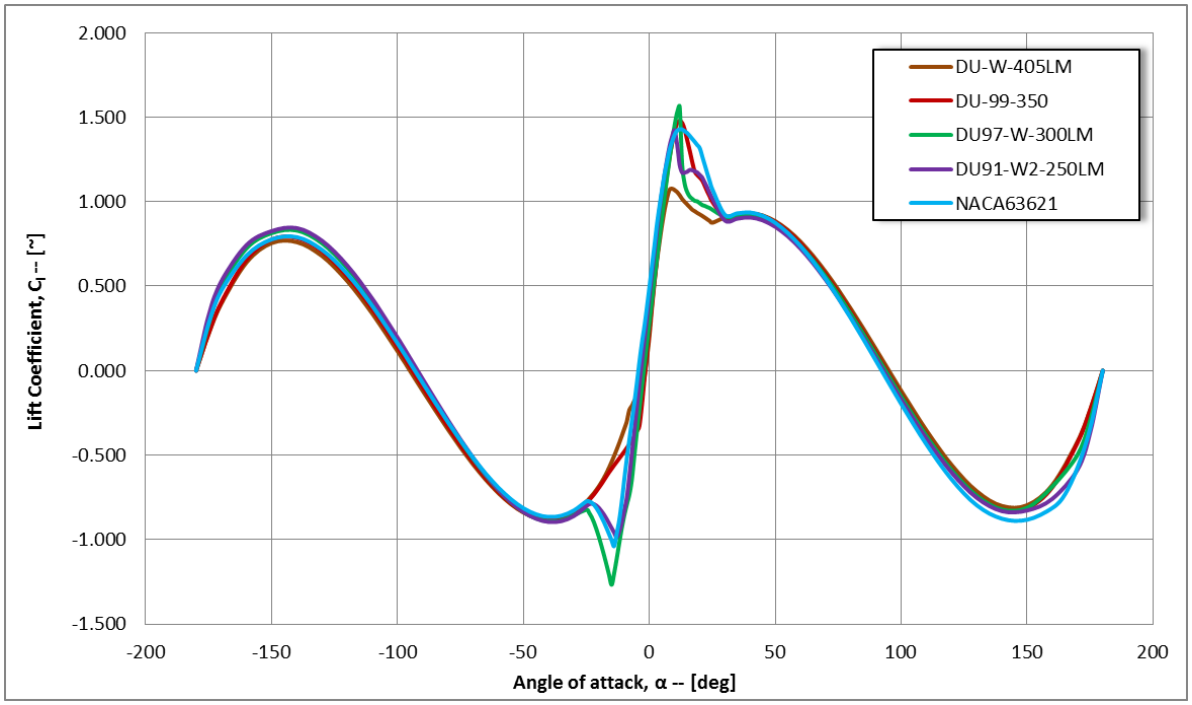

Figure 20. Aerodynamic Lift Curves for Blade Section Airfoils

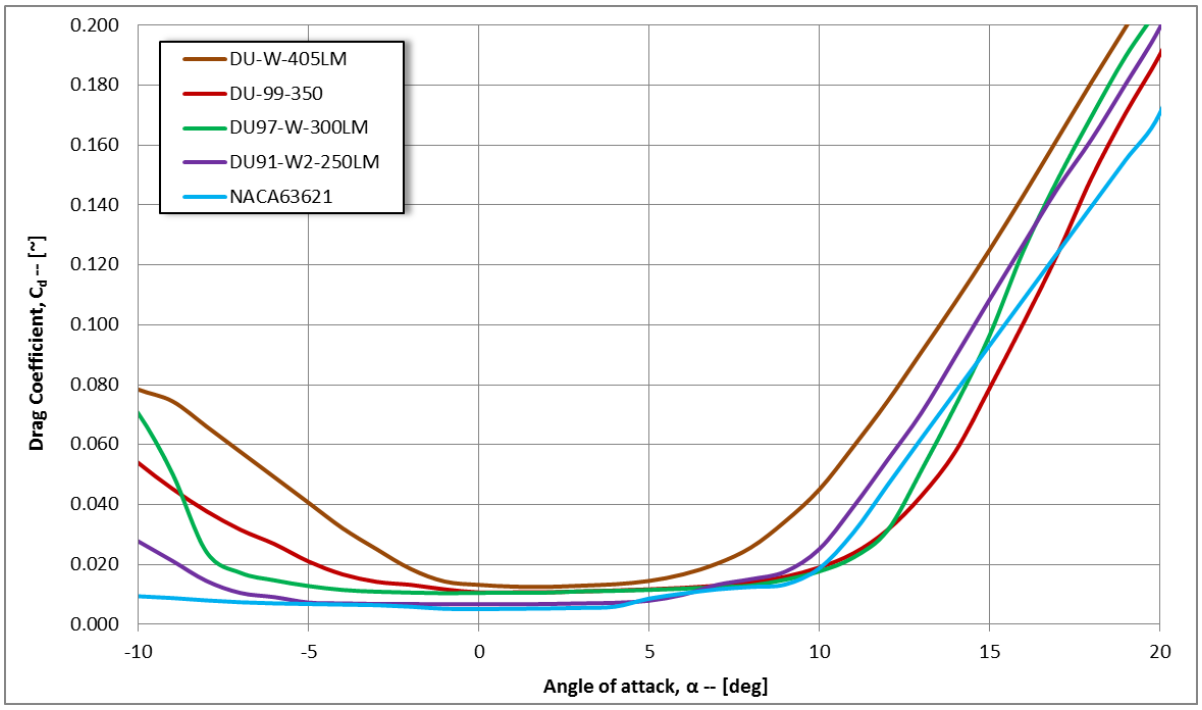

Figure 21. Aerodynamic Drag Data for Blade Section Airfoils (Reduced Range)

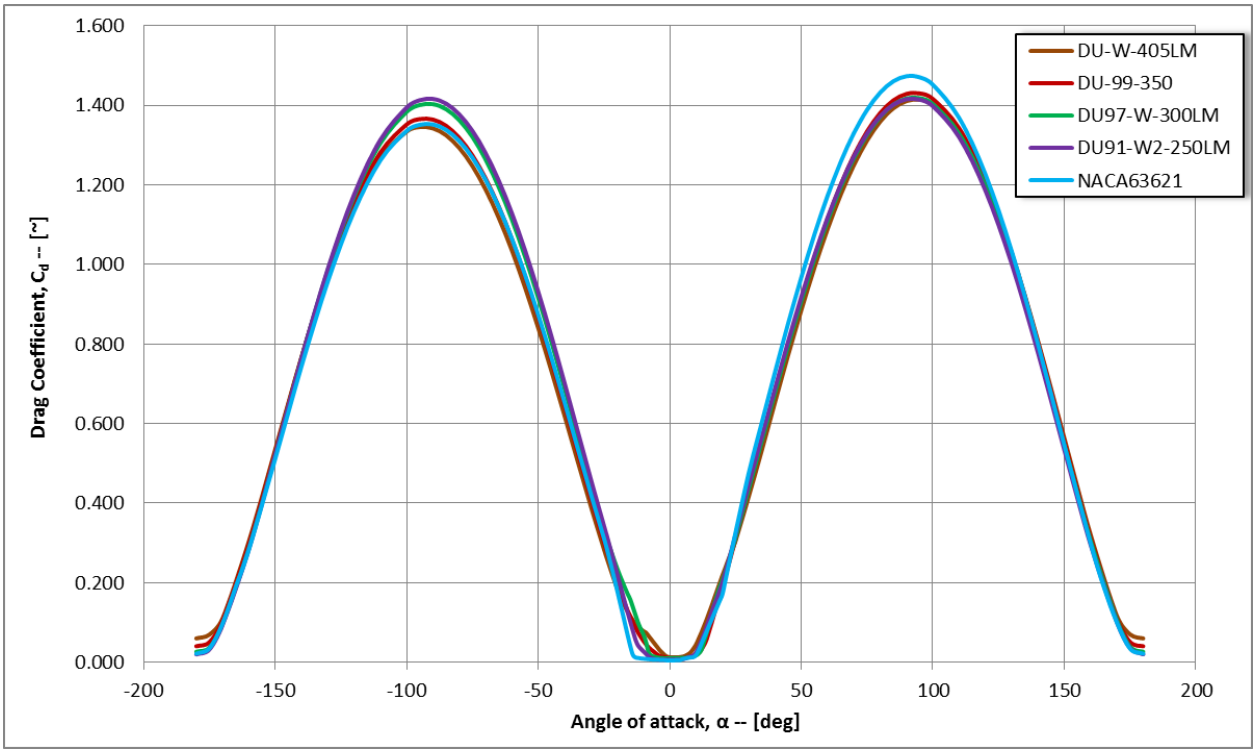

Figure 22. Aerodynamic Drag Data for Blade Section Airfoils

6.3. Structural Analysis

This section summarizes the analyses of the preliminary structural design of the 56-m blade. The aerodynamic blade planform designed in the previous task serves as a basis for preliminary structural design. It should be noted that this structural design, while performed with exceptional attention to detail and engineering judgment indicative of the standards of practice of the wind industry, is not representative of a certification-worthy blade. This section is intended to outline the general structural characteristics of the 56-m blade, including maximum blade deflection, first and second natural frequencies of vibration in bending, and material exertion factors.

An equivalent beam model consisting of finite element models of multiple spanwise stations is built for the present analysis. An in-house blade sectional analysis tool to analyze the

blade structure at multiple, distinct span-wise sections is used for this task. This tool has been previously designed by WEI and is used for all blade structural designs. Each section contour is divided into a number of sections, and the laminate structure in each region is defined. The code meshes the cross-section of the laminated structure with nine-node two-dimensional elements. The output from the blade sectional model are 4x4 beam-equivalent stiffness and compliance matrices (including axial tension, edgewise bending, flapwise bending, and torsional degrees of freedom) and the 6x6 inertial matrix. These matrices can be used to construct an equivalent beam model of the blade suitable for dynamic simulations. If sectional loads are provided, the program will also calculate full strain fields on all elements and find the maximum strain values for all components for all materials. In the past, an exceptional agreement between this model and the full FEA, generally within 1-2% in strain estimation has been achieved.

The preliminary loads used for the design and analysis of the 56m blade are established from the a preliminary loads estimation software used for determining rotor blade steady aerodynamic performance and rigid aeroelastic loads under specific critical design load cases as per the 2010 guidelines of Germanischer Lloyd [53]. The blade has been analyzed with respect to the following structural design considerations:

- Peak Deflection Constraints
- Modal Analysis Constraints
- Static Strength Analysis
    - Ply-by-ply analysis of the fiber-reinforced structure using LaRC03 failure criteria [50-51] for fiber failure (FF) and inter-fiber failure (IFF)

6.4. Results

6.4.1. Mass and Stiffness

The mass distribution of the blade was determined using the equivalent beam model as well as other internal tools used for modeling the preliminary structural design. These models assume a preliminary estimation of an assumed configuration for the root fastener concept, and account for the mass of the root fasteners, except for root studs. Figure 23 displays the mass distribution for the 56m blade. The trend of the plot shows that most of the mass is concentrated between 25% and 75% sections of the blade span. At the blade root, mass is concentrated at the root due to the root ring, and the trend monotonically decreases as one approaches the maximum chord station. The plot also shows a general decreasing trend as one approaches the tip whereby, overall mass of the blade decreases due to structural changes/termination points to various structural components of the blade, such as the spar cap and shear webs. The total blade mass and breakdown can be found in Table 13.

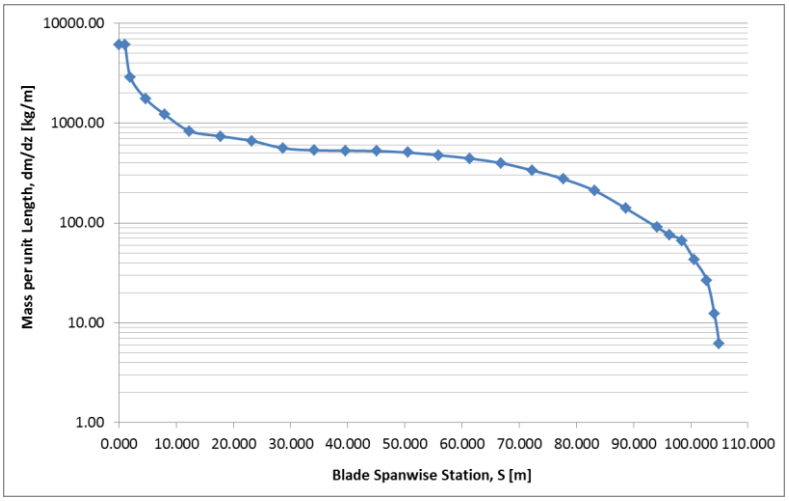

Figure 23. Mass Distribution for the 56-m blade

Table 13. Bill of Materials for 56-m blade (in kg)

	Fiber/Foam	Resin	Adhesive
Skins	2214	891	
Root Reinforcement	457	184	
TE	297	121	
Balsa	378	331	
SparCaps	2221	905	
Web Flanges	100	40	149
TE Overlam	76	31	
LE Bond	137	55	123
Paint			150
Shear Webs	763	307	
TE Bond			275
Total (kg)			10205

6.4.2. Deformation

For this turbine configuration, the blade tip deflection is constrained to be no more than 18% of the total blade length, Δx=10.1m. The present equivalent beam model predicts a maximum out-of-plane deflection of 8.5m (15.2% of the total blade length) under extreme flapwise loading. The model results also predict an in-plane deflection of 0.65m under the same loading conditions.

Figure 24 is a spanwise plot of the out-of-plane (or flapwise) deflection, and Figure 25 is a spanwise plot of the in-plane (or edgewise) deflection of the 56-m blade. Under the blade extreme flapwise loading,

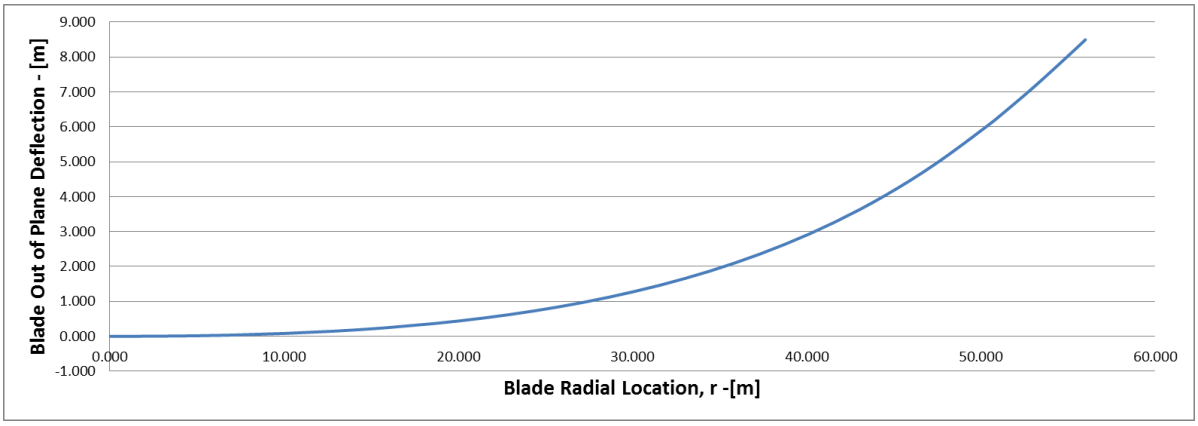

Figure 24. Out-of-Plane Deflection of the 56-m Blade under Maximum Flapwise Loading

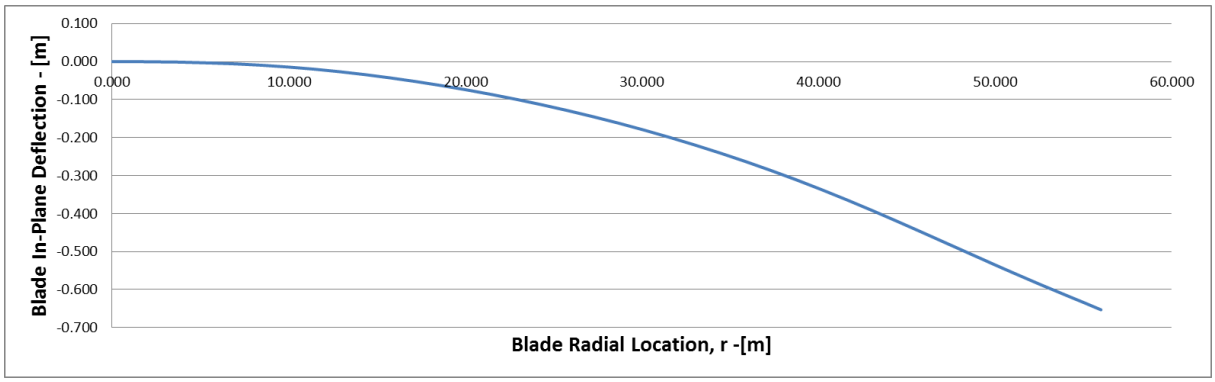

Figure 25**. In-Plane Deflection of the 56-m Blade under Maximum Edgewise Loading**

6.4.3. Modal Analysis

A modal analysis was conducted with inputs determined from WEI's internal sectional FEA tool using the NWTC Modes program which calculates uncoupled mode shapes from the beam equivalent model.[52] Table 14 describes the frequency characteristics.

General blade design practice is to design and optimize the blade structure such that the target range for first flapwise frequency, $f_{1,}$ is defined as 3P+10% < f_1 < 3P-10%. Additionally, the target range for first edgewise frequency, $f_{2,}$ is defined as $f_2 > 1.35*f_1$ and 6P+5% < f_2 < 6P-5%.

In other words, the target range for first flapwise frequency shall be outside of the range of 3 times the rotational frequency of one revolution of the rotor. Similarly, the target range for first edgewise frequency shall be outside the range of 6 times the rotational frequency of one revolution of the rotor, and that the first edgewise frequency is at least 35% higher than the first flapwise frequency to avoid resonance issues related to the first modes of flap and edge. The 56-m blade has desirable frequency characteristics as Table 14 shows the isolated blade first flapwise frequency to be just below 3P+10% and the first edgewise frequency to be below 5P-5% at rated shaft speed during normal operation. These isolated blade frequencies stay clear of any resonance with 3P and 6P. In addition, the first edgewise frequency is about 41% higher than first flapwise frequency.

Table 14. Summary of the 56m Blade Frequency Characteristics

Calculated Frequencies			
Rotating	1st Flap	0.7271	Hz
	1st Edge	1.0223	Hz
Stationary	1st Flap	0.6592	Hz
	1st Edge	0.9860	Hz

6.4.4. Exertion Factors and Stiffness Distribution

Each component has been analyzed for fiber failure (FF) and inter-fiber failure (IFF) as per the method described in [50] and [51]. For the glass fiber-reinforced material the strength was assessed on a ply-by-ply basis. Unidirectional glass material was analyzed for fiber failure (FF) and inter-fiber failure (IFF) using the methods of Puck. The multi-axial glass fabrics were analyzed for FF and IFF using the LaRC03 criteria. A detailed description of the theory and methods applied using LARC03 in the FF and IFF evaluation of the 56m blade can be found in Reference 50 and 51.

The static exertion factors of the fiber-reinforced plastic (FRP) components can be seen in Figure 26 through Figure 27. It should be noted that discontinuities correlate with locations of ply drops in the laminate structure. Static exertion factors greater than 1 indicate strain to failure at the ply level in the primary fiber direction (fiber-failure) and transverse fiber direction (inter-fiber failure). All exertion factors presented in the plots below are below 1.0.

The exertion factors in the spar cap of the 56m blade is shown to be maximized and optimal under extreme blade loading. This indicates that the blade spar cap was designed to the strength of the carbon materials in the spar cap, while under consideration for maximum blade deflection constraints. The exertion factors in the blade shell and shear webs show sufficient margin in the design. The general trends of the plots below also show the overall buildup of laminate structure in various structural components of the 56m blade from blade root to blade tip, with most of the structure concentrated towards 25% through 75% of the blade span.

The stiffness distributions for the blade are calculated using the equivalent beam model at each defined station. Figure 28 through Figure 29 display the results of these calculations.

The distributed blade structural properties are reflected in the figures below, showing the flapwise, edgewise and torsional section stiffness at each station, given about the principal structural axes of each cross section as oriented by the structural twist angle. The blade's sectional stiffness properties are used to determine the isolated blade modal frequencies, and are used as input for aeroelastic simulations of the 2MW wind turbine in FAST or GH BLADED.

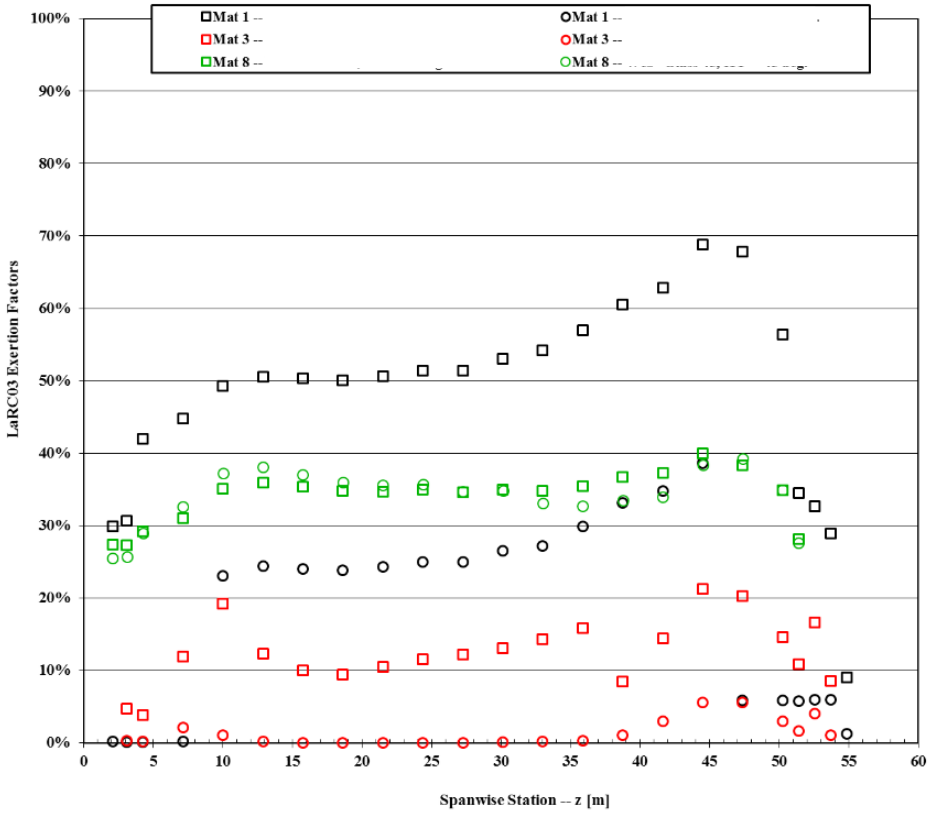

Figure 26. Sectional Exertion Factors for Shell Glass Materials of the 56-m Blade

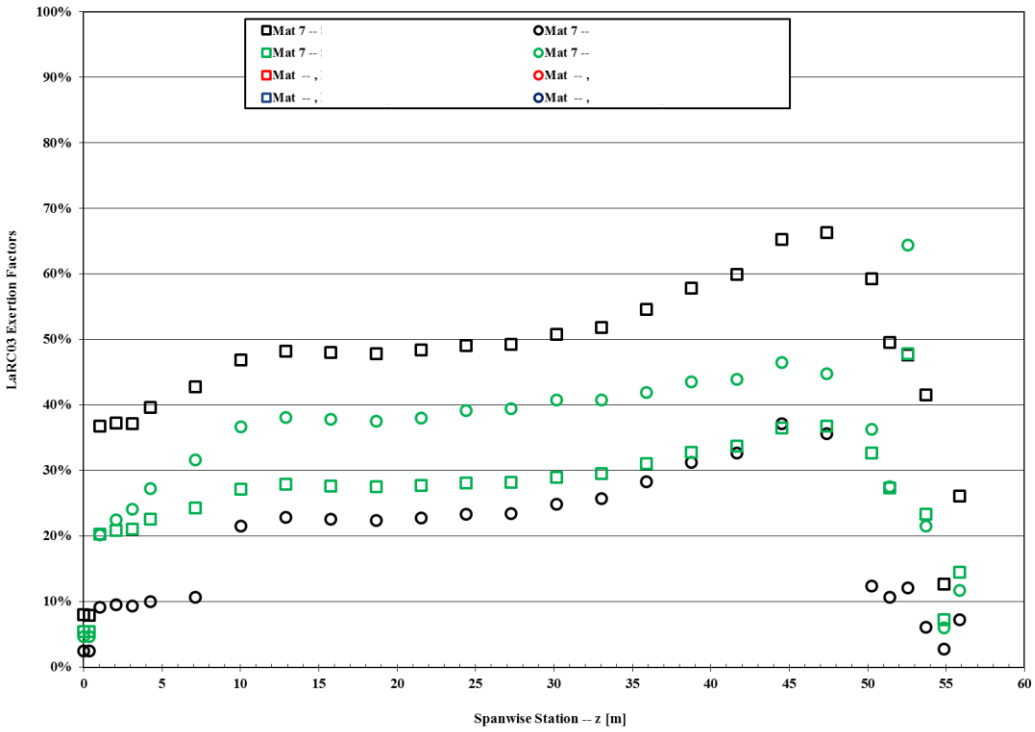

Figure 27. Sectional Exertion Factors for Girder Materials of the 56-m Blade

The overall trend in the blade stiffness shown in the following plots is smooth and monotonically decreasing from blade root to blade tip of the 56-m blade. It can be observed from the charts below that the trend tapers off at the tip, due to changes/termination points of some of the structural components within the blade structural layout.

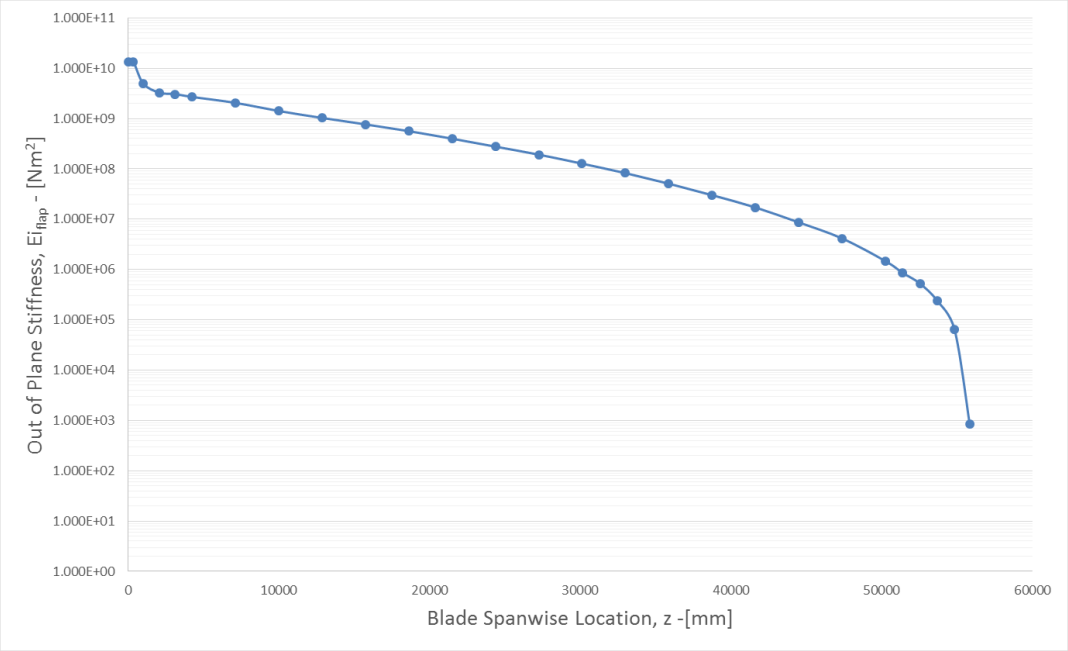

Figure 28. Out-of-Plane Stiffness Distribution for the 56-m Blade

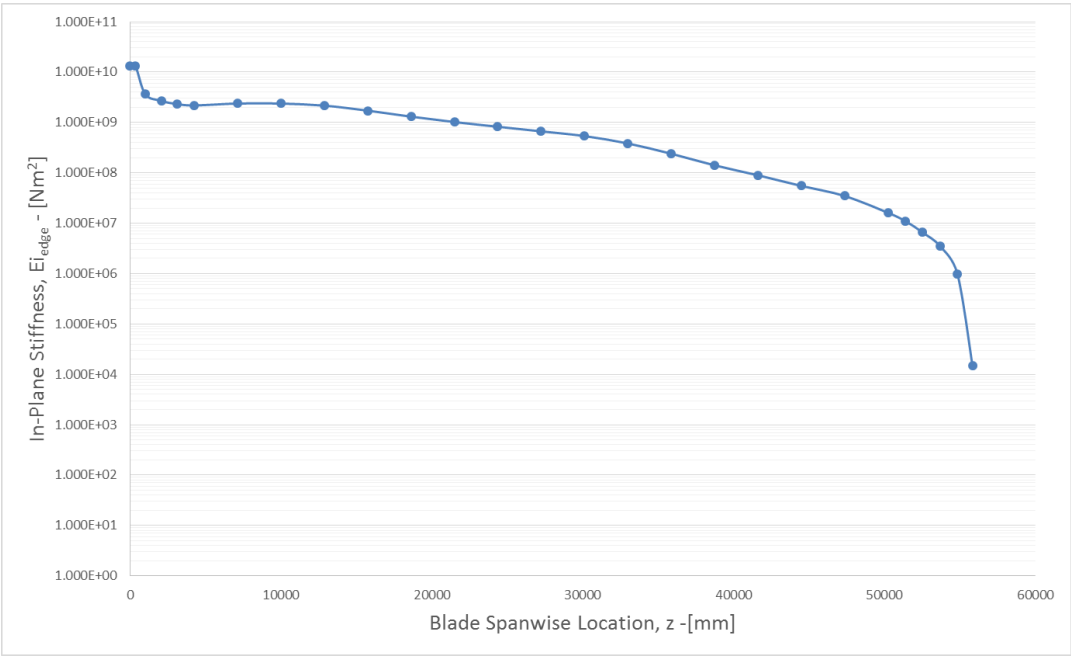

Figure 29. In-Plane Stiffness Distribution for the 56-m Blade

6.5. Loads Analysis

In order to perform the loads analysis, a widely used code in the wind industry i.e. GH-Bladed is used. GH-Bladed Bladed is the industry standard integrated software package for the design and certification of onshore and offshore turbines. It provides users with a design tool that has been extensively validated against measured data from a wide range of turbines and enables them to conduct the full range of performance and loading calculations. [50]

Based on the aerodynamic and structural design, an aero-structural model is created. This model is input into GH-Bladed and a limited set of loads simulations are carried out. The design load cases chosen are as per the IEC guidelines. The list of the design load cases are presented in Table 15. An OEM's 2MW turbine model is used for the loads analysis hence the details of the drivetrain configuration and other mass and inertia pertaining to the turbine will not be shared in this document.

Based on the results obtained from the loads analysis, it is noted that the maximum blade root bending moment results from an ECD (Extreme Coherent Gust with Direction Change) case. This loads case is independent of the design class. As compared to the predicted loads from BladeOpt, we see a ~6% difference in the predicted versus calculated blade root bending moment. It should be noted that since we have simulated a limited set of cases, we would expect the final loads to increase by 4-5%. Given that the structure has been designed to the BladeOpt loads, minimal design changes will be expected in the detailed structural design phase.

Table 15 Loads Analysis - Design Load Cases

DLC_1_1_NTM	Vrated, Vrated +/-2m/s, Vcutout
DLC_1_3_ECD	Vrated, Vrated +/-2m/s
DLC_1_5_EOG	Vrated, Vrated +/-2m/s, Vcutout
DLC_6_1_3EWM50	Vrated, Vrated +/-2m/s, Vcutout

Table 16 Loads Analysis Results

		Mx	My	Mxy	Mz	Fx	Fy
	Load Case	**kNm**	**kNm**	**kNm**	**kNm**	**kN**	**kN**
MAXIMUM	DLC_1_1_NTM_V12A_Y8	4128.44	5679.90	7021.76	-59.89	163.75	-183.70
MINIMUM	DLC_1_1_NTM_V25A_Y-8	-3205.17	1256.81	3442.77	-39.87	28.57	159.53
MAXIMUM	DLC_1_3_ECD_V10_NDC	2416.76	7456.77	7838.63	-73.56	224.96	-114.80
MINIMUM	DLC_1_1_NTM_V25A_Y8	2408.55	-6033.70	6496.66	168.00	-175.29	-66.98
MAXIMUM	DLC_1_3_ECD_V10_NDC	2665.18	7419.09	7883.28	-73.84	224.35	-128.51
MINIMUM	DLC_6_1_3ewm50_v38a_Y0_U8	-1.65	-0.78	1.82	10.46	-18.95	8.02
MAXIMUM	DLC_1_1_NTM_V25A_Y8	2408.55	-6033.70	6496.66	168.00	-175.29	-66.98
MINIMUM	DLC_6_1_3ewm50_v38a_Y150_U8	-67.34	4866.33	4866.80	-103.95	226.54	-11.71
MAXIMUM	DLC_6_1_3ewm50_v38a_Y120_U8	-12.18	5257.94	5257.95	-99.83	250.96	-8.32
MINIMUM	DLC_6_1_3ewm50_v38a_Y-120_U8	-463.80	-5394.13	5414.04	107.67	-240.61	30.08
MAXIMUM	DLC_1_1_NTM_V23A_Y-8	-3064.86	791.16	3165.33	-41.90	13.82	160.89
MINIMUM	DLC_1_1_NTM_V09A_Y0	4052.96	5576.78	6893.99	-39.29	172.57	-191.69

7. Verification and Validation of CFD Tools

In order to perform verification and validation of CFD tools, the data set from reference [45] is chosen. The reason for the choice of this reference is since it provides wind tunnel test data for all configurations i.e. clean airfoil data, test data and dynamic inflow conditions as well. In order to perform CFD analysis, STAR CCM+ code is used. The details of this study are provided below.

7.1. CFD Analysis of LS(1)-0417MOD Airfoil

In order to perform a verification and validation exercise on the LS(1)-0417MOD airfoil, a CFD analysis is performed. This analysis is carried out using STAR CCM+ software. STAR CCM+ software allows the user to perform both 2D and 3D analysis of complex flows. [54] STAR CCM+ has an inbuilt meshing tool and a variety of RANS models that are used for fluid flow analysis.

For this study, the airfoil was modeled as an infinite 3D wing, replicating the wind tunnel test model. The results obtained from this analysis are compared to the wind tunnel test data for the both the clean configuration as well as the vortex generators configurations.

7.1.1. Clean Airfoil Configuration

For the clean configuration, the details of the domain calculations are provided in Table 17. The values provided in the table below are the final mesh parameters determined after performing a grid independence study.

Table 17 Domain and Mesh Data for the Clean Airfoil Configuration

Parameter	Value
Upstream Length	5c
Downstream Length	20c
Normal Direction Length	8c
Mesh Count	~10million

For the clean configuration, multiple angles of attack are simulated and the corresponding aerodynamic performance parameters are recorded and graphed. The inlet is treated as a velocity inlet. The pressure far field is also treated as a velocity inlet. The operating Reynolds number based on chord was 1 million based on the basic assumptions that the flow field is completely turbulent. k-ω turbulence model was used as a solver. Second Order Upwind was used as the discretization scheme. Table 18 presents the parameters for the fluid analysis. Figure 30 shows the domain used for the analysis. Figure 31 shows the mesh for the entire domain and Figure 32 shows the mesh around the airfoil. A wake refinement based on the angle of attack is added in order to ensure better accuracy of the results.

Table 18: Fluid Analysis Parameters

Input Variable	Value Entered/Setting
Model	k-ω Turbulence Model
Inlet	Velocity inlet
Outlet	Pressure Outlet
Pressure Farfield	Velocity Inlet
Symmetry Plane	Symmetry
Airfoil	Wall
Reference Values	Initialized from Inlet
Discretization Scheme	Second Order Upwind
Residuals	1e-06
y^+	Less than 3

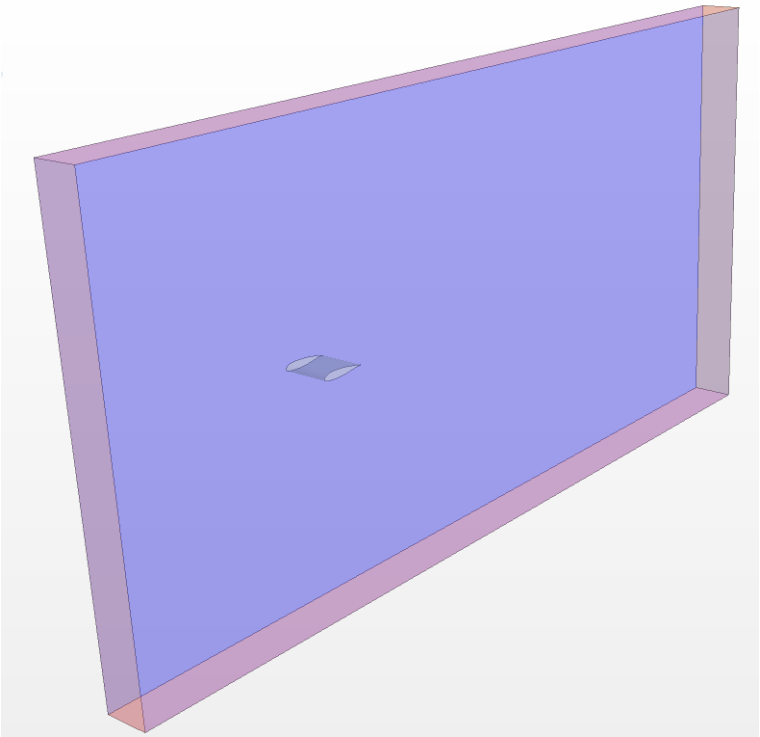

Figure 30: Domain Layout for clean configuration

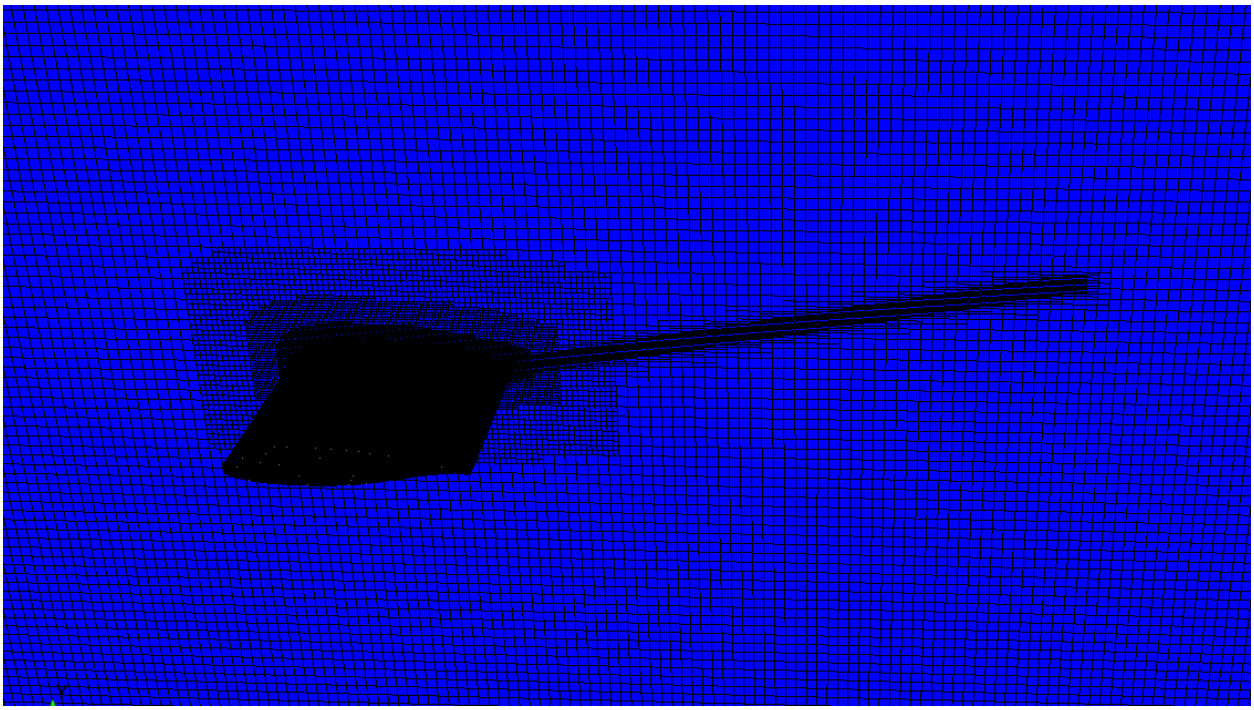

Figure 31: Mesh used for clean configuration

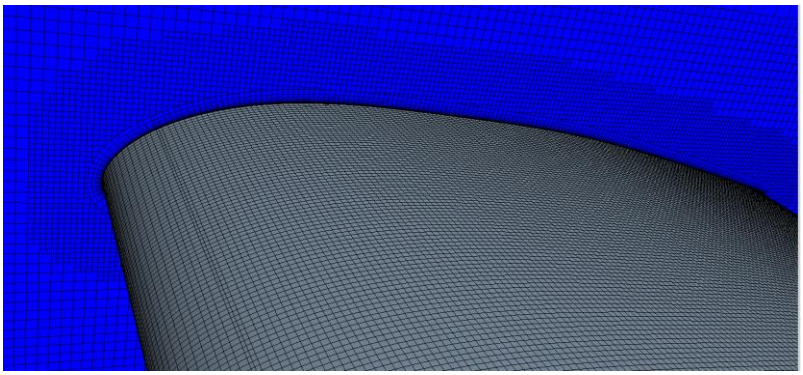

Figure 32: Mesh used for clean configuration (Boundary Layer)

7.1.2. Results for Clean Airfoil Configuration

The results for the clean airfoil configuration are presented in this section. A direct comparison to the wind tunnel test data is made and a good match is obtained to the wind tunnel test configuration. The wind tunnel test is carried out at Re_c = 1.0e6 million and the fluid analysis is carried out at the same Reynolds number as well. Figure 33 presents the comparison between the wind tunnel measurement and the simulated data.

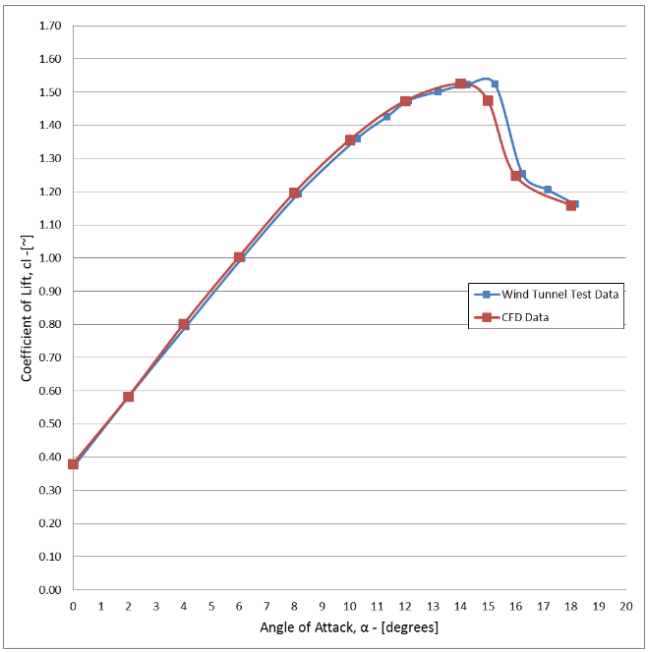

Figure 33: Comparison of Lift Curve variation with angle of attack for wind tunnel test data and CFD data

7.2. Vortex Generators Airfoil Configuration

For the vortex generators configuration, the details of the domain calculations are similar to those for the clean configuration. Type A vortex generators on the LS(1)-0417MOD airfoil is simulated. The details of this configuration are provided in reference [45]. The setup for the fluid flow analysis is the same as the clean configuration. Figure 34 shows the domain layout for the vortex generators configuration.

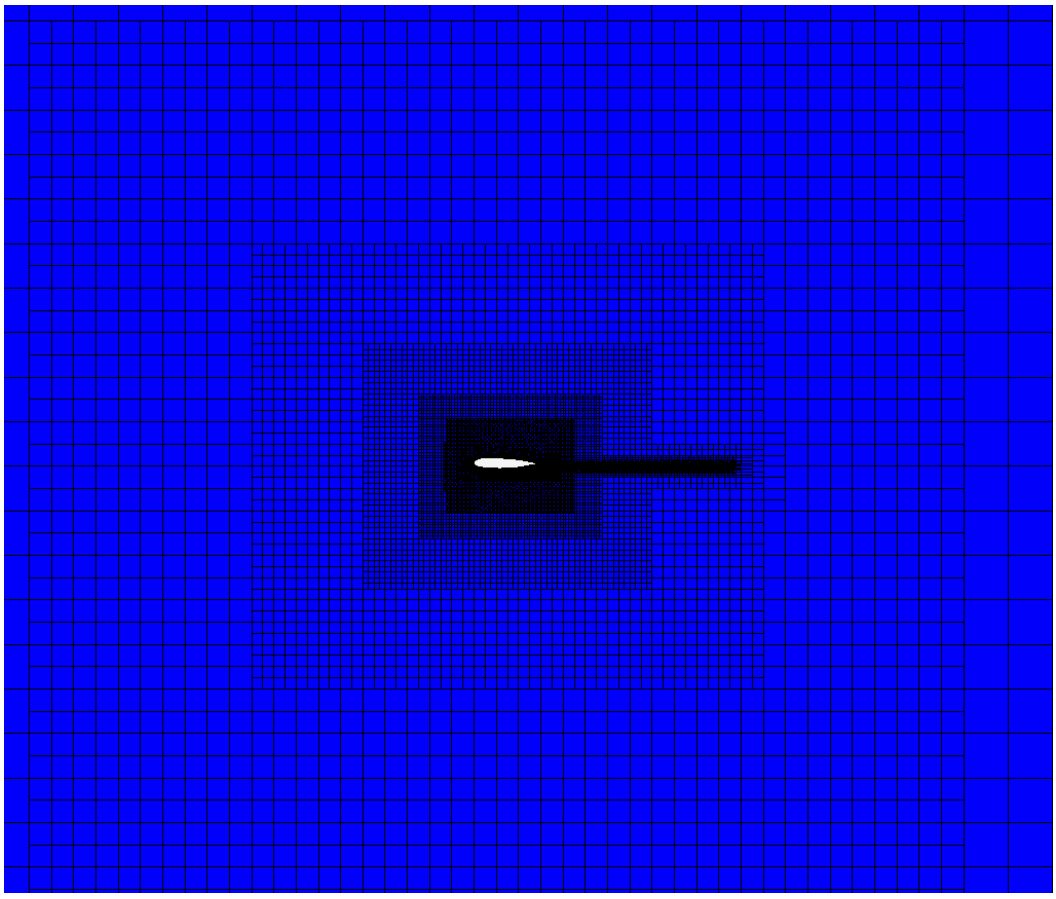

Figure 34: Mesh used for Vortex Generator configuration

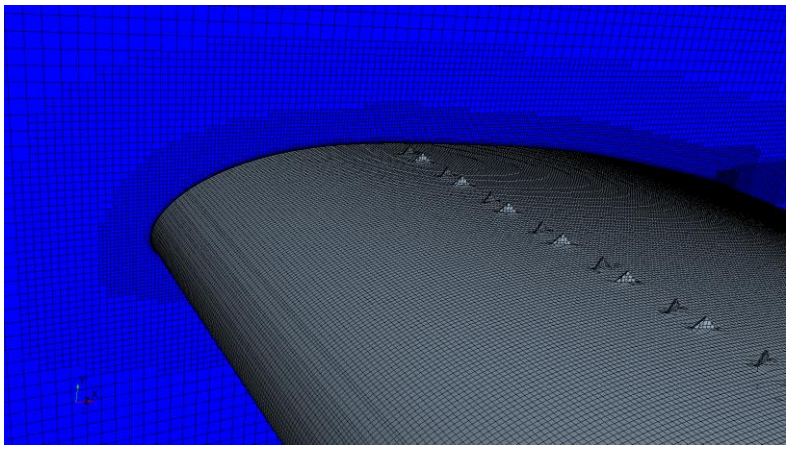

Figure 35: Mesh used for Vortex Generator configuration (Boundary Layer)

7.2.1. Results - Vortex Generators Airfoil Configuration

The results for the clean airfoil configuration are presented in this section. A direct comparison to the wind tunnel test data is made and a good match is obtained the wind tunnel test configuration. The wind tunnel test is carried out at Re_c = 1.0e6 million and the computational fluid analysis is carried out at the same Reynolds number as well. Figure 36 presents the comparison between the wind tunnel test data and the simulated data.

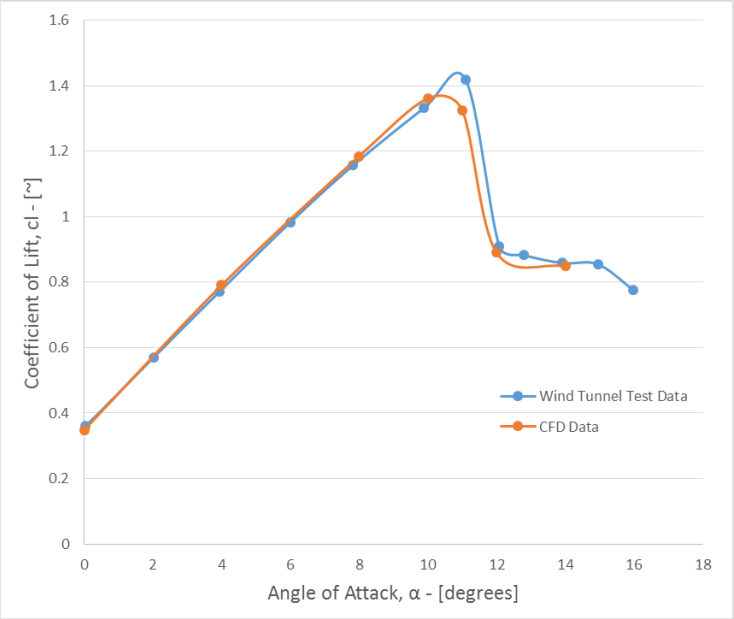

Figure 36: Comparison between wind tunnel test data and CFD analysis

7.3. CFD Analysis of FB-47 airfoil

Based on the analysis performed for the above two configurations, numerical simulations are carried out for the FB-47 airfoil. This airfoil is used in the transition region of the blade. The mesh and flow parameters are similar to those for the LS(1)-0417MOD airfoil. Below is a summary of the flatback airfoil section which was used for the blade aerodynamic design at the maximum chord location. The custom designed transition 47.29% thick flatback airfoil (WEI-FB-47) was analyzed using CFD and determined to be suitable for aerodynamic modeling of the inboard transition region of the rotor blade.

In the following graphs, the aerodynamic lift and drag data is presented. Analysis is performed for small angle of attack range to determine the linear range up to the pre-stall aerodynamic characteristics of the abovementioned airfoil. The deep stall aerodynamic data of the flatback airfoil was interpolated from DU40 airfoil data. CFD results are also presented in this section with pressure and velocity contour plots to show the overall

aerodynamic performance of this airfoil at small angles of attack to post-stall angle of attack range.

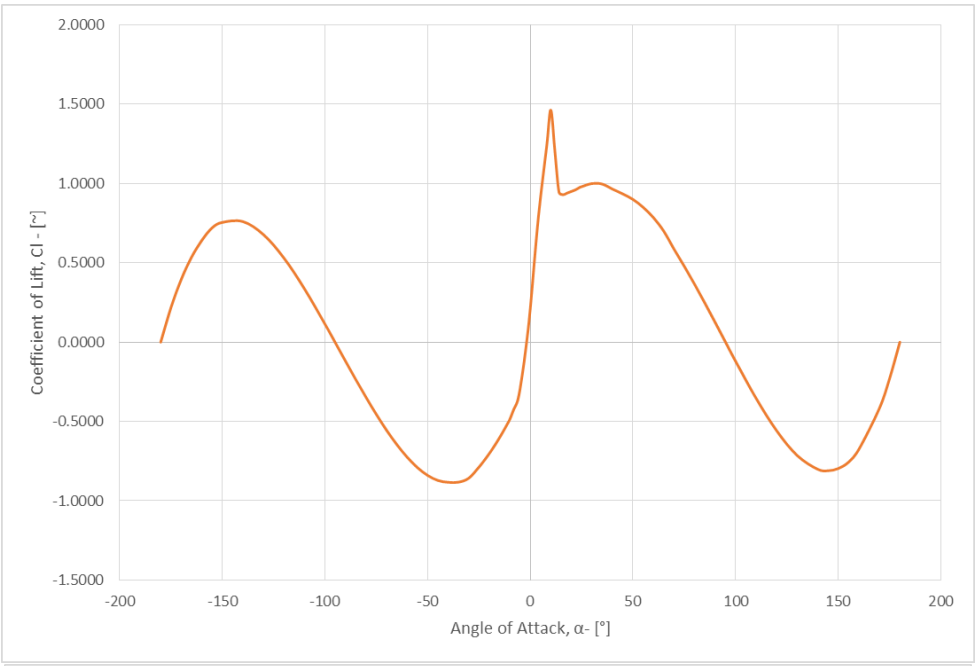

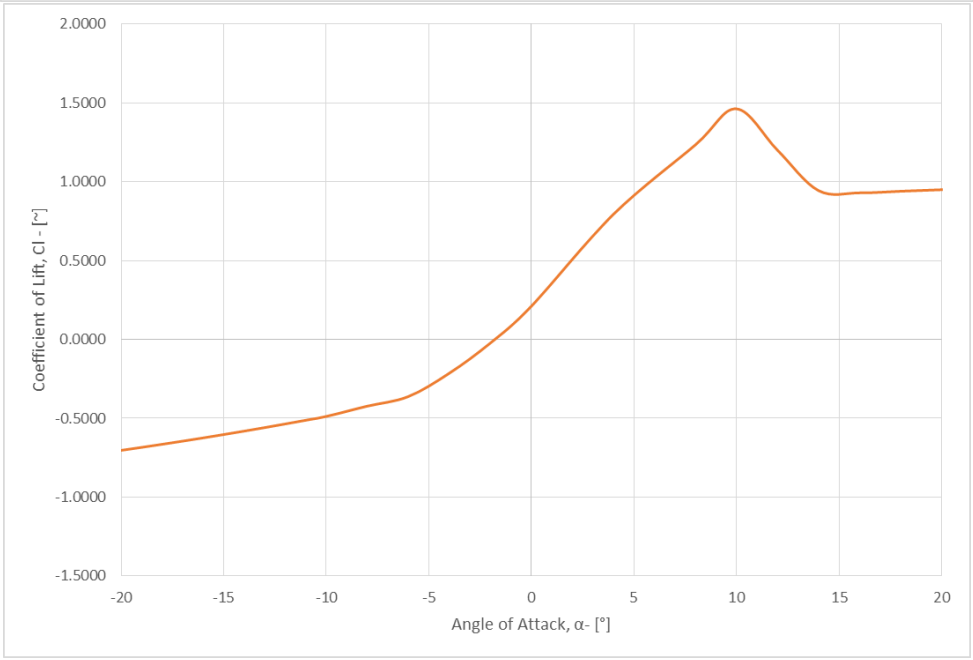

Figure 37. Aerodynamic Lift Curve for Custom Flatback Airfoil WEI-FB-47

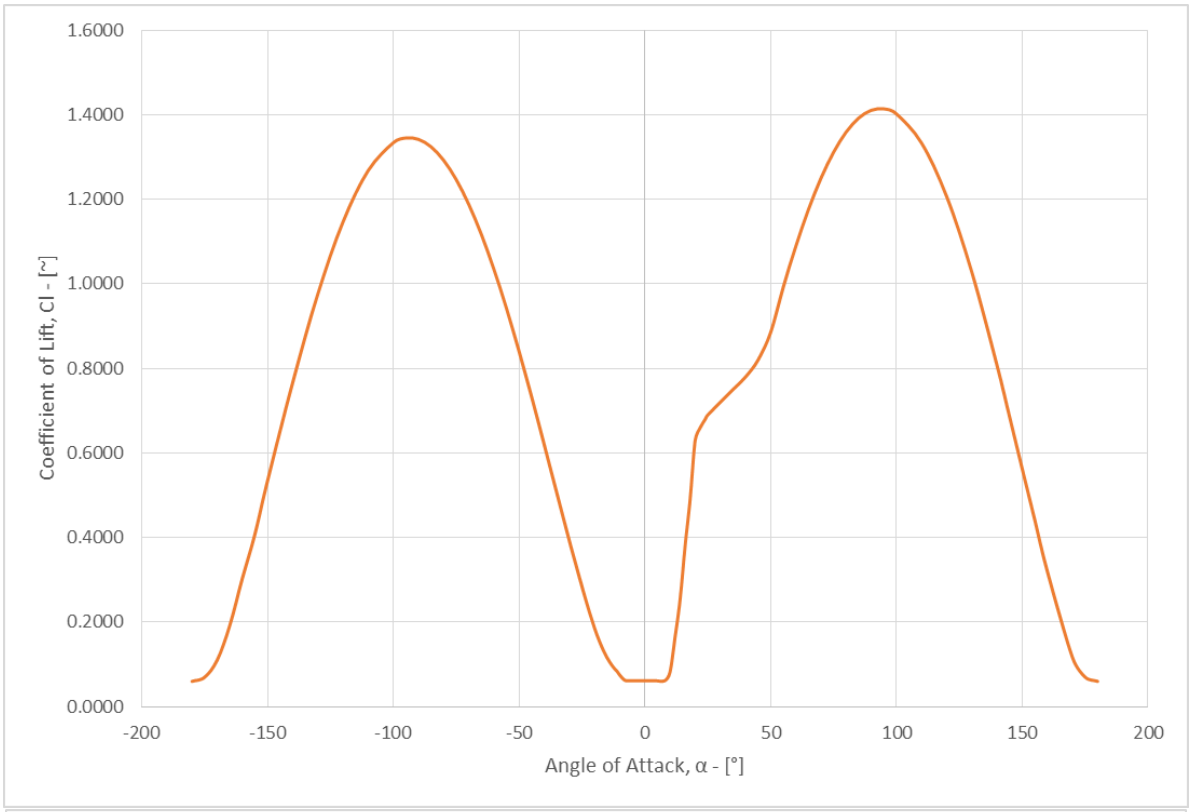

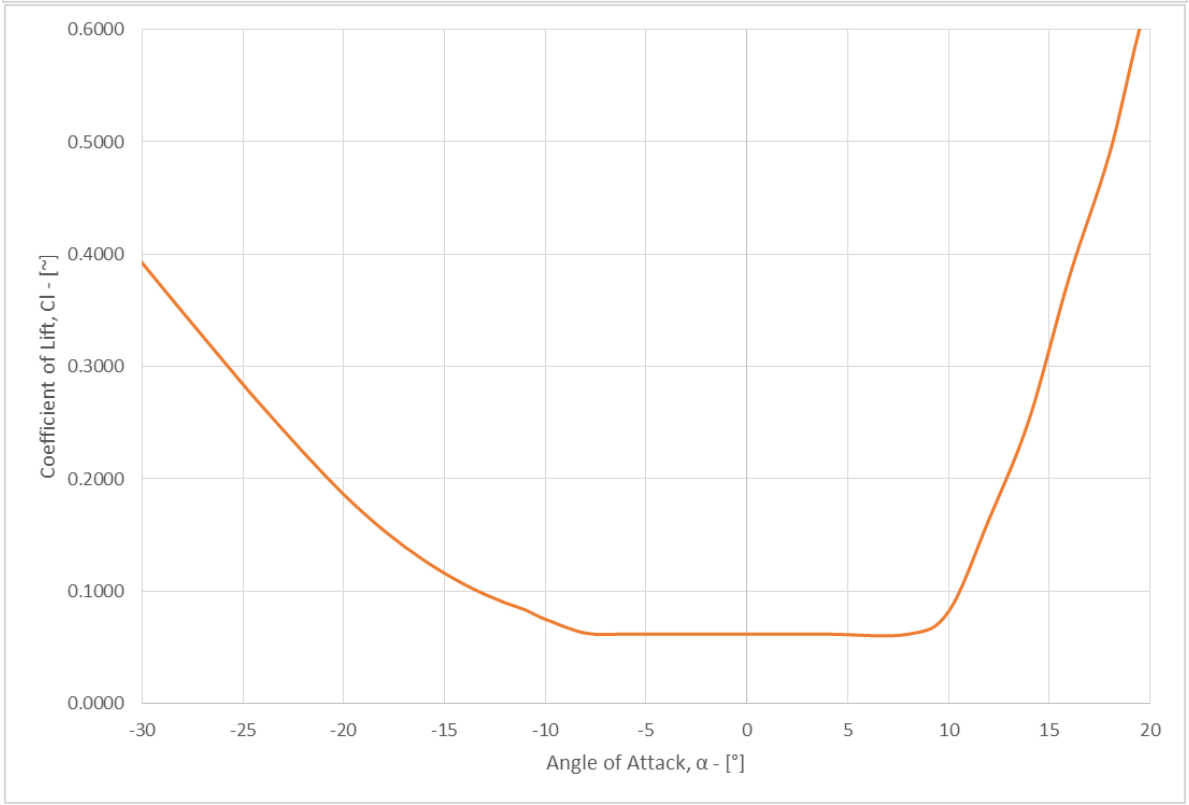

Figure 38. Aerodynamic Drag Data for Custom Flatback Airfoil WEI-FB-47

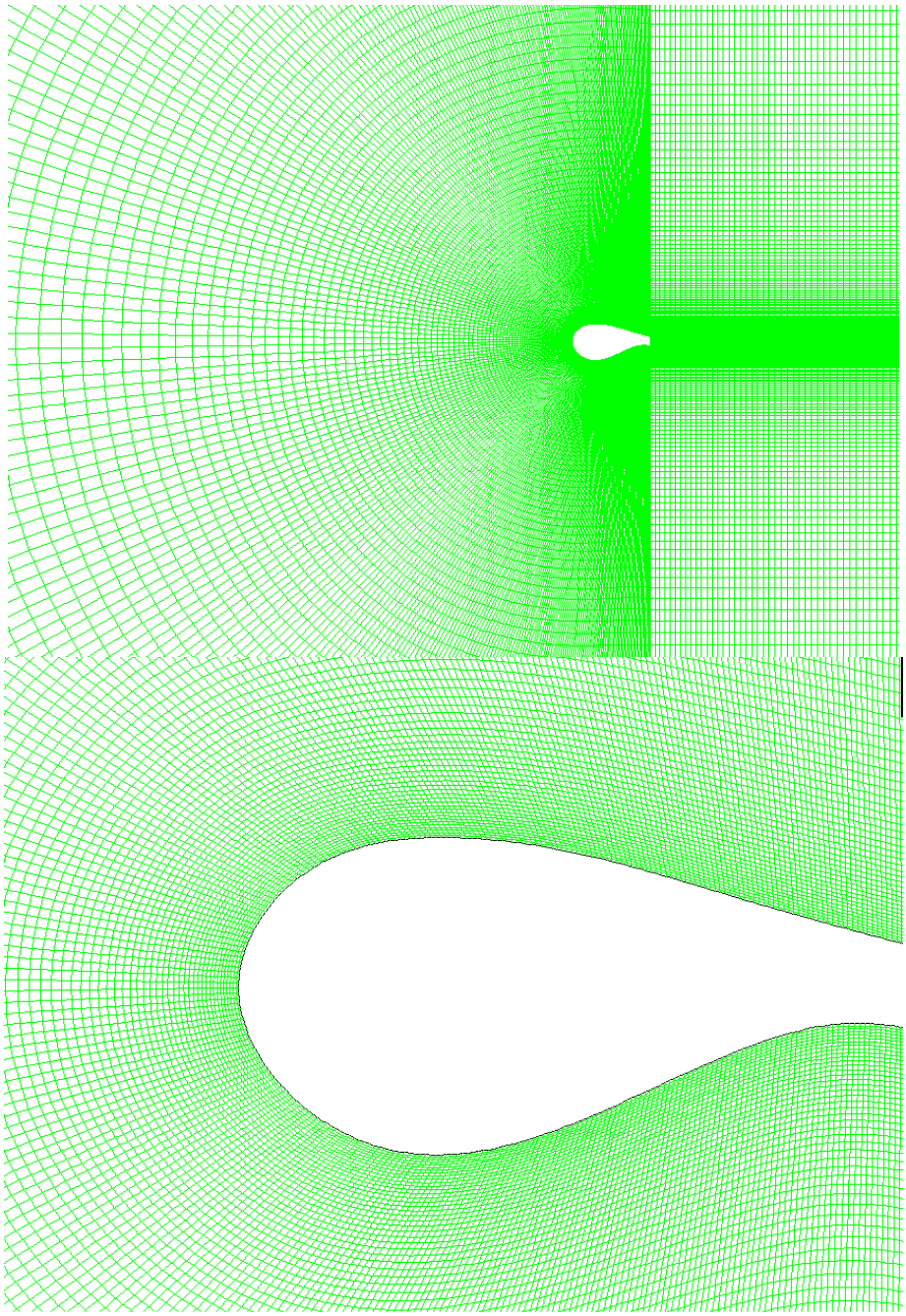

Figure 39. CFD Mesh Grid for WEI-FB-47 Airfoil Section

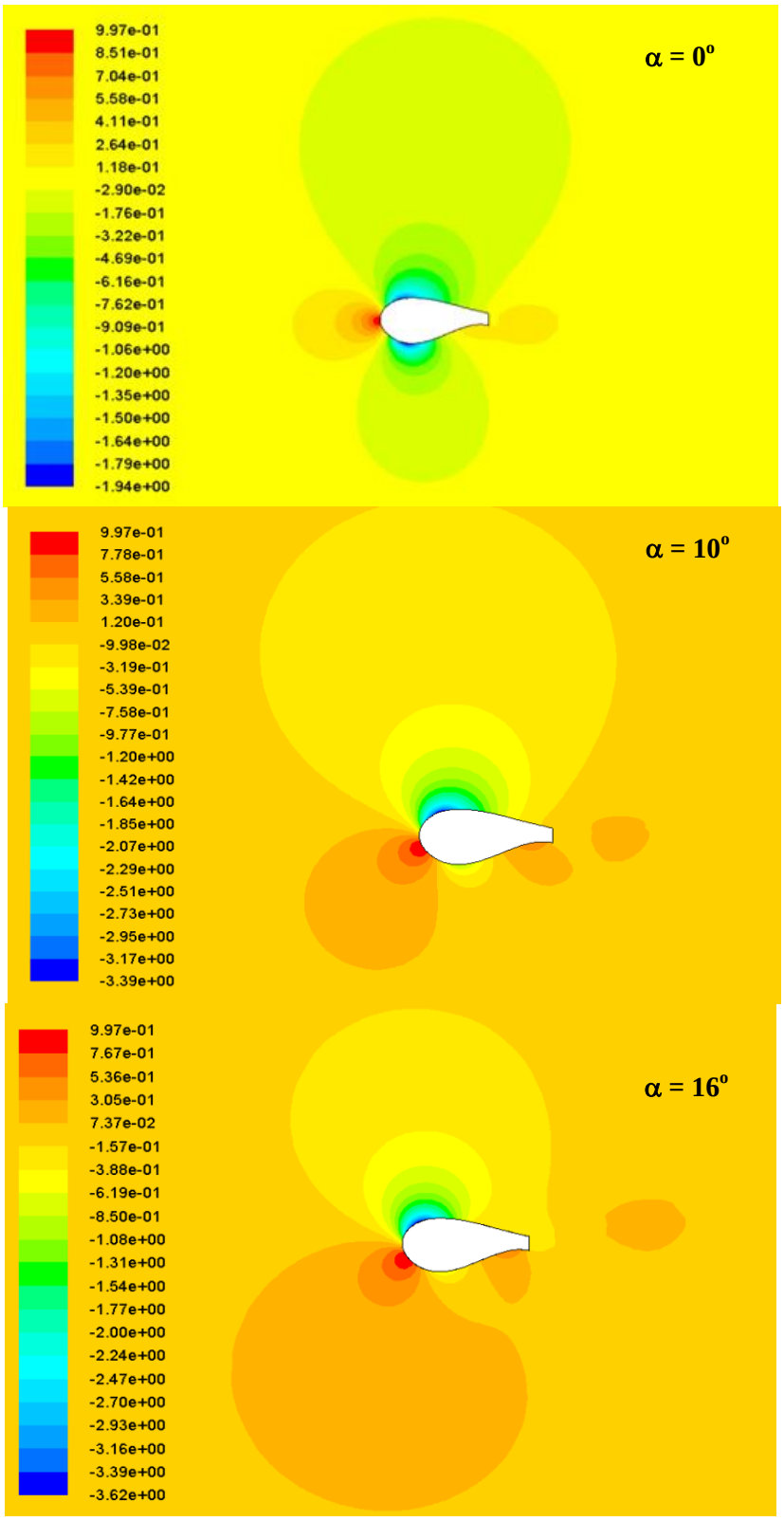

Figure 40. Pressure Contour Plots for WEI-FB-47Airfoil at AOA of 0°, 10° and 16°.

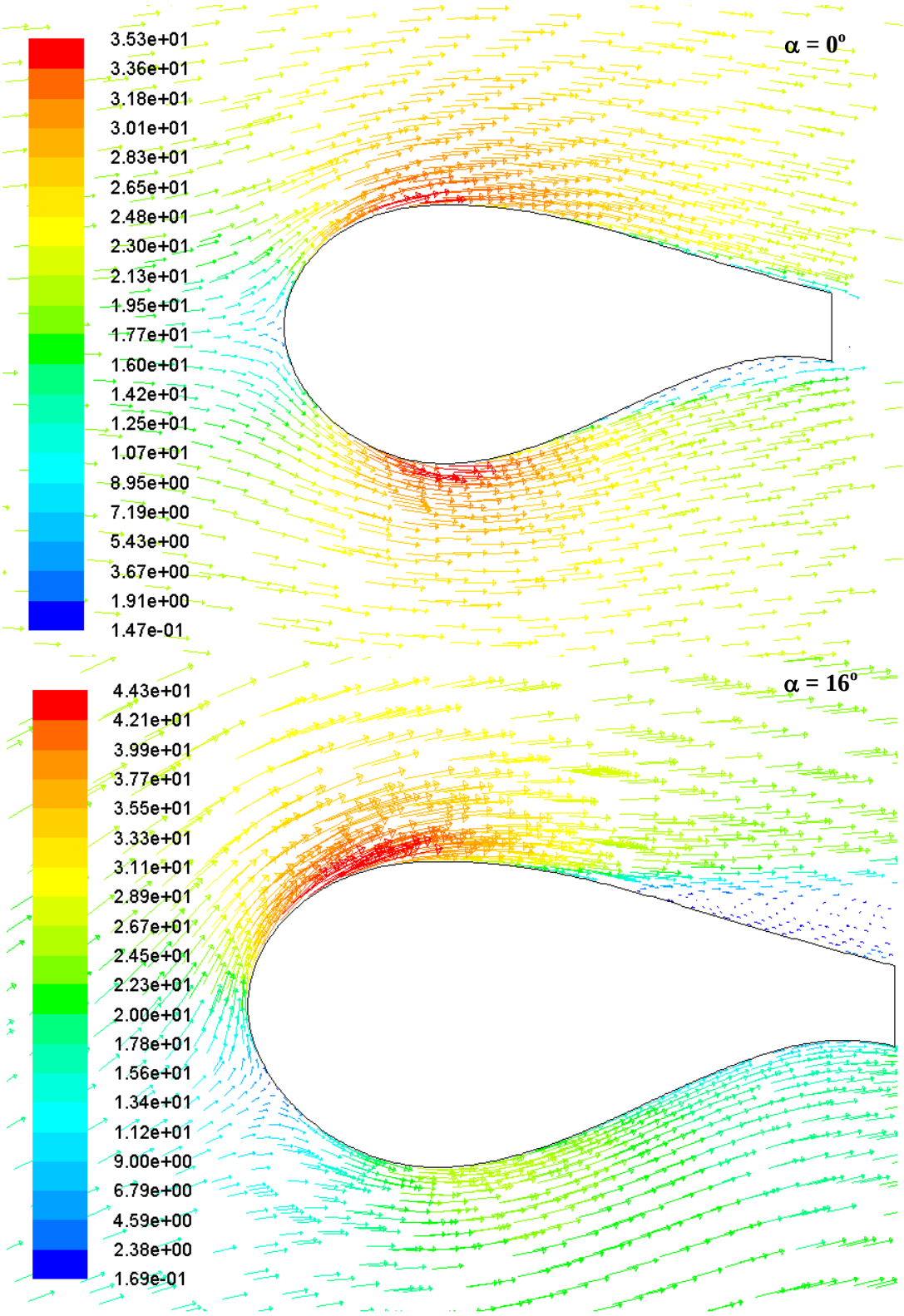

Figure 41. Velocity Magnitude and Vector Plot for WEI-FB-47 Airfoil.

7.4 Vortex Generator Design and Analysis

Procedures are developed for the validation exercise for airfoil with and without vortex generators as described in the previous section. Using these techniques, FB47 and NACA 63621 airfoils with and without vortex generators are simulated. In order to determine the geometry of the vortex generator, a matrix is created using two design types namely, triangular and vane type vortex generators.

7.4.1 Vortex Generator Design Matrix

The matrix consisted of five geometries for each design type which are analyzed using Star CCM+ software. The performance characteristics for each configuration is recorded and the configuration providing the highest lift-to-drag ratio is selected as a final design. The matrix for the different vortex generators is provided in the table 19. All dimensions of length parameters are in mm assuming the airfoil chord as 1m.

Table 19: Vortex Generator Geometry Matrix

	A	B	C	D	E
h	3.38	4.57	5.08	5.59	6.10
L	8.44	8.69	9.65	10.62	11.58
l	6.76	9.14	10.16	11.18	12.19
λ	20.27	36.73	40.81	44.89	48.97
β (deg)	15°	15°	15°	15°	15°

Figure 43 shows the nomenclature of the vortex generator geometry used for the analysis. As an example, for Vortex generator A triangular design, the height h is 3.38mm for a 1m chord, the distance between a pair of the vortex generators L is 8.44mm, pitch λ is 20.3mm and the angle made with the inflow velocity is chosen as 15°. Figure 43 shows the two different types of vortex generator designs used for the analysis.

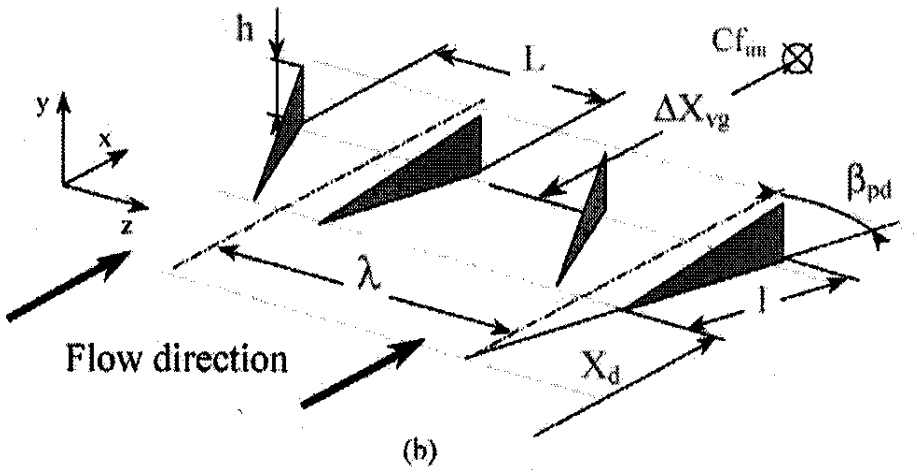

Figure 42. Vortex Generator Geometry Definition Schematic

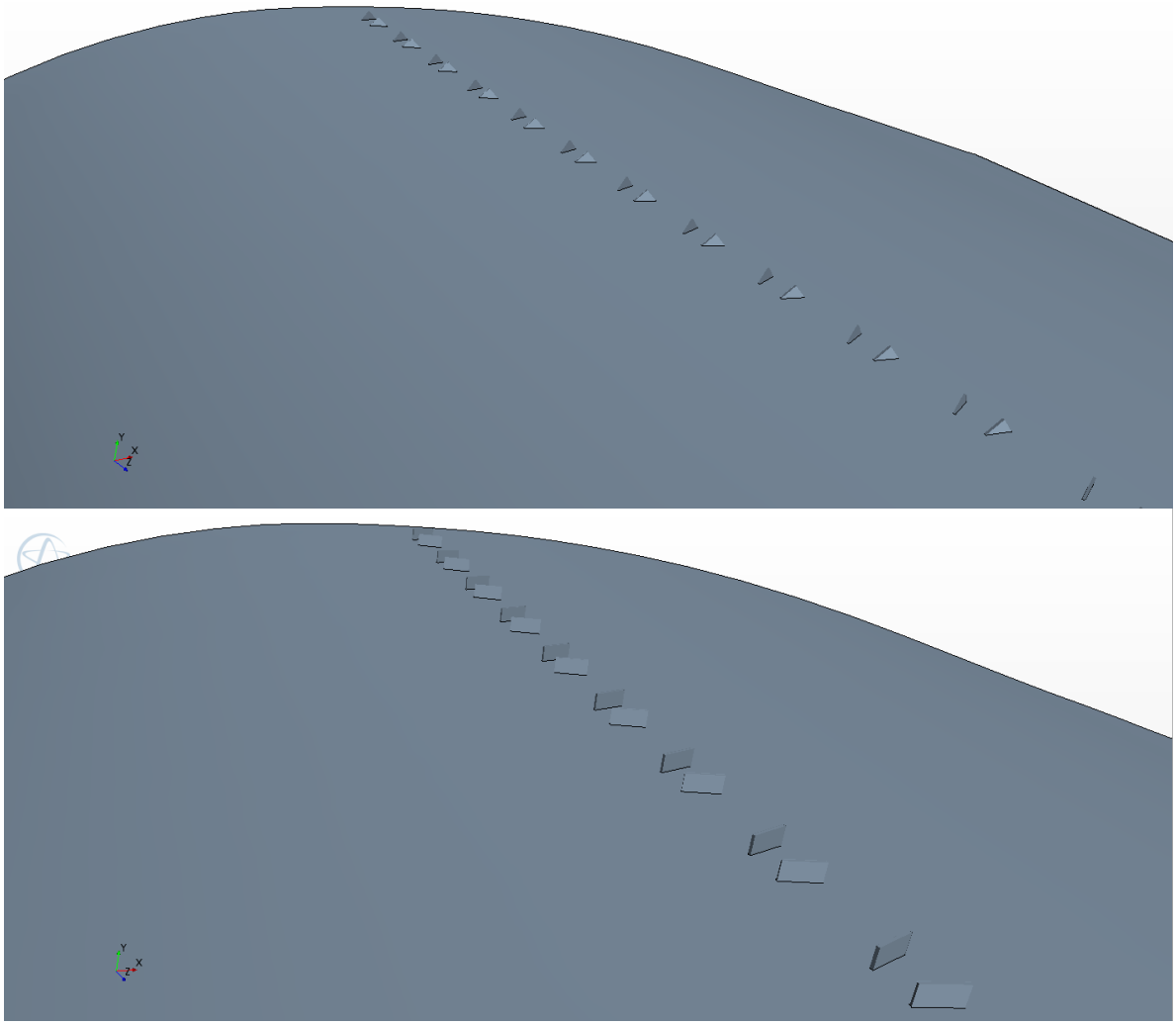

Figure 43. Vortex Generator Geometry – Triangular and Vane Type Design

7.4.2 Vortex Generator Fluid Flow Analysis

From the ten geometries selected for each airfoil, the goal was to analyze these configurations using STAR CCM+ and choose the highest performing configuration. A polyhedral mesh based approach is used for this analysis. A major advantage of polyhedral cells is that they have many neighbors (typically of order 10), so gradients can be much better approximated (using linear shape functions and the information from nearest neighbors only) than is the case with tetrahedral cells. Even along wall edges and at corners, a polyhedral cell is likely to have a couple of neighbors, thus allowing for a reasonable prediction of both gradients and local flow distribution. The fact that more neighbors means more storage and computing operations per cell is more than compensated by a higher accuracy. Polyhedral cells are also less sensitive to stretching than tetrahedral. Smart grid generation and optimization techniques offer limitless possibilities: cells can automatically be joined, split, or modified by introducing additional points, edges and faces. Indeed, substantial improvements in grid quality are expected in the future, benefiting both solver efficiency and accuracy of solutions. Also, tetrahedral meshes require special treatment in certain cases. This is not the case with polyhedral cell topology i.e. cell-wise local mesh refinement, sliding grid interfaces, periodic boundaries, etc., only create special types of polyhedral cells which are the same for a given solver. [55]

For this analysis, an overset mesh approach is undertaken. The overset mesh will also be used for dynamic flow simulations performed after the steady state analysis. In an overset grid system, a complex geometry is decomposed into a system of geometrically simple overlapping meshes. Boundary information is exchanged between these meshes via

interpolation of the flow variables, and many mesh points may not be used in the solution. Each block has boundary or fringe points, which lie in the interior of a neighboring block (or blocks) and will require information from that containing block. The data that must be generated to successfully complete an overset mesh calculation is not insignificant, and thus has been automated to a high degree. In very general terms, there are three steps to setting up an overset simulation namely, grid generation, hole cutting and determination of interpolation weights. Meshes for an overset simulation are generally simple and structured, and are often generated hyperbolic or marching techniques. The key element is in arbitrary overlap of the computational mesh that define and surround the geometry to be simulated. They may be structured, unstructured, Cartesian or a combination of these. One intuitive combination occurs when structured-curvilinear grids and Cartesian grids are used. A high quality body-fitting curvilinear grid is built independently for each geometric component and embedded within a coarser Cartesian grid. Because each curvilinear grid is paired with a component from the geometry, overset grids can be used to track relative motion with computational efficiency, but domain connectivity must be performed so that adjacent grids share information. [56]

In this case a polyhedral mesh approach is taken wherein an inner subdomain is created as the overset region and a high density mesh is created around the airfoil for accurate resolution of flow features. Figure 44 and Figure 45 present the mesh created for simulation of the NACA 63621 airfoil.

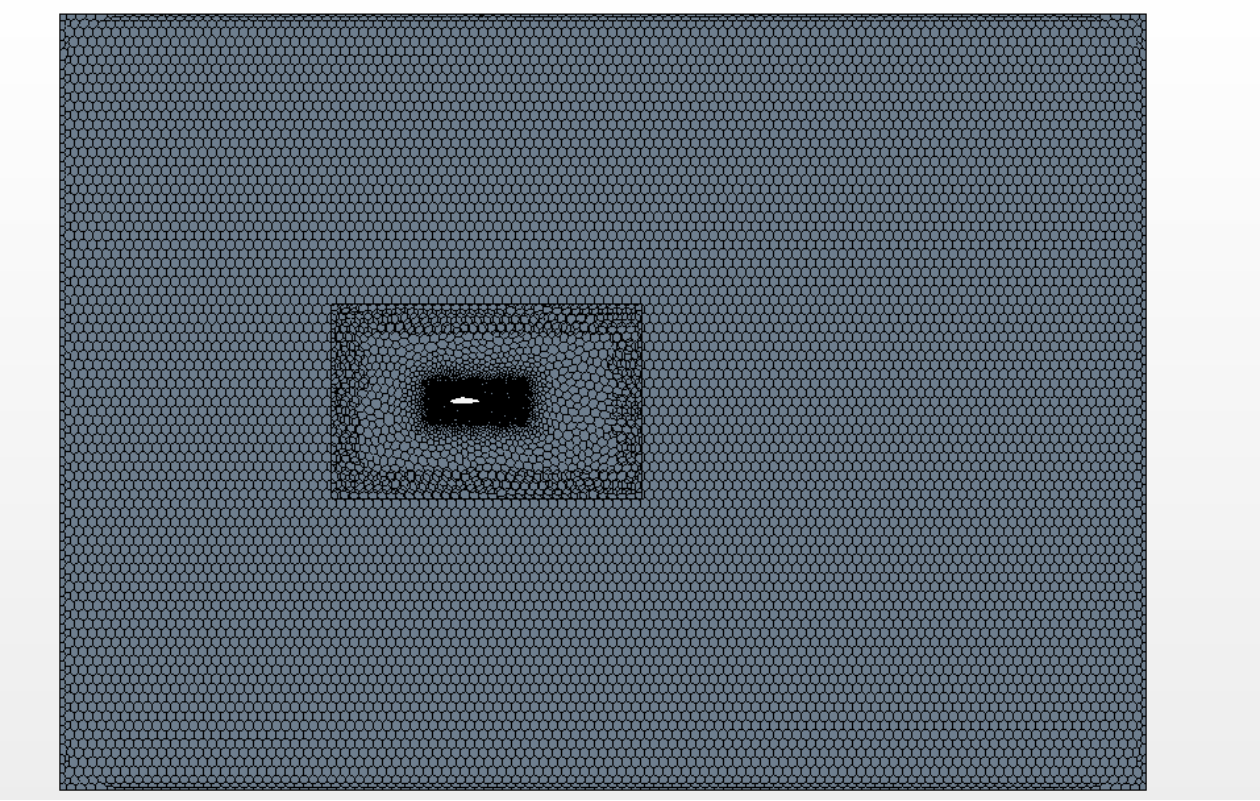

Figure 44. Representative mesh used for analysis

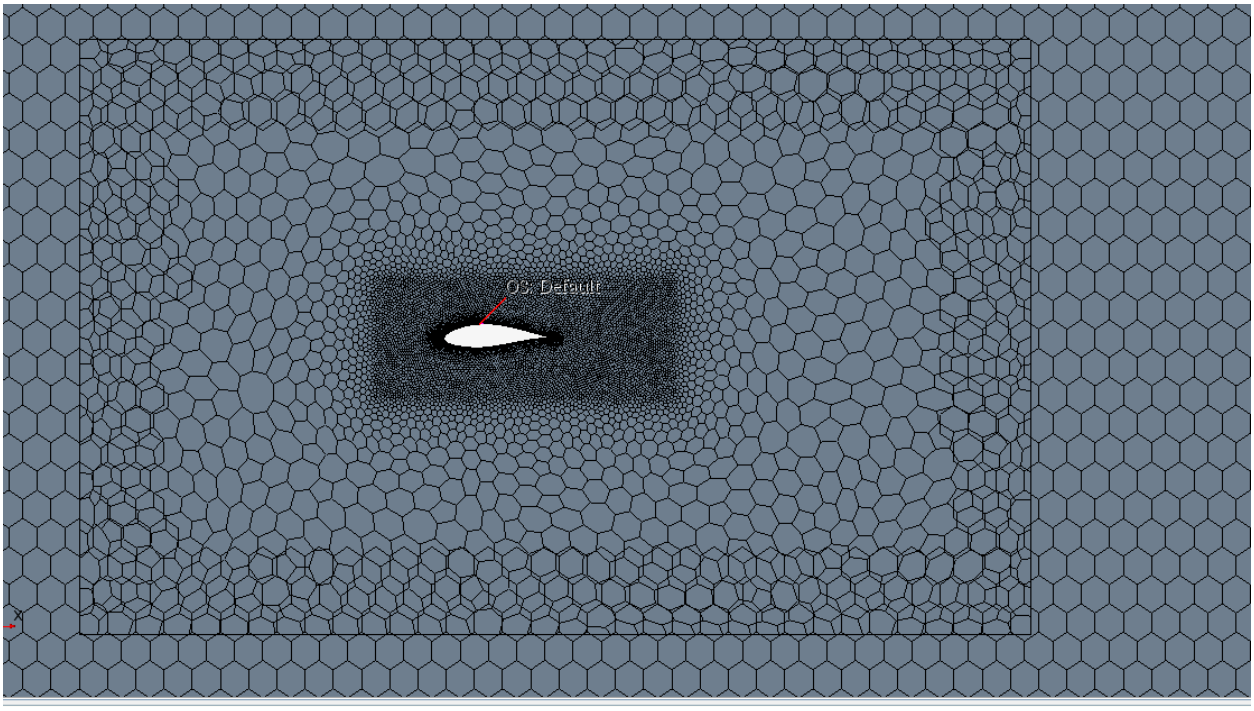

Figure 45. Representative mesh - inner domain – used for analysis

7.4.3 Results

Based on the analysis carried out, the maximum lift-to-drag ratio for each design configuration is calculated and plotted. Figure 46 shows the lift-to-drag ratio of the triangular vortex generator for the FB47 flatback airfoil. Figure 47 shows the lift-to-drag ratio for the vane type vortex generators for the FB47 airfoil.

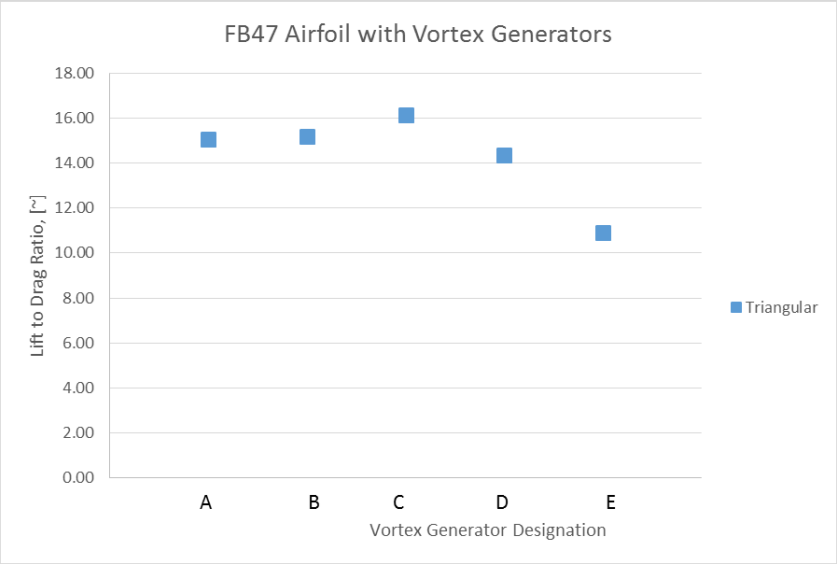

Figure 46. Lift-to-Drag Ratio of Triangular Vortex Generators for FB47 airfoil

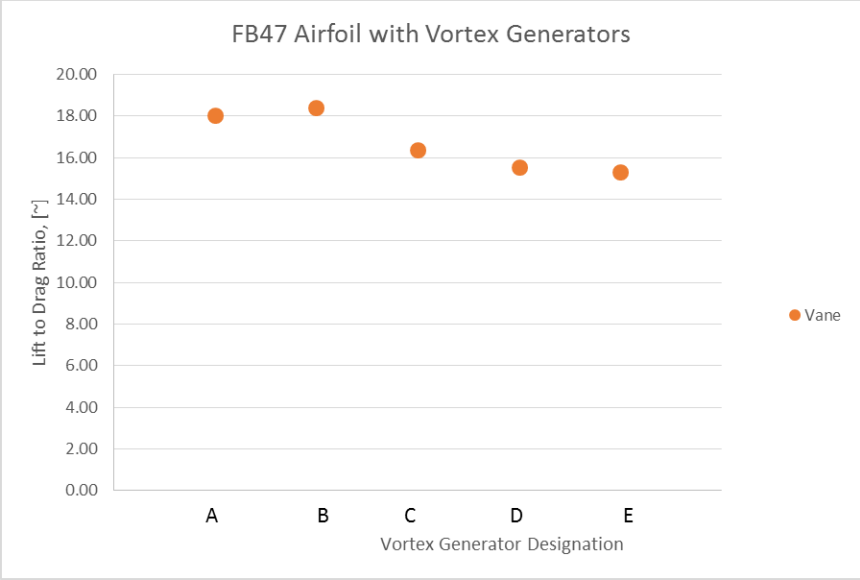

Figure 47. Lift-to-Drag Ratio of Vane Type Vortex Generators for FB47 airfoil

Based on the results obtained for the two configurations, it is decided to choose the vane type vortex generator for the FB47 airfoil since it offer superior performance as compared to the triangular vortex generator designs. Specifically, in this case the B-design achieves the highest performance and hence is chosen for system integration into the blade design. Since the performance of the vane type vortex generator configuration outperforms the triangular design configuration, it is decided to evaluate the different vane type vortex generator configurations for the NACA 63621 airfoil.

For the NACA 63621 airfoil, the C-design configuration offer the best performance and hence is selected as the optimal design from the chosen matrix. Figure 48 shows the lift-to-drag ratio for the various configurations. The airfoil analysis is carried out at a Reynolds number of 3 million based on chord.

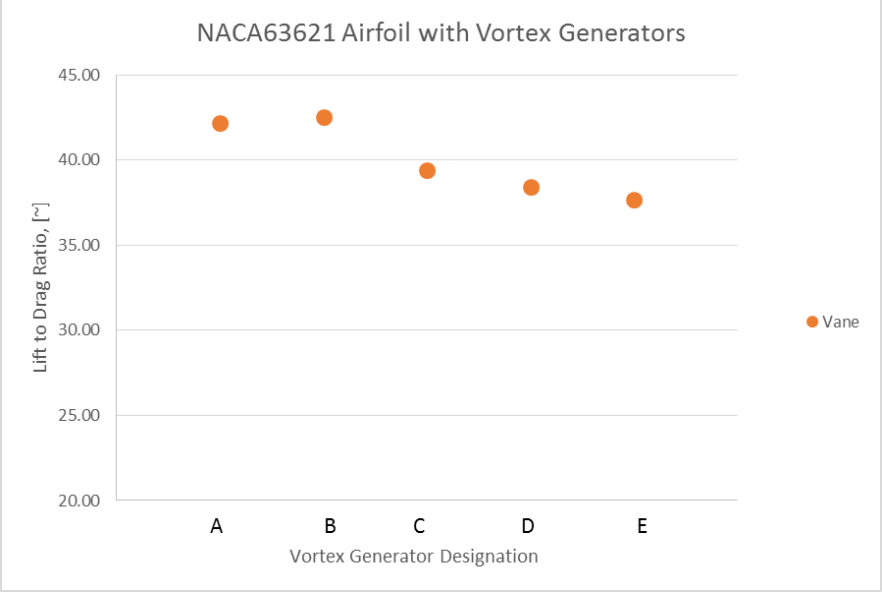

Figure 48. Lift-to-Drag Ratio of Vane Type Vortex Generators for NACA 63621 airfoil

7.4.4 Full Aerodynamic Data for FB47 and NACA 63621 airfoils

Based on the configurations chosen, an extended set of performance data is generated for the two airfoils. The same mesh and flow properties are used for the analysis. Figure 49 shows the lift characteristics of the FB47 airfoil whereas Figure 50 shows the drag characteristics of the FB47 airfoil with vortex generators. As compared to the pure airfoil data, we note an increase in lift at higher angles of attack. The vortex generator configuration of the FB47 airfoil achieves a maximum lift of 1.63 occurring at 14°. However, the increase in lift also comes with an increase in drag at these high angles of attack. It should be noted that in spite of the increase in drag the net lift-to-drag ratio of the vortex generator configuration exceeds that of the clean airfoil at high angles of attack. Similar to the FB47 airfoil, the performance characteristics for the NACA 63621 airfoil are developed and presented below. Figure 51 presents the lift characteristics with angle of attack for the NACA 63621 airfoil with vortex generators whereas Figure 52 presents the drag characteristics with angle of attack for the same airfoil. The peak lift coefficient for the NACA airfoil with vortex generators is 1.76 occurring at 16° angle of attack. This aerodynamic performance data is used for evaluating the remaining two configurations outlined earlier in this dissertation.

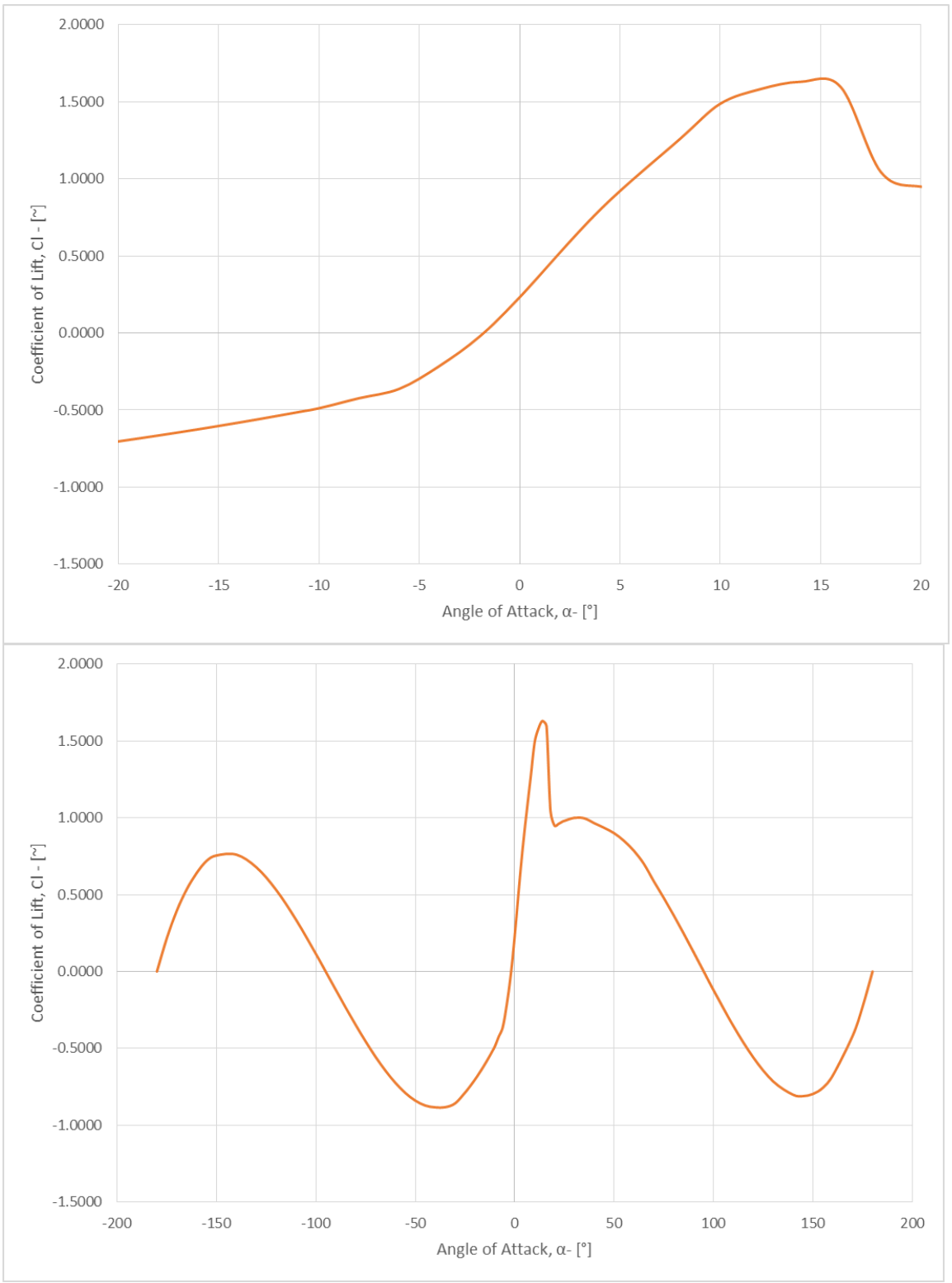

Figure 49: Lift Coefficient for FB47 airfoil with Vortex Generators

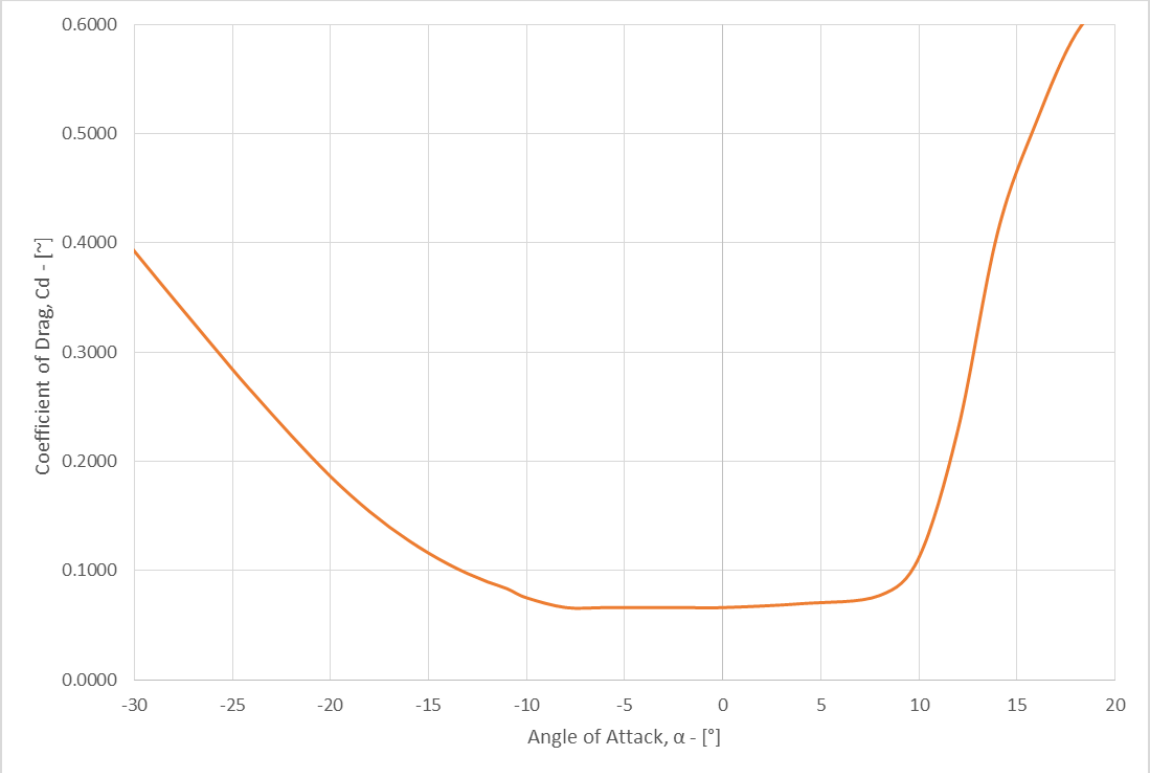

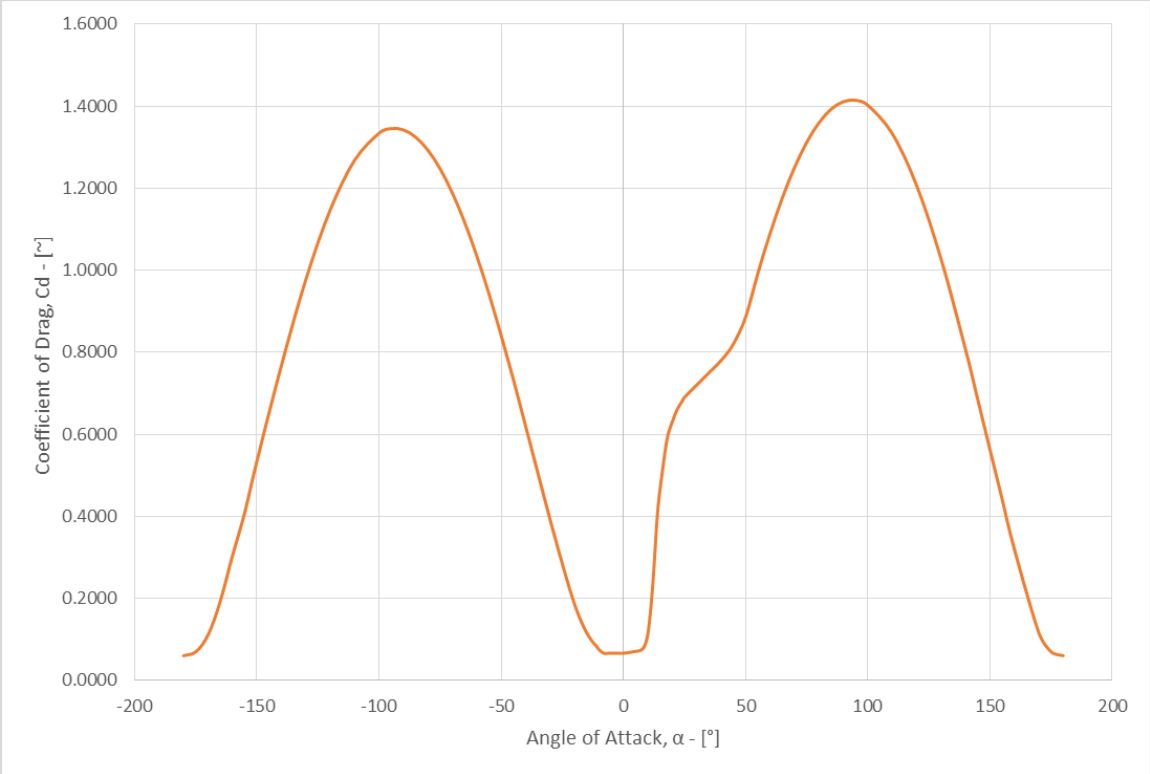

Figure 50: Drag Coefficient for FB47 airfoil with vortex generators

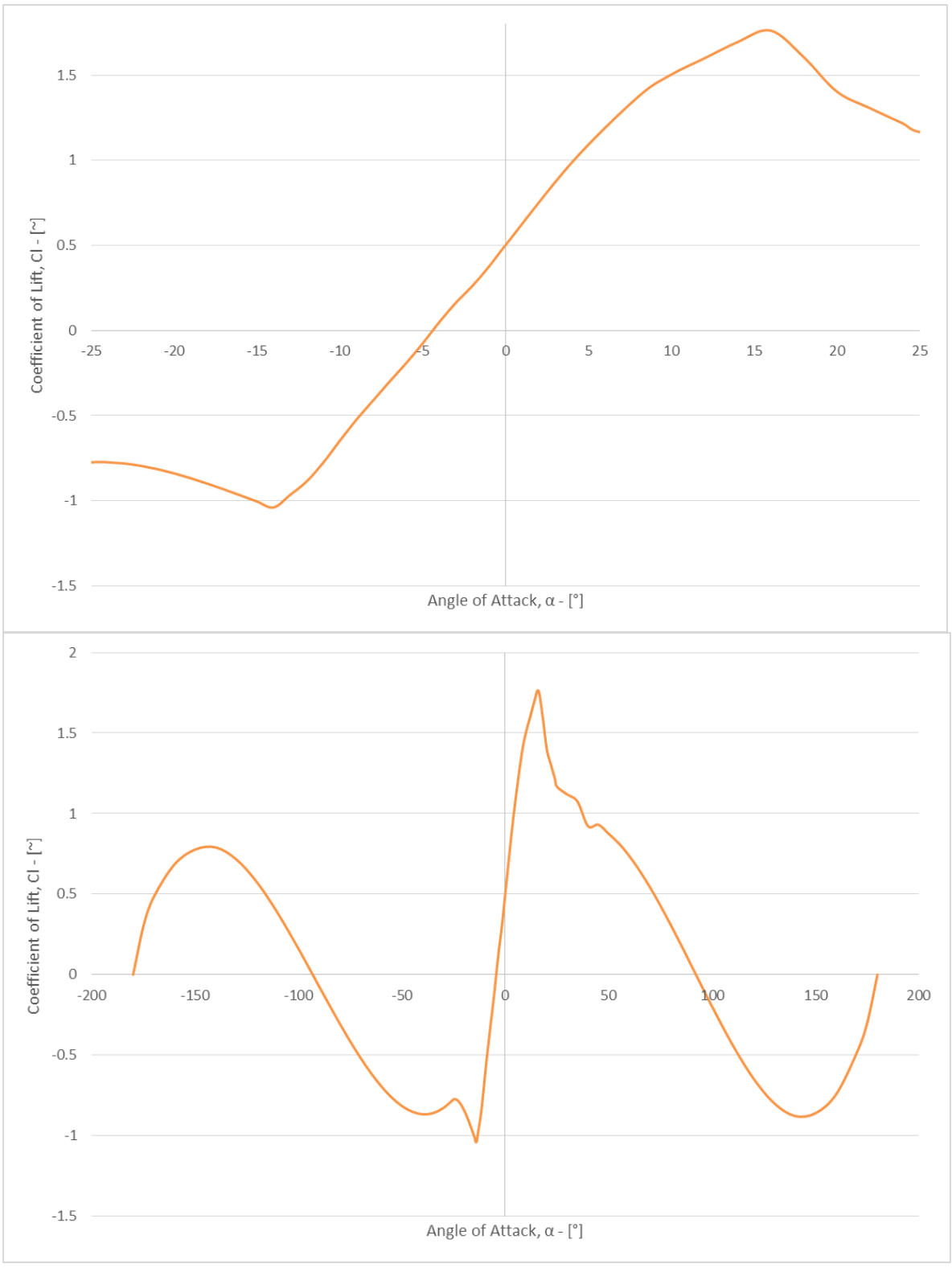

Figure 51. Lift Coefficient for NACA 63621 airfoil with vortex generators

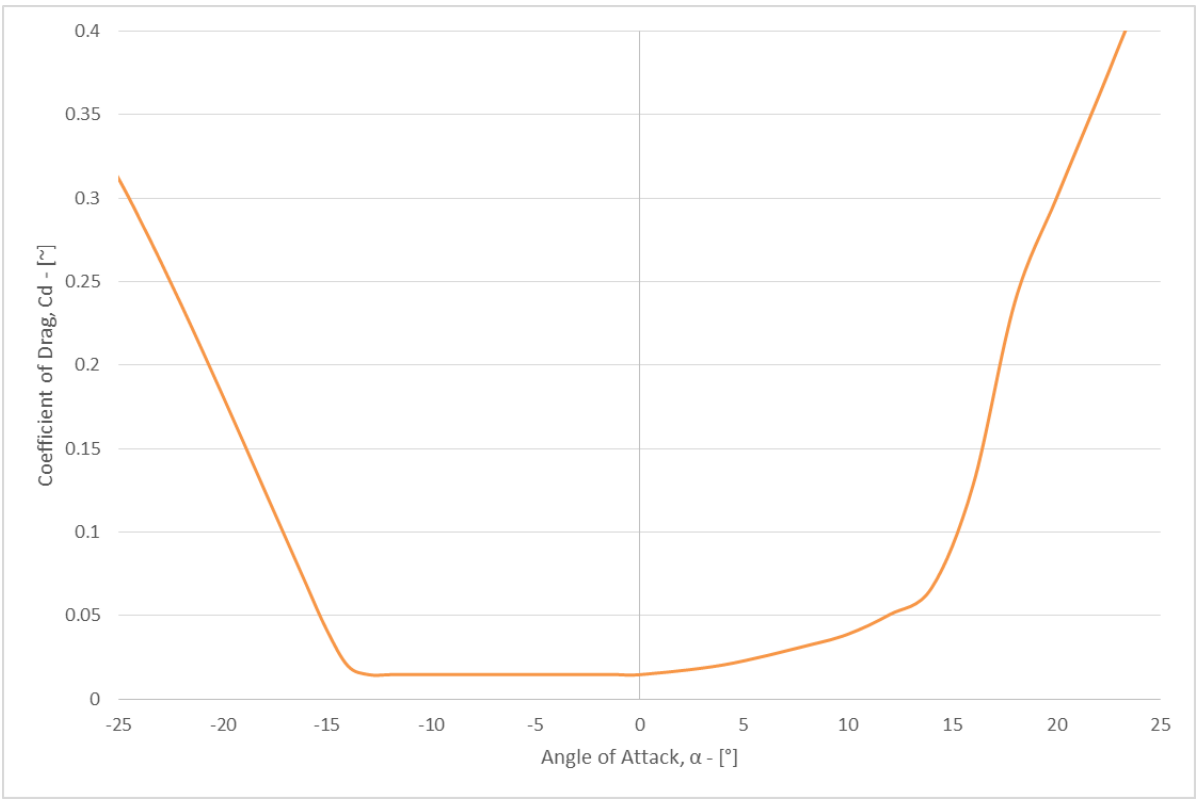

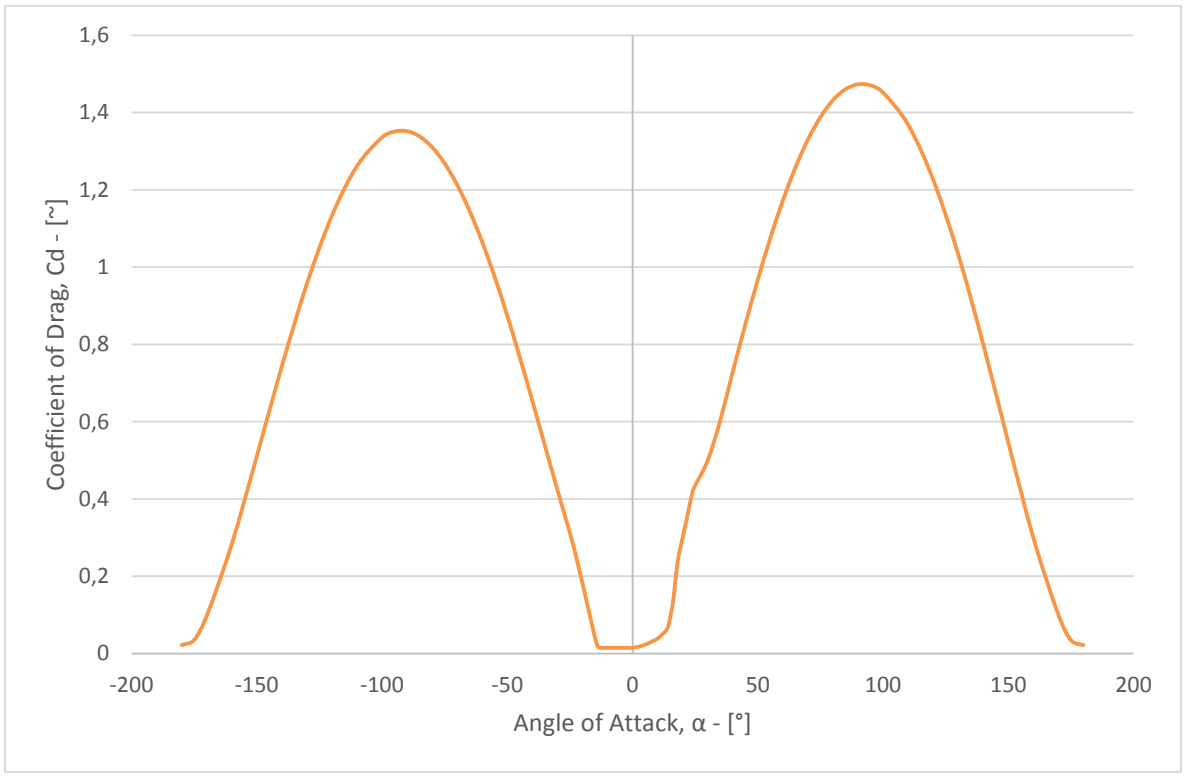

Figure 52. Drag Coefficient for NACA 63621 airfoil with vortex generators

7.5. Unsteady Airfoil Analysis

In order to study the impact of dynamic inflow conditions on the performance of airfoils, e.g., dynamic lift phenomenon, an unsteady airfoil analysis is performed. As a part of the unsteady analysis, three airfoils are analyzed namely LS(1)-MOD0417, FB47 and NACA 63621. The latter two airfoils are studied with vortex generators since this is the primary configuration that is currently being used in the blade design. For brevity, the performance data for the NACA63621 airfoil is not presented in this work since during the final design configuration with vortex generators, NACA 63621 airfoil with vortex generators is not used. The unsteady simulation is carried out using STAR CCM+ software. The overset meshes used for the steady analysis are used for the unsteady analysis as well. The mean angle of attack is set ~~to~~ at 8 degrees. For the LS(1)-MOD0417 airfoil the frequency of pitching about the quarter chord is set to 0.6 Hz. For the FB47 airfoil case, the frequency of oscillations is set to 2.0 Hz with a mean angle of 8 degrees. The lift and drag data are recorded and used to evaluate the vortex generator blade designs (both add-on and integral vortex generator configurations).

The lift data for LS(1)-MOD0417 airfoil and FB47 with VGs airfoils is presented in figures Figure 53 and Figure 54 respectively. As seen in the figures below, peak lift coefficient of ~2.4 is obtained for the FB47 airfoil when subjected to unsteady flow field conditions, thus revealing the phenomenon of dynamic lift. The hysteresis loop extends from ~7° to 16.5° for this airfoil pitching at 2 Hz.

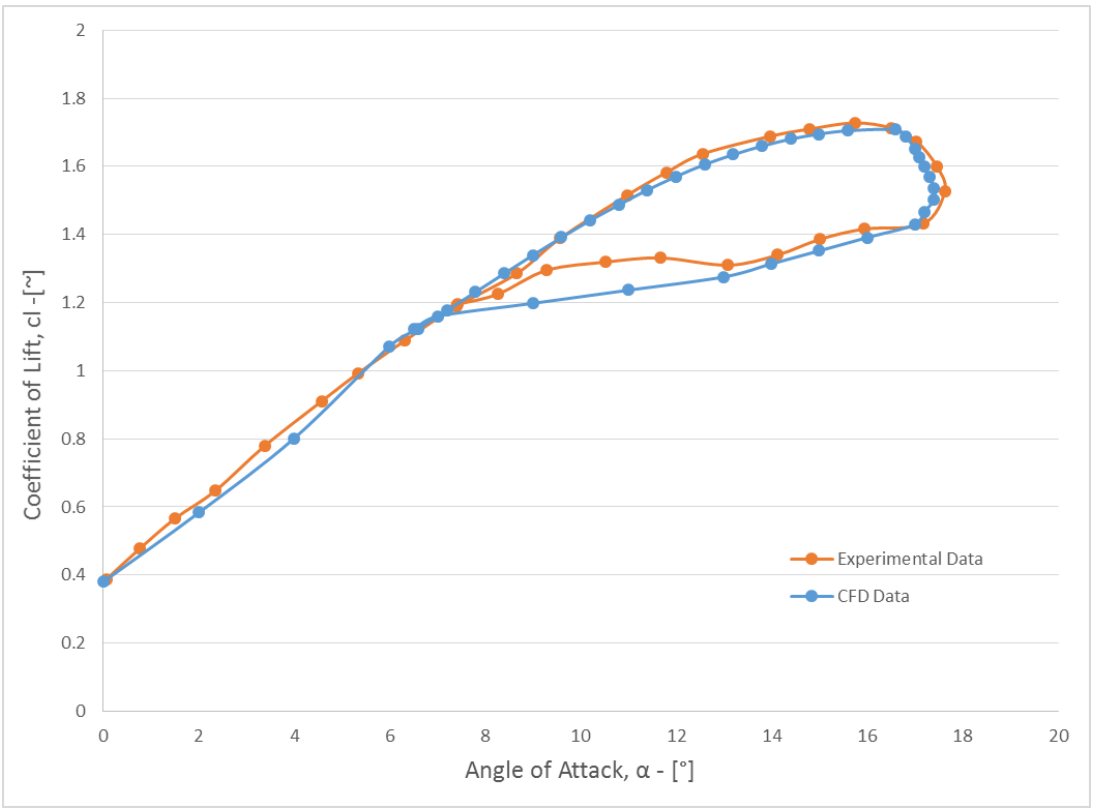

Figure 53: Unsteady lift coefficient for LS(1)MOD0417 airfoil

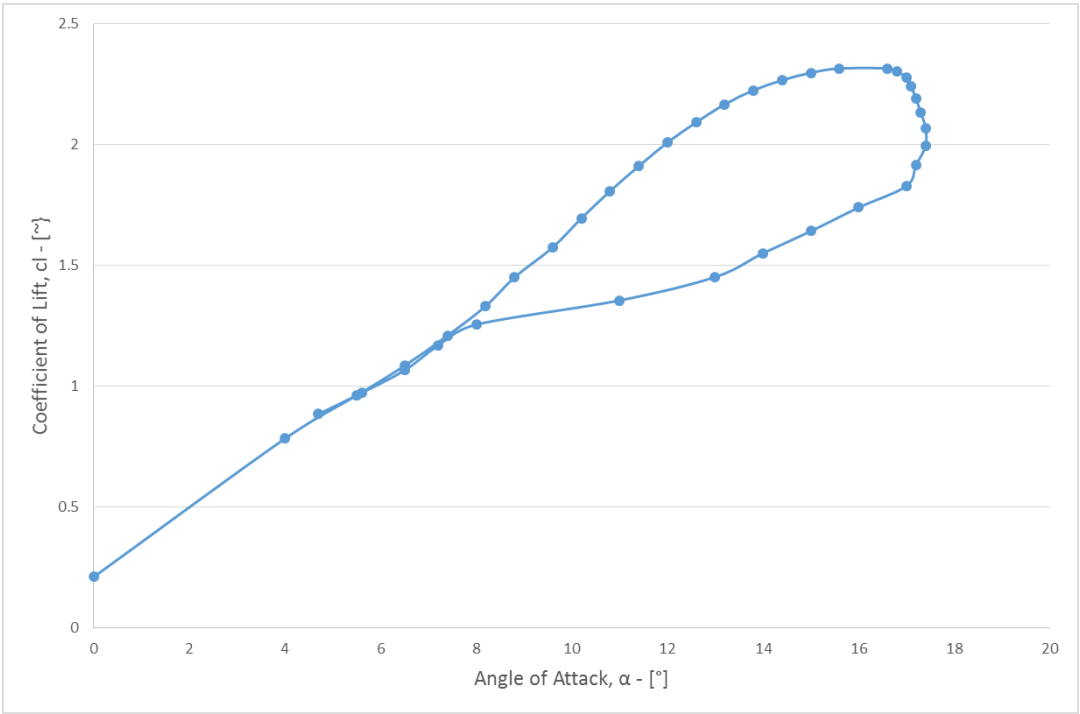

Figure 54: Unsteady lift coefficient for FB47 airfoil

8. Blade Design with Vortex Generators

8.1 56-m Blade with Add-on Vortex Generators

Using the airfoil data generated in the previous section using numerical tools, the performance of the 56m baseline blade design is evaluated. A BEM-based approach is used for analyzing the performance of the 56-m blade with add-on vortex generators. For this analysis the impact of vortex generators in the transition region as well as in the outboard region of the blade is recorded. Upon preliminary analysis it is observed that the use of vortex generators on the outboard region of the blade impact the performance negatively. The reason for this result is due to the dominance of the drag penalty seen by adding vortex generators in the outboard region. For an optimal blade design, the chord and twist combination are chosen so that the sections across the blade span operate at or near the maximum lift-to-drag ratio point of the given airfoil. By adding vortex generators, stall delay with increased lift-to-drag ratios at higher angles of attack is obtained but at lower angles of attack a penalty in drag is still observed. However by using vortex generators only in the inboard region of the blade, specifically from 15% to 30% blade span, we see an increase in performance of the blade. Table 20 provides the performance data for the 56-m blade with add-on vortex generators. Figure 55 presents the power curve for the 56-m blade with vortex generators. An annual energy capture of 9200 MWhr is obtained for this configuration.

An increase of ~0.4% is seen by the addition of vortex generators to the transition region of the blade. In order to evaluate loads and cost associated with this added design feature, RotorPerf code (a performance evaluation code based on the Optimization tool) is used. An increase in blade root bending moment of ~1.2% and increase in COE of 2.13% is

observed as compared to the baseline blade. The blade root bending moment for the add-on blade configuration is 8135kNm. The cost of energy for this configuration is calculated as 38.37$/MWhr. The cost of energy calculation accounts for the manufacturing cost for the vortex generator, labor and equipment for installation of these devices in the field and the maintenance cost across the lifespan of the blade. As seen, there is an increase in the overall extreme loads experienced by the blade. This increase in loads will also affect the fatigue loads, which in turn will reduce the total operational life of the turbine. Hence the use of vortex generators as a retrofit solution for improved performance does not entirely serve as a solution in this case based on the overall lifecycle cost. It should be noted that the increase in energy capture is not proportional with the increase in cost of energy.

Table 20. Power performance for a 56m blade using vortex generators

Wind Speed V (m/s)	Shaft Speed Ω (rpm)	Tip Speed Ratio X (~)	Pitch Angle β (°)	Aero Power Coefficient Cpaero (~)	Aero Power Paero (MW)	Electric Power Pelec (MW)
3.50	6.50	11.18	0.00	0.480	0.13	0.12
4.00	6.98	10.50	0.00	0.484	0.20	0.18
4.50	7.85	10.50	0.00	0.484	0.28	0.25
5.00	8.72	10.50	0.00	0.484	0.38	0.35
5.50	9.59	10.50	0.00	0.484	0.51	0.46
6.00	10.46	10.50	0.00	0.484	0.66	0.60
6.50	11.33	10.50	0.00	0.484	0.85	0.76
7.00	12.21	10.50	0.00	0.484	1.06	0.95
7.50	12.50	10.04	0.00	0.480	1.29	1.16
8.00	12.50	9.41	0.00	0.466	1.52	1.37
8.50	12.50	8.85	0.00	0.446	1.74	1.57
9.00	12.50	8.36	0.00	0.422	1.96	1.76
9.50	12.50	7.92	0.00	0.396	2.16	1.94
10.00	12.50	7.53	0.00	0.371	2.36	2.00
15.00	12.50	5.02	14.67	0.104	2.36	2.00
20.00	12.50	3.76	21.86	0.044	2.36	2.00
25.00	12.50	3.01	27.80	0.022	2.36	2.00

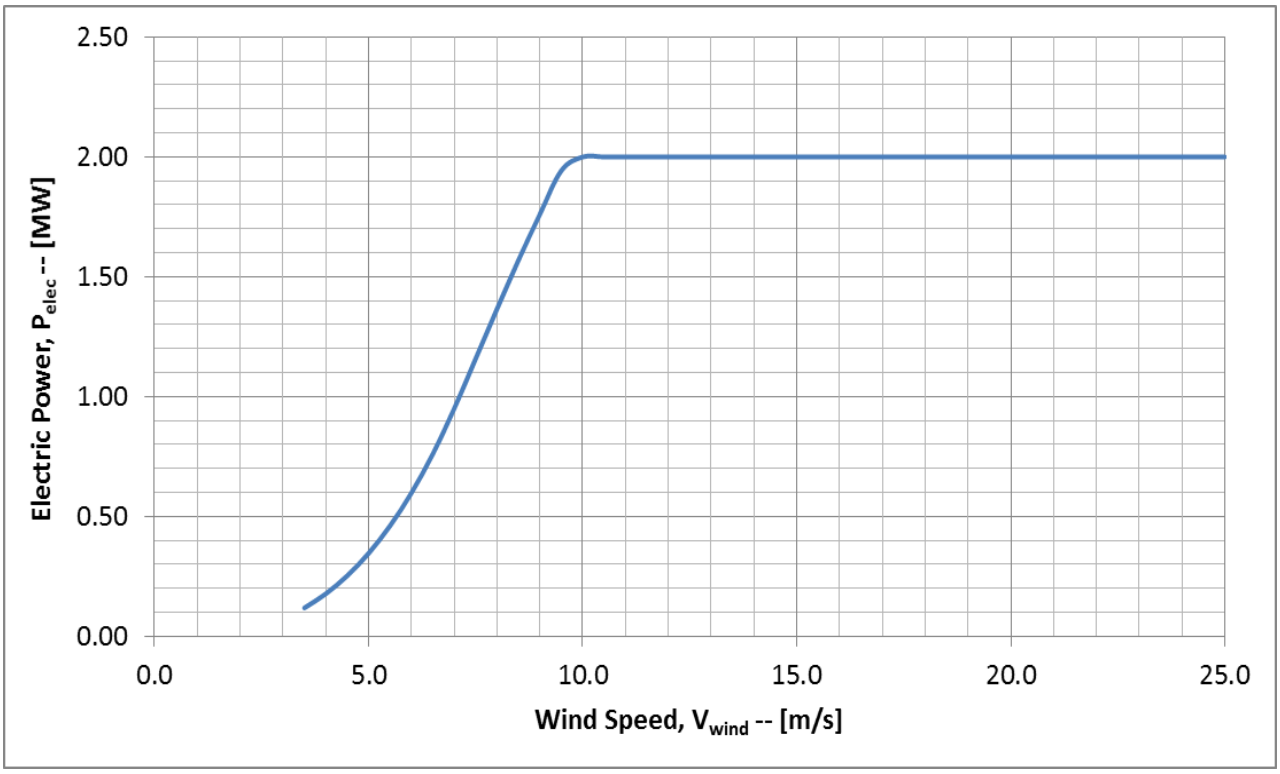

Figure 55. Power Curve for 56m blade design with add-on vortex generators

8.2 Blade Optimization with Integral Vortex Generators

In order to determine the impact of integral vortex generators (IVG) on the design features and selection of a blade, an optimization analysis is carried out. Since the analysis is primarily concerned with the aerodynamic performance, the detailed structural design is not carried out as a part of this work. Preliminary loads and structural design data is obtained from the optimization analysis providing enough details about the mass and loads for the integral vortex generator blade design. For the optimization analysis, BladeOpt is used whereas the aerodynamic design is carried out using BEM based rotorspreadsheet tool. The rotorspreadsheet tool used a BEM based sectional approach for determining the performance of a rotor blade from cut-in to cutout. The blade root bending moment, blade mass, blade root bending moment and cost of energy are calculated as a part of the optimization analysis.

8.2.1 Optimization Analysis of 56m blade using Integral Vortex Generators

Below are the optimization parameters used for the optimization analysis. Two different configurations are analyzed as a part of this optimization study. Both configurations incorporated vortex generators but at different locations. The two configurations are named:

1. Single Vortex Generator Configuration
2. Double Vortex Generator Configuration

The first configuration consisted of vortex generators only in the transition region of the blade whereas the second configuration incorporated vortex generators at both the inboard and outboard locations of the blade. FB-DU-NACA airfoils are used for this optimization analysis. The following steps are performed as a part of the optimization analysis.

- The design requirements are established, as described in Table 21.

- The optimization is carried out for:
  - Rotor Blade Length: 56m
  - Wind Class: III-A (as per GL 2010)
  - Rated Power: 2.0 MW
  - Shaft Speed: 12.5 rpm
  - Spar Cap Material: H-Glass
- Table 21 - Table 24 summarizes the inputs used for the optimization analysis carried out for the 2.0MW turbine.
- DU-NACA airfoil family is considered as a primary airfoil family for this optimization. (See Table 23 and Table 24)

Table 21. Summary of Design Requirements for the 2.0-MW Wind Turbine Rotor

Design Wind Class	III-A (GL 2010)
Blade Mass	≤ 12.5tons
Blade Cost	(Minimize)
Extreme Root Bending Moment Load Margin, M_{XY}	≤ 10,000 kNm
Rated Power	2.0 MW
Blade Length	56m
Hub Height	80 m
Rated Shaft Speed	12.5rpm
Blade Primary Material	H-Glass

Table 22. Nominal Airfoil Thickness and Airfoil Designation

Airfoil Designation	Airfoil Thickness-to-Chord Ratio
WEI-FB47VG	47.29%
DU-W-405LM	40.50%
DU99-350	35.09%
DU97-W-300LM	30.00%
DU91-W2-250LM	25.00%
NACA63621VG	21.00%

Table 23. List of Design Variables for the 2.0-MW Rotor Blade Optimization Study

Design Input Variable	Choice of Selection	Comments
Airfoil Family	WEI-FB, DU and NACA family	WEI-FB, DU and NACA airfoil family consisted of FB-47VG, DU 40, DU35, DU30, DU25, NACA 63621VG airfoils.
Thickness distributions	No. of thickness distributions = 8	8 distributions are defined to cover the entire design space. This selection is defined to accommodate both high aerodynamic performance blades as well as structurally efficient blade designs.
Chord Distributions	Max chord variation: From 2.0 to 3.5 m	A spanwise distribution based on the maximum chord variation was defined to obtain different blade planforms. The matrix of chord combinations and thickness distributions equated to approximately 1.7million blade designs in the rotor optimization

Materials	H-Glass	-

Table 24. Summary Table of Airfoil Thickness Distribution for the Optimization Study

r/R	AF-1	AF-2	AF-3	AF-4	AF-5	AF-6	AF-7	AF-8
r_{hub}/R	100.00%	100.00%	100.00%	100.00%	100.00%	100.00%	100.00%	100.00%
25.00%	58.00%	58.00%	47.00%	47.00%	47.00%	47.00%	47.00%	47.00%
30.00%	52.00%	47.50%	40.00%	44.00%	38.50%	42.50%	40.00%	40.00%
40.00%	46.00%	40.00%	35.00%	38.50%	32.00%	37.00%	35.00%	35.00%
50.00%	40.00%	35.00%	30.00%	34.00%	27.50%	32.50%	30.00%	30.00%
60.00%	35.00%	30.00%	25.00%	28.50%	25.00%	27.50%	25.00%	25.00%
70.00%	30.00%	25.00%	22.50%	25.00%	23.00%	24.00%	21.00%	21.00%
80.00%	25.00%	22.50%	21.00%	22.50%	21.00%	21.00%	21.00%	21.00%
94.00%	22.50%	21.00%	21.00%	21.00%	21.00%	21.00%	21.00%	21.00%
100.00%	21.00%	21.00%	21.00%	21.00%	21.00%	21.00%	21.00%	21.00%

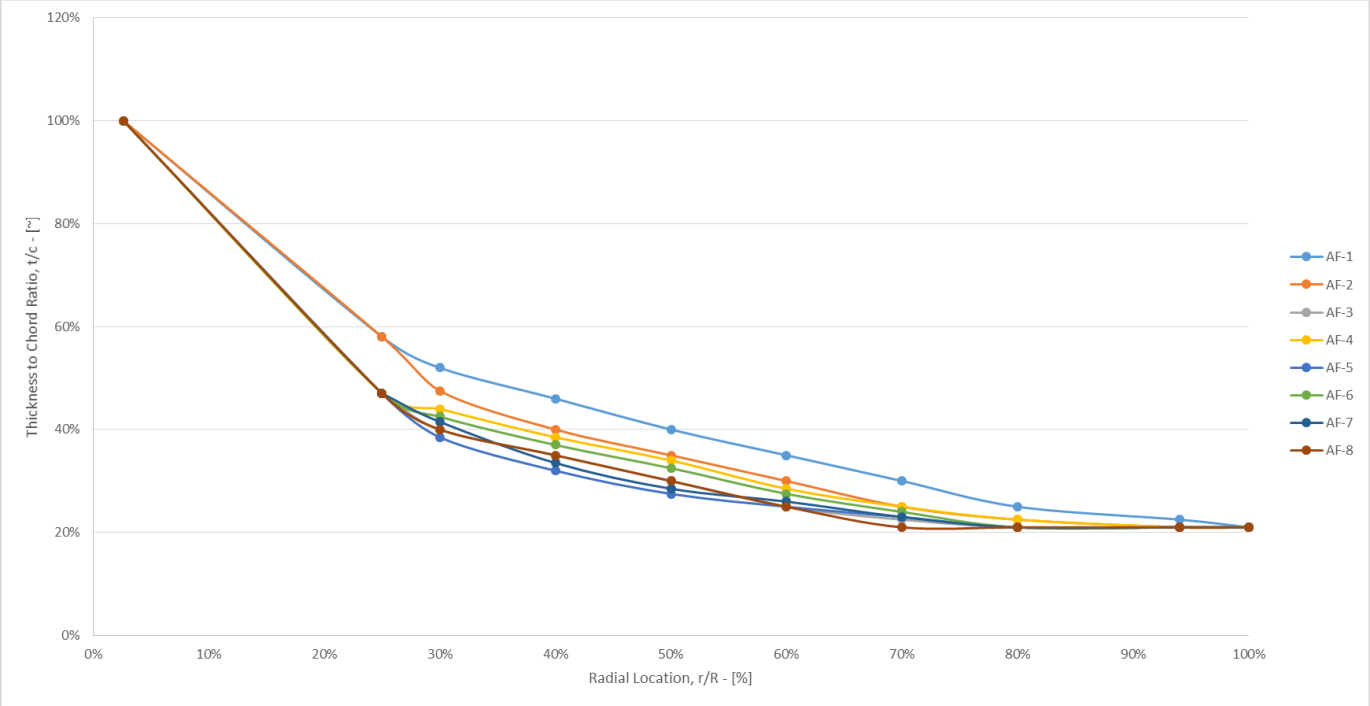

Figure 56. Thickness-to-Chord Ratio Plot of Airfoil Thickness Families for Optimization

8.3. Optimization Analysis Results

This section gives details about post processing the results obtained from the BladeOpt. After imposing the weighting criteria provided in the next section, the design space is further narrowed down and the optimal blade is selected from the down selected blades. Section 8.4 and 8.5 discusses overall post processing approach whereas Figures 8.6 and 8.7 show details on specifics used in post processing different designs for a blade variable speed 2.0-MW turbine.

8.4. Design Constraints

Out of 1,679,184 blades obtained from the BladeOpt, only the blades that would satisfy the design constraints, pertaining to each configuration i.e. single vortex generator configuration and double vortex generator configuration, would be considered for further examination. All design constraints established earlier are applied. The cost functions are calculated for each of these blades and the top 3 blades with the lowest cost functions are selected for a final optimal blade selection.

8.5. Cost Functions

The cost function of each blade is a function of various blade parameters, their ranges, the relative distance of the value of the parameters from the corresponding parameters of the blade with the lowest COE in the design space, and the weight assigned to the parameters. The parameters considered are the M_{XY}, AEP, Blade Mass, Blade Cost, and COE. Other parameters can be added if required. If any of the parameters are not to be included, then their weight is assigned equal to zero.

The normalized weights are assigned to each of the parameters based on their relative importance. This quantification of relative importance, or weights, depends on several

factors such as the market, blade manufacturer, customer, application, etc. Since there are multiple possibilities, several possibilities are considered and thus different sets of weights are used.

Depending on the weights assigned to each of the parameters, there are different sets of cost functions. All these different sets of cost functions are calculated for each blade. Then the blade with the lowest cost function for each different set of cost function is identified. Out of these, one of them is selected as the optimal blade. In this research, blades that have the lowest cost function are presented, and only a recommendation is made for the final blade to be selected as the optimal blade.

8.6. Weights for Properties used for 2.0-MW Wind Turbine

The weights used for the parameters examined for the current blade, i.e. the 2.0-MW wind turbine are given in Table 25. A total of eight different sets were examined.

Table 25. Weight for each property and different sets of weights for the design space

Sl. No.	Property	Set 1	Set 2	Set 3	Set 4	Set 5	Set 6	Set 7	Set 8
1	M_{XY}	0.00%	35.00 %	35.00 %	25.00 %	50.00 %	35.00 %	20.00 %	30.00 %
2	AEP	35.00 %	0.00%	0.00%	0.00%	0.00%	35.00 %	20.00 %	20.00 %
3	Blade Mass	45.00 %	65.00 %	35.00 %	25.00 %	25.00 %	15.00 %	20.00 %	25.00 %
4	Blade Cost	20.00 %	0.00%	30.00 %	25.00 %	0.00%	0.00%	20.00 %	0.00%
5	COE	0.00%	0.00%	0.00%	25.00 %	25.00 %	15.00 %	20.00 %	25.00 %

8.7. Single Vortex Generator Configuration - Blades with the Lowest Cost Function

The blades with the lowest cost function under each set and its properties are given in Table 26. Table 26 shows the three blades within the design space that has the lowest cost function depending on the weight sets given in Table 25. A final recommendation of AFC3-52664 blade design is made due to high performance, low blade weight and low blade root bending moment, M_{xy} values. It should be noted that we would expect a +/- 5% margin on the blade root bending moment.

Table 26. Blades with the Lowest Cost Function for Single IVG Configuration

Set No.	Blade Name	Maximum Root Bending Moment, MXY (kNm)	Annual Energy Production, AEP (MWh/yr)	Coefficient of Power, Cp	Blade Mass (tons)	Cost of Energy, COE (US$/MWh)
1	AF5-52664	9998.26	9247	0.4800	11.963	36.87
2	AF3-52664	9954.13	9232	0.4785	11.662	36.88
3	AF3-52583	10080.42	9238	0.4812	11.671	36.88

8.8. Double Vortex Generator Configuration - Blades with the Lowest Cost Function

The blades with the lowest cost function under each set and its properties are given in Table 27. Table 27shows the three blades within the design space that has the lowest cost function depending on the weight sets given in Table 25. No feasible designs resulted from this configuration based on the higher cost of energy and lower annual energy capture values as compared to the single vortex generator design configurations.

Table 27. Blades with the Lowest Cost Function for Double IVG Configuration

Set No.	Blade Name	Maximum Root Bending Moment, MXY (kNm)	Annual Energy Production, AEP (MWh/yr)	Coefficient of Power, Cp	Blade Mass (tons)	Cost of Energy, COE (US$/MWh)
1	AF4-26339	8771.37	8665	0.4319	11.92	40.9
2	AF4-17591	8339.54	8523.18	0.4267	12.955	41.52
3	AF4-52583	10190.45	8953.77	0.4437	11.056	39.94

Hence based on the results obtained, single vortex generator configuration provides the best results from an annual energy capture and cost of energy standpoint.

8.9. Aerodynamic Design – 56m blade with Integral Vortex Generators (IVG)

In order to perform the aerodynamic design of the 56m blade with vortex generators, the geometry obtained from the optimization results is post processed to ensure that no discontinuities exist in the geometry of the blade. Thereafter, the optimal tip speed ratio is determined and the performance is calculated using BEM techniques as used the previous cases. The aerodynamic performance, based on steady inflow conditions, of the 56m blade with integral vortex generators is given in Table 28. Maximum Aerodynamic Power Coefficient, C_{pmax} = 0.481 is achieved whereas an Annual Energy Production based on IEC Class III Rayleigh distribution, AEP = 9,320 MWhr. Figure 61 shows the tip speed ratio and shaft speed schedule for the 56m blade. Figure 62 shows the coefficient of performance distribution vs wind speed for this configuration. Figure 63 shows the electric and aerodynamic power curves for the designed configuration. The aerodynamic performance of this blade configuration exceeds the baseline blade configuration by 1.7%, which is a significant and measurable increase in performance in the wind industry.

Table 28. Summary of the Aerodynamic Design of the 56-m blade with Integral Vortex Generators

Radial Station		Spanwise Station	Chord	Solidity	Twist	Sectional thicknes	Thickness-to-Chord Ratio	Airfoil
r	r/R	$s = r - r_{hub}$	c	σ	θ	t	t/c	**Used for Aerodynamic Modelling Purposes
(m)		(m)	(m)		(°)	(m)		
1.500	2.6%	0.000	2.215	0.705	0.00	2.215	100.0%	Cylinder
1.850	3.2%	0.350	2.215	0.572	0.00	2.215	100.0%	Cylinder
2.532	4.4%	1.032	2.215	0.418	0.00	2.215	100.0%	Cylinder
3.565	6.2%	2.065	2.215	0.297	0.00	2.215	100.0%	Cylinder
4.600	8.0%	3.100	2.250	0.234	0.00	2.205	98.0%	Cylinder
5.750	10.0%	4.250	2.300	0.191	14.00	2.185	95.0%	Cylinder
8.625	15.0%	7.125	2.650	0.147	14.00	2.120	80.0%	Cylinder - FB64 Interpolated Airfoil
11.500	20.0%	10.000	3.100	0.129	12.00	1.922	62.0%	FB64 - FB47VG Interpolated Airfoil
14.375	25.0%	12.875	3.300	0.110	10.00	1.551	47.0%	FB47VG Airfoil
17.250	30.0%	15.750	3.085	0.085	8.00	1.234	40.0%	DU40-W-405LM
20.125	35.0%	18.625	2.778	0.066	6.25	1.028	37.0%	DU40-W-405LM - DU-99-350 Interpolated Airfoil
23.000	40.0%	21.500	2.520	0.052	4.57	0.882	35.0%	DU-99-350
25.875	45.0%	24.375	2.344	0.043	3.63	0.766	32.7%	DU-99-350 - DU97-W-300LM Interpolated Airfoil
28.750	50.0%	27.250	2.180	0.036	3.25	0.654	30.0%	DU97-W-300LM
31.625	55.0%	30.125	2.013	0.030	2.88	0.557	27.7%	DU97-W-300LM - DU97-W2-250LM Interpolated Airfoil
34.500	60.0%	33.000	1.875	0.026	2.44	0.469	25.0%	DU97-W2-250LM
37.375	65.0%	35.875	1.758	0.022	1.88	0.419	23.8%	DU97-W2-250LM - NACA63621 Interpolated Airfoil
40.250	70.0%	38.750	1.641	0.019	1.25	0.369	22.5%	DU97-W2-250LM - NACA63621 Interpolated Airfoil
43.125	75.0%	41.625	1.523	0.017	0.63	0.332	21.8%	DU97-W2-250LM - NACA63621 Interpolated Airfoil
46.000	80.0%	44.500	1.406	0.015	0.16	0.295	21.0%	NACA63621
48.875	85.0%	47.375	1.280	0.013	0.00	0.269	21.0%	NACA63621
51.750	90.0%	50.250	1.150	0.011	0.00	0.242	21.0%	NACA63621
52.900	92.0%	51.400	1.080	0.010	0.00	0.227	21.0%	NACA63621
54.050	94.0%	52.550	1.000	0.009	0.00	0.210	21.0%	NACA63621
55.200	96.0%	53.700	0.880	0.008	0.00	0.185	21.0%	NACA63621
56.350	98.0%	54.850	0.689	0.006	0.00	0.145	21.0%	NACA63621
56.925	99.0%	55.425	0.541	0.005	0.00	0.114	21.0%	NACA63621
57.500	100.0%	56.000	0.058	0.000	0.75	0.012	21.0%	NACA63621

Table 29. Performance for Prated=2.0 MW, assume Drivetrain Efficiency of (Peak 90%)

ROTOR PERFORMANCE OUTPUT PARAMETERS						
Wind Speed V (m/s)	Shaft Speed Ω (rpm)	Tip Speed Ratio X (~)	Pitch Angle β (°)	Aero Power Coefficient C_{paero} (~)	Aero Power P_{aero} (MW)	Electric Power P_{elec} (MW)
3.50	6.50	11.18	0.00	0.451	0.12	0.11
4.00	6.50	9.78	0.00	0.481	0.20	0.18
4.50	7.31	9.78	0.00	0.481	0.28	0.25
5.00	8.12	9.78	0.00	0.481	0.38	0.34
5.50	8.93	9.78	0.00	0.481	0.51	0.46
6.00	9.75	9.78	0.00	0.481	0.66	0.59
6.50	10.56	9.78	0.00	0.481	0.84	0.76
7.00	11.37	9.78	0.00	0.481	1.05	0.94
7.50	12.18	9.78	0.00	0.481	1.29	1.16
8.00	12.50	9.41	0.00	0.478	1.56	1.40
8.50	12.50	8.85	0.00	0.471	1.84	1.66
9.00	12.50	8.36	0.00	0.457	2.12	1.91
9.50	12.50	7.92	2.45	0.408	2.22	2.00
10.00	12.50	7.53	4.40	0.350	2.23	2.00
10.50	12.50	7.17	5.90	0.3011	2.22	2.00
11.00	12.50	6.84	7.10	0.2628	2.23	2.00
11.50	12.50	6.54	8.25	0.2291	2.22	2.00
12.00	12.50	6.27	9.25	0.2024	2.22	2.00
12.50	12.50	6.02	10.23	0.1787	2.22	2.00
13.00	12.50	5.79	11.13	0.1592	2.22	2.00
13.50	12.50	5.58	12.00	0.1420	2.22	2.00
14.00	12.50	5.38	12.85	0.1271	2.22	2.00
14.50	12.50	5.19	13.65	0.1146	2.22	2.00
15.00	12.50	5.02	14.45	0.1033	2.22	2.00
15.50	12.50	4.86	15.20	0.0938	2.22	2.00
16.00	12.50	4.70	15.95	0.0851	2.22	2.00
16.50	12.50	4.56	16.65	0.0779	2.23	2.00
17.00	12.50	4.43	17.35	0.0713	2.23	2.00
17.50	12.50	4.30	18.05	0.0652	2.22	2.00
18.00	12.50	4.18	18.73	0.0598	2.22	2.00
18.50	12.50	4.07	19.38	0.0552	2.22	2.00
19.00	12.50	3.96	20.03	0.0509	2.22	2.00
19.50	12.50	3.86	20.68	0.0469	2.21	1.99
20.00	12.50	3.76	21.28	0.0438	2.23	2.00
20.50	12.50	3.67	21.90	0.0405	2.22	2.00
21.00	12.50	3.58	22.50	0.0377	2.22	2.00
21.50	12.50	3.50	23.10	0.0351	2.22	2.00
22.00	12.50	3.42	23.68	0.0329	2.23	2.00
22.50	12.50	3.35	24.25	0.0307	2.23	2.00
23.00	12.50	3.27	24.83	0.0287	2.22	2.00
23.50	12.50	3.20	25.40	0.0268	2.21	1.99
24.00	12.50	3.14	25.95	0.0252	2.22	1.99
24.50	12.50	3.07	26.50	0.0237	2.21	1.99
25.00	12.50	3.01	27.03	0.0224	2.23	2.00

***Note: Blade aerodynamic performance analysis results assume clean performance of airfoil sections and steady power.**

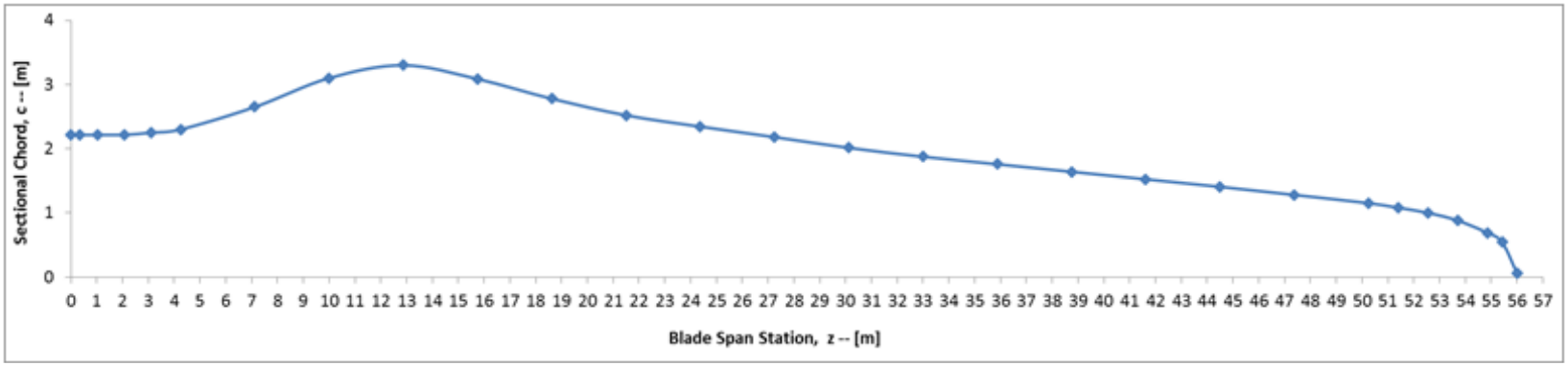

Figure 59. Chord Distribution for 56-m blade with Integral Vortex Generators

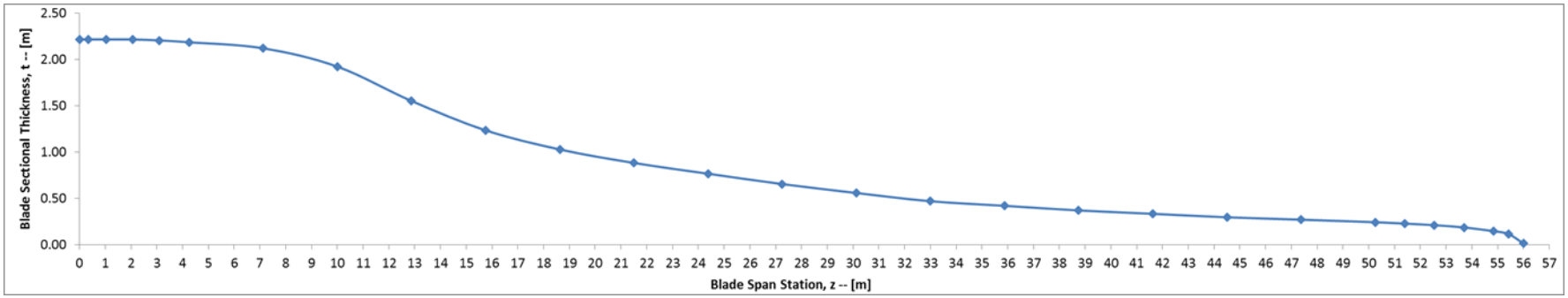

Figure 58. Thickness Distribution for 56-m blade with Integral Vortex Generators

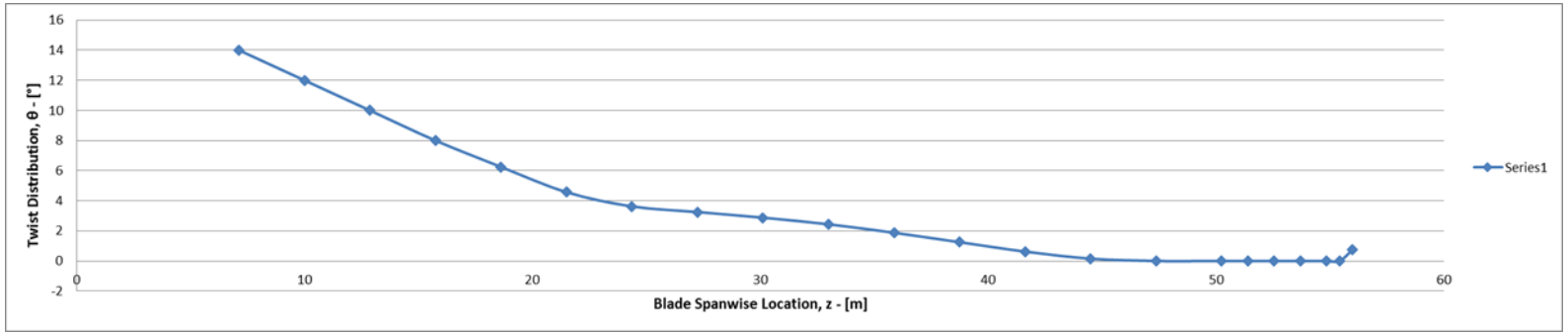

Figure 57. Twist Distribution for 56-m blade with Integral Vortex Generators

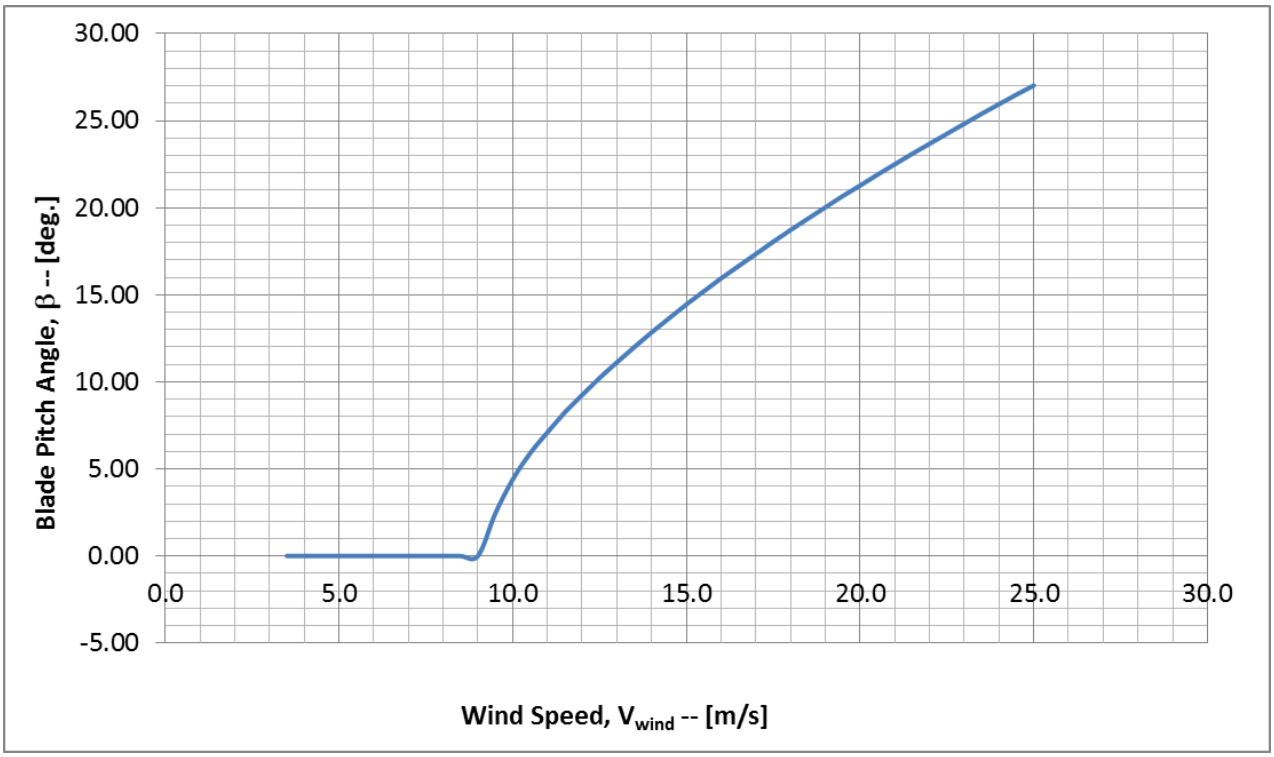

Figure 60. Blade Pitch Angle-Speed Schedule for 56m blade with IVG

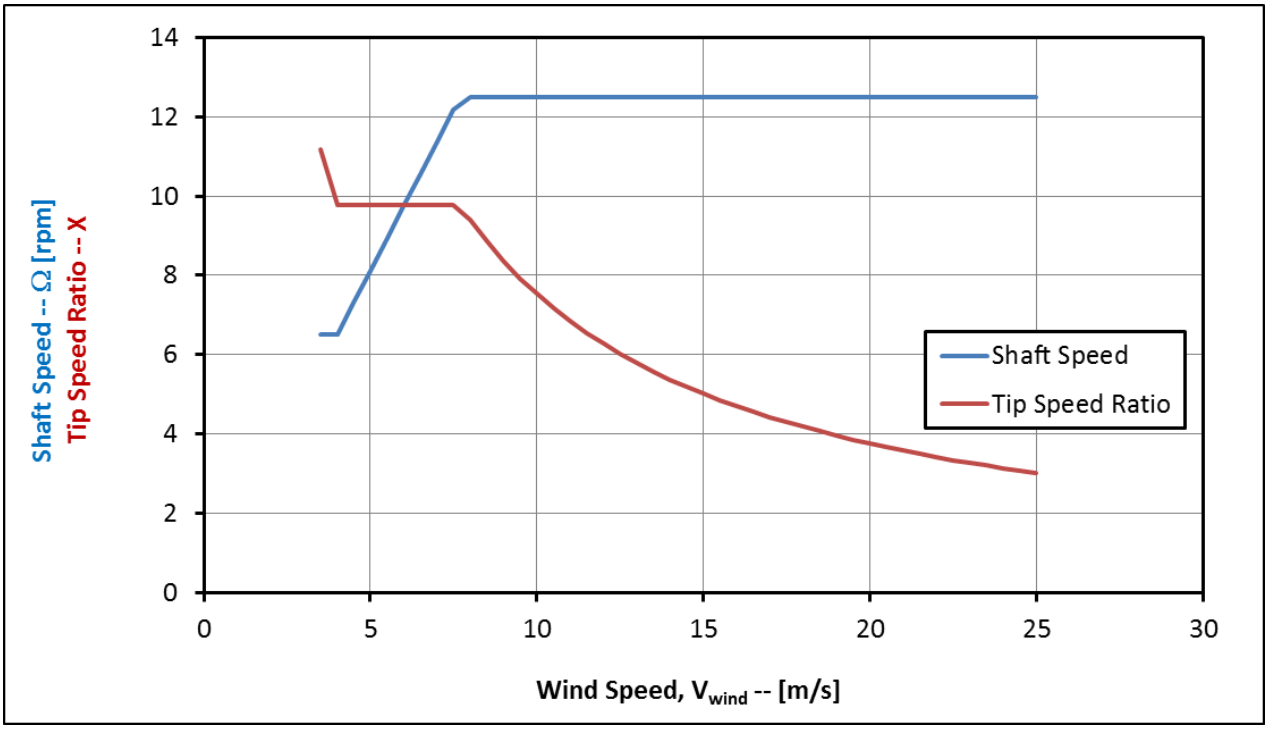

Figure 61. Shaft Speed Schedule and Tip Speed Ratio for the 56-m blade with IVG

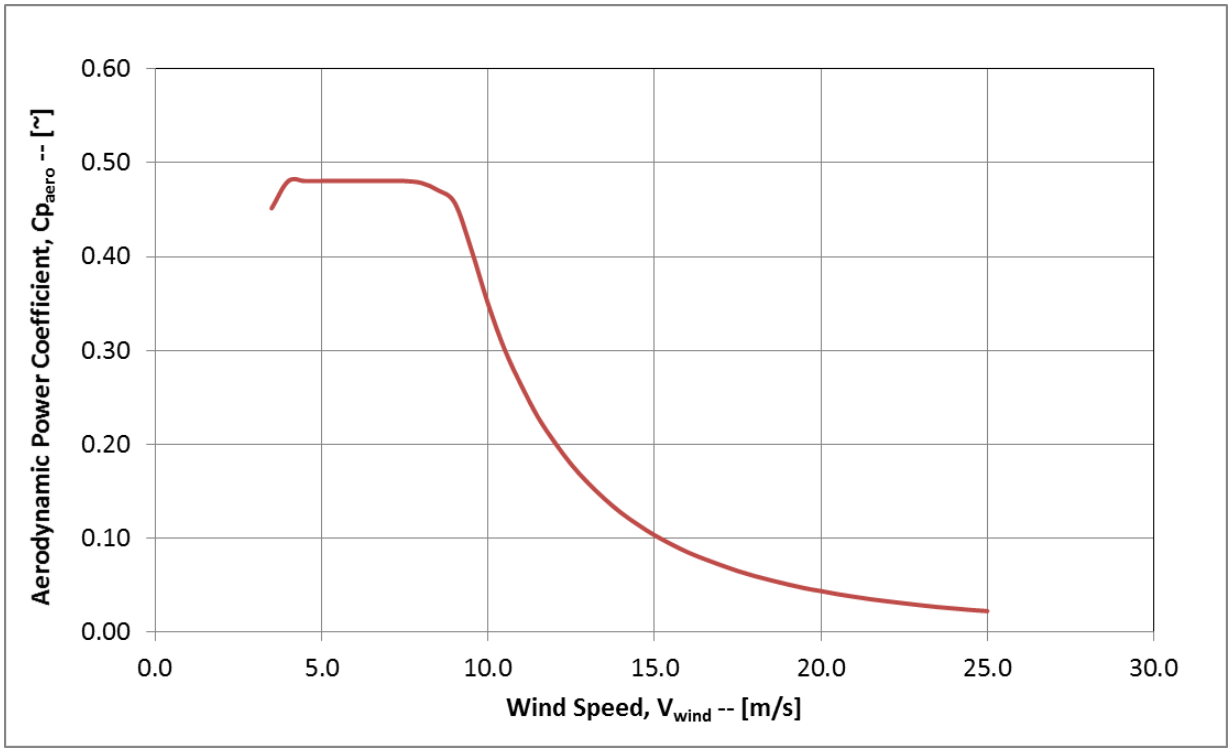

Figure 62. Aerodynamic Power Coefficient for 56-m blade with IVG

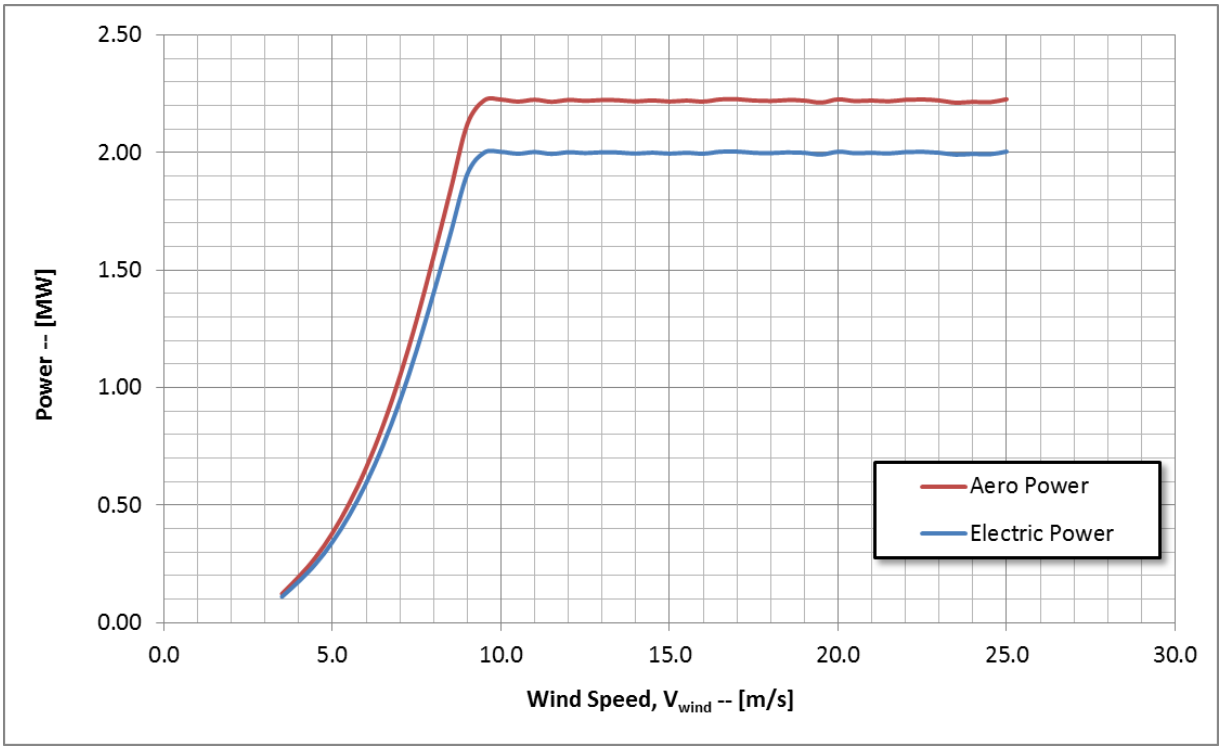

Figure 63. Power Curves for the 56-m blade with IVG

8.10. Loads Analysis and Structural Design – 56m blade with Integral Vortex Generators

The loads analysis is carried out using the analysis tool of the BladeOpt optimization tool. Using the analysis tool, a maximum blade root bending moment of 9591kNm. The highest load case resulted from DLC1.6 Extreme Operating Gust. Using the spanwise load distribution provided in Table 30, the structural design is carried out. The total weight of the blade with integral vortex generators is 10.41 metric tons. The blade incorporates the same amount of prebend i.e. 1.5 m as seen in the original blade design. A breakdown of the mass is provided in Table 31. As seen in Table 31, the mass of the girder is 3.17 tons, the shell skin weighs 3.6tons and shell core weighs 1.47 tons. These three components are the main weight contributors to the overall blade weight. The resin weight is estimated to be 2.22 tons. The blade uses glass fiber materials along with epoxy as a resin. The properties of these materials are provided in Table 32. It should be noted that further structural optimization along with full finite element analysis should be performed in order to create a certification based structural design. The need for a certification based design is out of the scope of this dissertation work and hence is not addressed as a part of this work.

It should be noted that the total blade mass is approximately the same as the clean baseline configuration. Also there has been an increase in loads which can be further reduced through controller tuning. Thus the integral vortex generator configuration provides increased performance as compared to the baseline clean configuration.

Table 30. Spanwise Loads Distribution

Z (m)	MX (kNm)	MY(kNm)
0.00	1259.52	9508.13
1.03	1214.58	9183.97
2.06	1169.63	8859.81
3.10	1125.18	8543.83
4.25	1086.15	8270.42
7.13	981.50	7566.62
10.00	844.32	6681.91
12.88	706.03	5825.90
15.75	572.09	5012.39
18.63	449.51	4246.84
21.50	347.45	3535.18
24.38	259.36	2886.12
27.25	186.27	2306.16
30.13	129.52	1797.43
33.00	85.08	1359.38
35.88	52.37	990.36
38.75	29.84	687.88
41.63	15.37	448.71
44.50	6.87	268.70
47.38	2.47	142.11
50.25	0.39	49.12
51.40	0.31	24.90
52.55	0.19	12.76
53.70	0.09	5.22
54.85	0.02	1.05
55.43	0.00	0.19
56.00	0.00	0.00

Table 31. Blade Weight Breakdown

Component	**Weight (kg)**
Shell Skin	3600.5
Shell Core	1470.1
WebSkin	441.2
WebCore	319.8
Girder	3172.7
TE Girder	69.5
Root Reinforcement	622.7
Paint	156.1
Adhesive	560
Resin	2221.6
Total	10412.6

*Resin mass is ~~already~~ accounted for in each of the structural components.

Table 32. Material Properties

Component	Density (kg/m^3)
ShellSkin	1924
ShellCore	300
WebSkin	1924
Webcore	100
Girder	1947
TE Girder	1947
RootInfo	1924
Adhesive	1200
Paint	1200

9. Conclusions and Recommendations for Future Work

As a part of this dissertation, the impact on aerodynamic performance, loads and cost using integral vortex generators on wind turbine blade designs is studied. In order to investigate the possibility of this new design space, a multi-disciplinary optimization analysis is carried out. To perform the optimization analysis, an aero-structural optimization routine is created. Three configurations are designed and as a part of this dissertation. The first configuration consisted of a baseline blade that spans 56m in length. The AEP associated with this baseline blade is 9165MWhr. No vortex generators are included in this baseline blade design. In order to determine the effectiveness of vortex generators on airfoils used on the 56m blade design, a verification and validation study of CFD tools is carried out. For this exercise, the LS(1)-0417MOD airfoil is used. STAR CCM+ software is used for performing the CFD analysis on the clean and vortex generator configurations of the LS(1)-0417MOD airfoil. Satisfactory aerodynamic results are obtained from the CFD analysis. A CFD analysis of a 47% thick airfoil and NACA63621 airfoil with vortex generators is performed as well. This data is then used to evaluate the improvement of aerodynamic performance of the add-on, 56-m blade configuration. Vortex generators are incorporated in the post design phase of the clean 56m blade design and the improvement in performance in recorded. It is observed that a 0.4% improvement in AEP along with a 1.2% increase in loads and 2.13% increase in cost of energy is achieved. Thereafter, the optimization and design of the 56m blade with integral vortex generators is carried out. As a part of this optimization and design, two configurations are studied namely – Single Vortex Generator configuration and Double Vortex Generator configuration. The single vortex generator configuration consists of vortex generators used only in the transition region of the blade whereas the double vortex

generator configuration consists of VGs used in the transition as well as outboard regions of the blade. Upon evaluating the single VG and double VG configuration, it is observed that the single VG configuration offers an increased performance as compared to the clean and double vortex generator configuration. Finally a full blade design of the 56m blade with integral vortex generators is carried out and the key performance metrics are recorded. A comparison of the three blade configurations is provided in Table 33.

Table 33. Comparison of 56m Blade Design Configurations with and without VGs

	Performance Metrics				Compared to Baseline Configuration			
Blade Name	AEP (MWhr)	Mxy (kNm)	COE ($/MWhr)	Blade Mass (kg)	AEP (MWhr)	Mxy (kNm)	COE ($/MWhr)	Blade Mass (kg)
Clean 56m Blade Design	9165	8317	37.57	10205				
Add-on VG 56m Blade Design	9200	8417	38.37	10205	0.38%	1.20%	2.13%	0.00%
Integral VG 56m Blade Design	9320	9592	36.45	10412	1.69%	15.33%	-2.98%	2.03%

As seen in the table above, the Integral VG design improves the performance by 1.7% but also results in a 15% increase in blade root bending moment. It should be noted that the cost of additional maintenance cost during the life cycle of the turbine specifically for reinstallation of vortex generators is not accounted for in the IVG case. The addition of such costs will affect the cost of energy for the system. The Add-on VG configuration on the other hand increases the aerodynamic performance only by 0.4% with a 1.2% increase in loads. This configuration however does not prove feasible from an economic standpoint. The impact of full dynamic extreme and fatigue loads is recommended as future work.

References

[1] Renewable Energy, Wikipedia – The Free Encyclopedia, Wikimedia Foundation Inc Website: http://en.wikipedia.org/wiki/Renewable_energy

[2] IEA World Energy Outlook Report 2011, International Energy Agency Webiste: http://www.iea.org/weo/

[3] Burton, T.; Sharpe, D.; Jenkins, N.; Bossanyi, E.; "Wind Energy Handbook", Wiley Publications, John Wiley & Sons, Inc., Danvers, MA, 2009.

[4] Manwell, J.; McGowan, J.; Rogers, A.; "Wind Energy Explained – Theory, Design and Application", Wiley Publications, John Wiley & Sons, Inc., Danvers, MA, 2002.

[5] Renewable Wind, Energy Kids, US Energy Information Administration Website: http://www.eia.gov/kids/energy.cfm?page=wind_home-basics

[6] Global Wind Energy Council Website: http://www.gwec.net/index.php?id=21

[7] Gad-el-Hak M, Bushnell DM. Separation control: review. J Fluids Eng 1991; 113:5–30.

[8] Wind Turbine Sizes, Access Science, McGraw Hill, Website: http://accessscience.com/loadBinary.aspx?aID=6581&filename=YB021005FG0040.gif

[9] CFD- Wiki, CFD Online Forums Website: http://www.cfd-online.com/Wiki/Main_Page

[10] Ning, S.Andrew, Objectives and Constraints for Wind Turbine Optimization, National Renewable Energy Laboratory, Internal Presentation, January 2013.

[11] Xudong, W., et.al.; Shape optimization of wind turbine blades, Journal of Wind Energy, Page no. 781 - 803 · April 2009

[12] Eke, G.B., Onyewudiala, J.I.; Optimization of Wind Turbine Blades Using Genetic Algorithm, Global Journal of Researches in Engineering, Vol. 10, Issue 7, December 2010

[13] McCosker, J.; Design and Optimization of a Small Wind Turbine, ME Mechanical Engineering Report, Rensselaer Polytechnic Institute Hartford, Connecticut, December 2012

[14] Private conversation with J. Nader, Director of Blade Technology, Siemens Wind Energy Corporation, September 2015.

[15] Chang PK; Control of flow separation, Washington, DC:Hemisphere Publishing Corporation, 1976.

[16] Taylor HD; The elimination of diffuser separation by Vortex generators. United Aircraft Corporation Report No. R-4012-3, June 1947.

[17] Bragg MB, Gregorek GM; Experimental study of airfoil performance with vortex generators, Journal of Aircraft 1987; 24(5):305-9.

[18] Calarese W, Crisler WP, Gustsfson GL. Afterbody drag reduction by vortex generator s. AIAA paper 85-0354, AIAA 23rd Aerospace Sciences Meeting, Reno, NV, January 14–17, 1985.

[19] Brown AC, Nawrocki HF, Paley PN. Subsonic diffusers designed integrally with vortex generators. Journal of Aircraft 1968; 5(3):221–9.

[20] Rao DM, Kariya TT. Boundary-layer submerged vortex generators for separation control—an exploratory study, AIAA Paper 88-3546-CP, AIAA/ASME/SIAM/APS 1st National Fluid Dynamics Congress, Cincinnati, OH, July 25–28, 1988.

[21] Lin JC, Selby GV, Howard FG.; Exploratory study of vortex-generating devices for turbulent flow separation control; AIAA Paper 91-0042, AIAA 29th Aerospace Sciences Meeting, Reno, NV, January 7-10, 1991.

[22] Lin JC.; Control of turbulent boundary-layer separation using micro-vortex generators. AIAA Paper 99-3404, 30th AIAA Fluid Dynamics Conference, Norfolk, VA, June 28–July 1, 1999.

[23] Jenkins L, Gorton SA, Anders S.; Flow control device evaluation for an internal flow with an adverse pressure gradient; AIAA Paper 2002-0266, 40th AIAA Aerospace Sciences Meeting and Exhibit, Reno, NV, January 14–17, 2002.

[24] Ashill PR, Fulker JL, Hackett, KC. Research at DERA on sub boundary layer vortex generators (SBVGs), AIAA Paper 2001-0887, 39th AIAA Aerospace Sciences Meeting and Exhibit, Reno, NV, January 8–11, 2001.

[25] Yao C-S, Lin JC, Allan BG. Flowfield measurement of device-induced embedded streamwise vortex on a flat plate. AIAA Paper 2002-3162, 1st AIAA Flow Control Conference, St. Louis, MO, June 24–27, 2002.

[26] Kerho M, Hutcherson S, Blackwelder RF, Liebeck RH.; Vortex generators used to control laminar separation bubbles. Journal of Aircraft 1993;30(3):315–9.

[27] Lin JC, Robinson SK, McGhee RJ, Valarezo WO.; Separation control on high-lift airfoils via micro-vortex generators. Journal of Aircraft 1994;31(6):1317–23.

[28] Klausmeyer S, Papadakis M, Lin J. A flow physics study of vortex generators on a multi-element airfoil, AIAA Paper 96-0548, 34th AIAA Aerospace Sciences Meeting and Exhibit, Reno, NV, January 15–18, 1996.

[29] Allan BG, Yao C-S, Lin JC; Numerical simulation of vortex generator vanes and jets, AIAA Paper 2002-3160, 1st AIAA Flow Control Conference, St. Louis, MO, June 24–27, 2002.

[30] Wetzel, KK.; Interactions of Riblets and Vortex Generators on a Flat Plate and Airfoil, Doctoral Dissertation, The University of Kansas, December 1995.

[31] Akbari, M.H., Price, S.J., 2003, Simulation of dynamic stall for a NACA0012 airfoil using a vortex method, Journal of Fluids and Structures, 17, 855-874.

[32] Theodorsen, T., 1979, General theory of aerodynamic instability and the mechanism of flutter, Report National Advisory Committee for Aeronautics, Report No 496.

[33] McCroskey, W.J., Some current research in unsteady fluid dynamics the 1976 freeman scholar lecture, Journal of Fluids Engineering, 8-39, Dec 1977.

[34] Ohmi, K., Coutanceau, M., Daube, O., Loc, T.P., 1991, Further experiments on vortex formation around and oscillating and translating airfoil at large incidences, Journal of Fluid Mechanics, 225, 607-630.

[35] Panda, J., Zaman, K.B.M.Q., 1994, Experimental investigation of the flow field of an oscillating airfoil and estimation of lift from wake surveys, Journal of Fluid Mechanics, 265, 65-95.

[36] Coton, F.N., Galbraith, R.A.M., JIang, D., and Gilmour., An experimental study of the effect of pitch rate on the dynamic stall of a finite wing, Royal Aeronautical Society, 17-18 July 1996.

[37] Carr, L.W., Progress in analysis and prediction of dynamic stall, AIAA, Atmospheric Flight Mechanics Conference, Snowmass, CO, August 19-21, 1985.

[38] Tuncer, I.H., Wu, J.C., Wang, C.M., 1990, Theoretical and numerical studies of oscillating airfoils, AIAA Journal, 28, Sept. 1990.

[39] Ekaterinaris, J.A., Menter, F.R., Computation of oscillating airfoil flows with one and two equation turbulence models, AIAA Journal, 28, (12), Dec. 1994.

[40] Barakos, G.N., Drikakis, D., Unsteady separated flows over maneuvering lifting surfaces, Phil. Trans. R. Soc. Ion. 358, 3279-3291, 2000.

[41] Mertes, C., et.al. ; A study of Flatback airfoils in Dynamic Motion, 49th AIAA Aerospace Sciences Meeting Including the New Horizons Forum and Aerospace Exposition, Orlando, Florida, 4-7 Jan 2011.

[42] Farokhi, S., Wetzel, K.; Influence of Vortex Generators on NREL S807 Airfoil Aerodynamic Characteristics and Wind Turbine Performance, Wind Engineering Journal, Volume 19, Number 3, September 1995, pp. 157-165.

[43] Farokhi, S., Barrett, R.; Subsonic Aerodynamics and Performance of Smart Vortex generators, AIAA Journal of Aircraft, Vol. 33, No. 2, March-April 1996.

[44] Farokhi, S., Propulsion System Design with Smart Vortex Generators, Aircraft Design Journal, pp. 127-143, 1999.

[45] Janiszewska, J., Three Dimensional Aerodynamics of a Simple Wing in Oscillation Including Effects of Vortex Generators, Doctoral Dissertation, Ohio State University, 2004.

[46] Farokhi, S., Cheng, G.; On Turbulent Flows Dominated By Curvature Effects, ASME Journal of Fluids Engineering, Vol. 114, March 1992, 52-57.

[47] Anderson, B.H., and Farokhi, S., "A Study of Three Dimensional Turbulent Boundary Layer Separation and Vortex Generator Control Using the Reduced Navier Stokes

Equations," Eighth Symposium on Turbulent Shear Flows, Munich, Germany, September 9 11, 1991.

[48] Farokhi, S., Aircraft Propulsion, 2nd Edition, John Wiley and Sons Ltd., Chichester, UK, May 2014

[49] Timmer, N., "Thick Airfoils for Wind Turbines – Wind Tunnel Test Data", Email Communication, Delft University of Technology, Netherlands, April 7, 2011.

[50] Dávila, C. G.; Camanho, P. P.; Failure Criteria for FRP Laminates in Plane Stress, NASA/TM-2003-212663, November 2003.

[51] Hermann, T.; Application of the Larc03 failure criterion to the analysis of wind turbine rotor blades, WEI Document 00.09.001, October 11, 2011.

[52] Buhl, M.; NWTC Design Codes (Modes), http://wind.nrel.gov/designcodes/preprocessors/modes/, Last modified May 26, 2005.

[53] Germanischer Lloyd, GH-Bladed Software Code, Version 4.5, 2015

[54] CD-Adapco, STAR CCM+ Fluid Flow Analysis Code, 2015

[55] Peric, M., et.al.; The advantage of polyhedral meshes, STAR CCM+ Fluid Flow Analysis Code, 2015

[56] CD-Adapco, Overset Mesh Tutorial, STAR CCM+ Fluid Flow Analysis Code, 2015

Appendix A: Additional Aerodynamic Simulation Data and Validation

A1. Pressure Distributions for LS(1)MOD0417 airfoil at different angles of attack

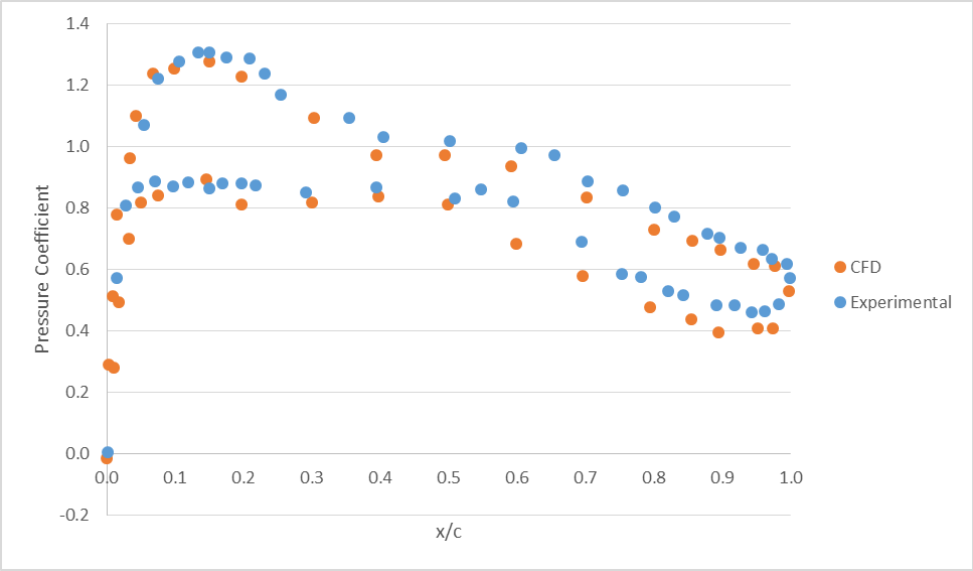

Figure 64. Cp distribution for angle of attack 0°

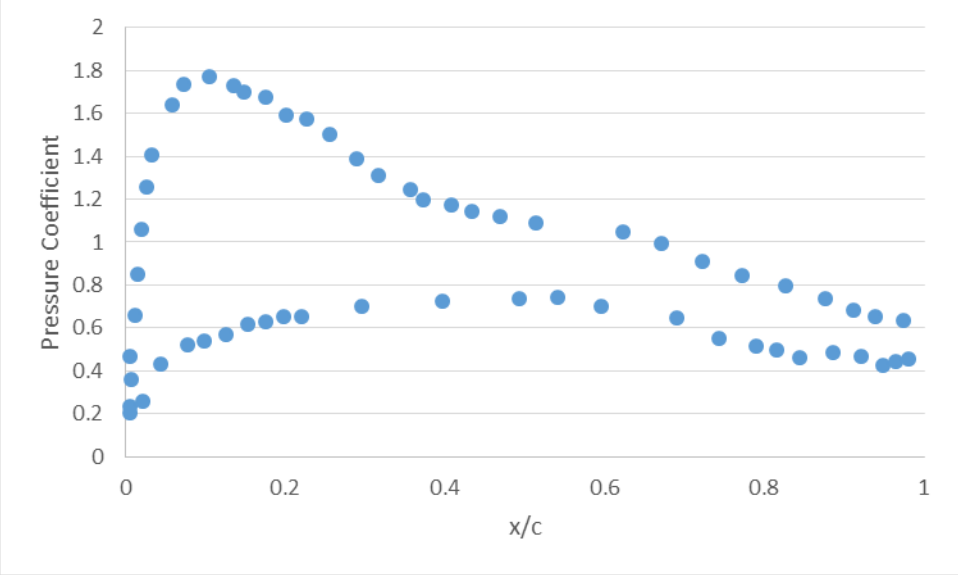

Figure 65. Cp distribution for angle of attack 4°

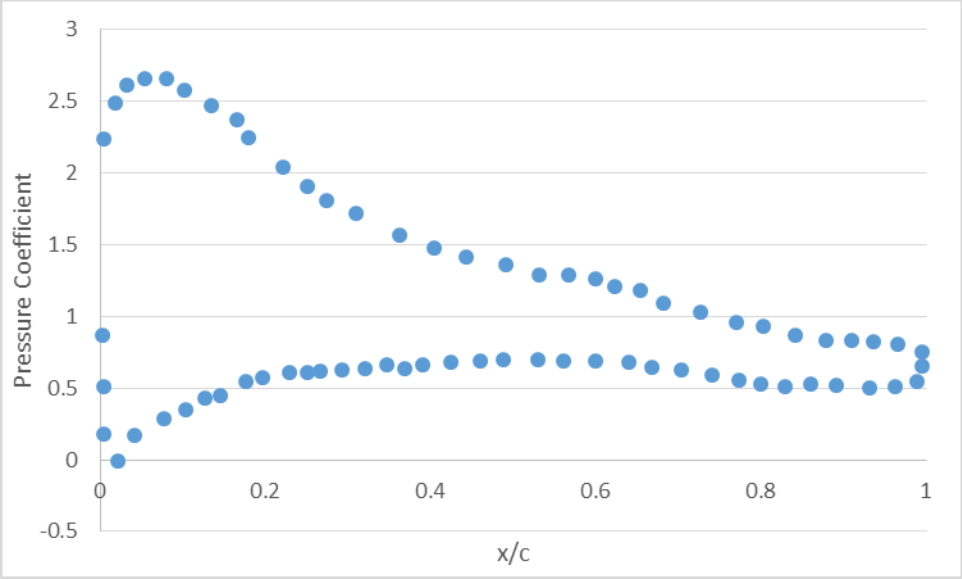

Figure 66. Cp distribution for angle of attack 8°

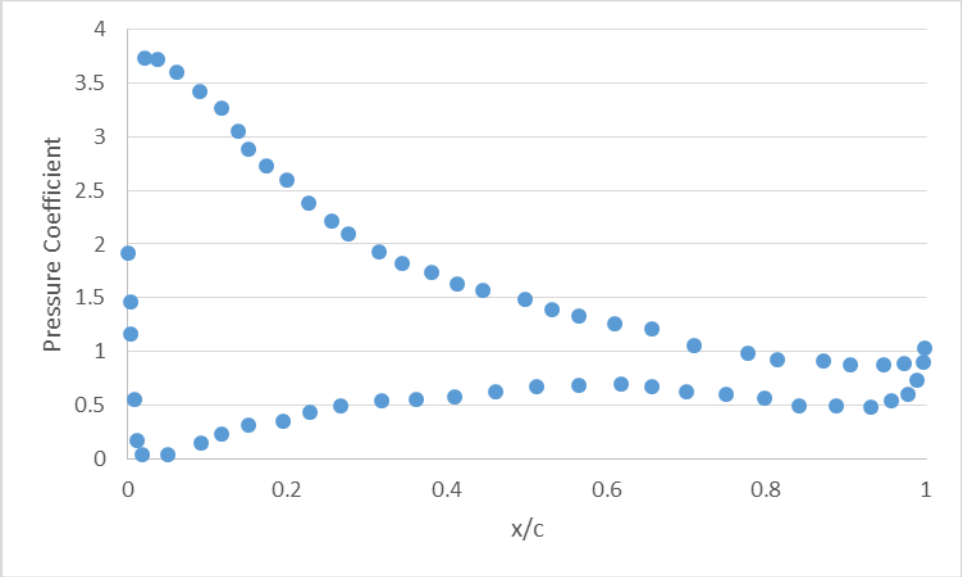

Figure 67. Cp distribution for angle of attack 12°

A2. Velocity distribution for LS(1)-0417MOD airfoil at different angles of attack

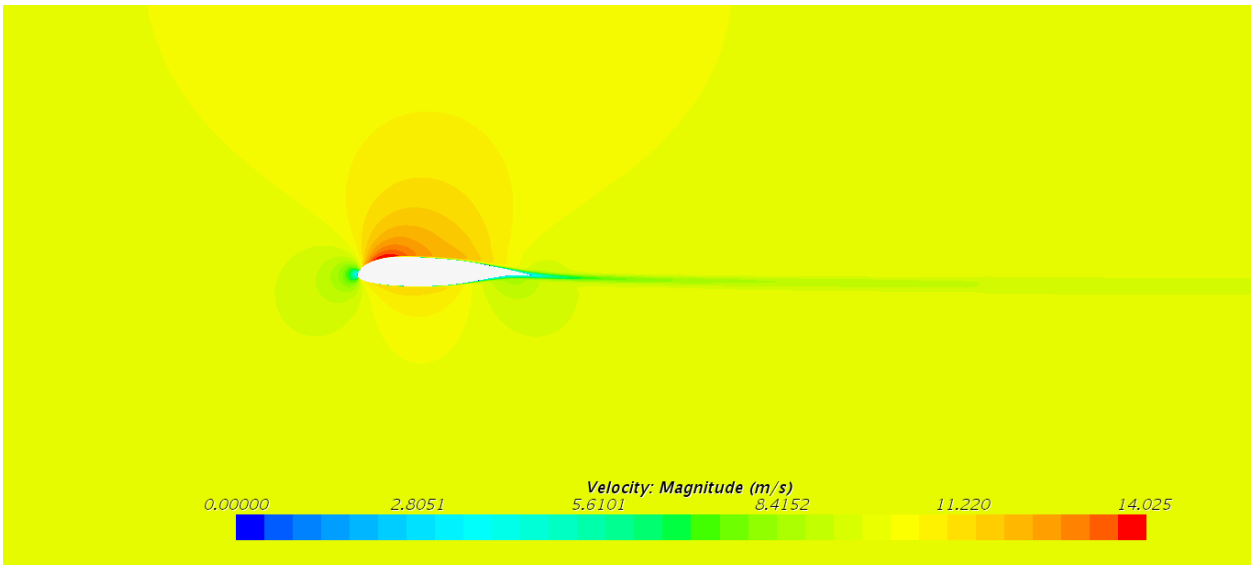

Figure 68. Velocity distribution for angle of attack 0°

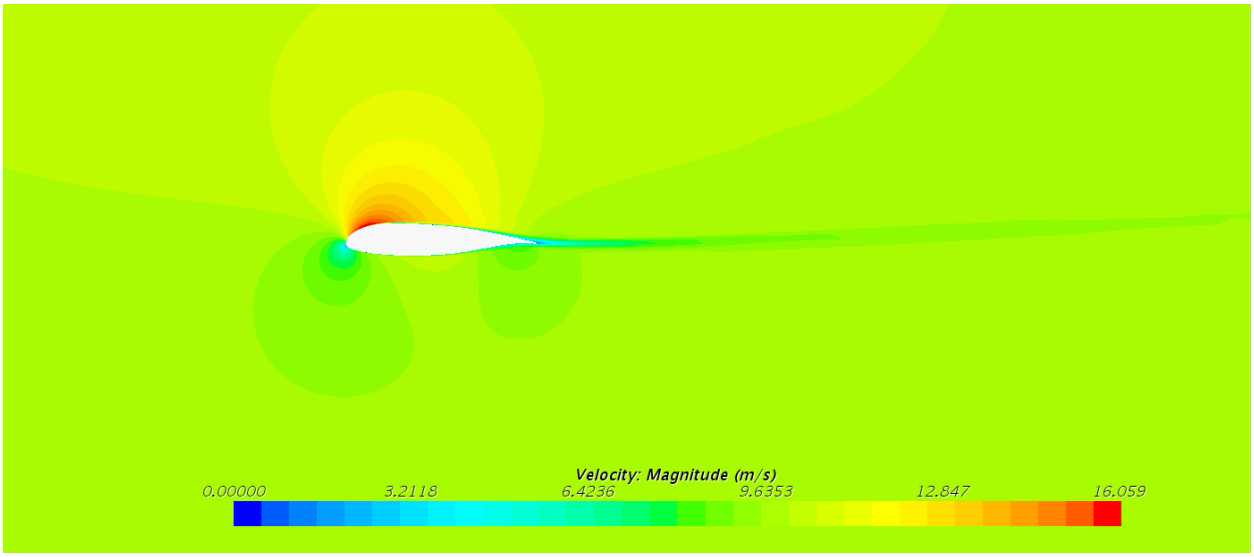

Figure 69. Velocity distribution for angle of attack 4°

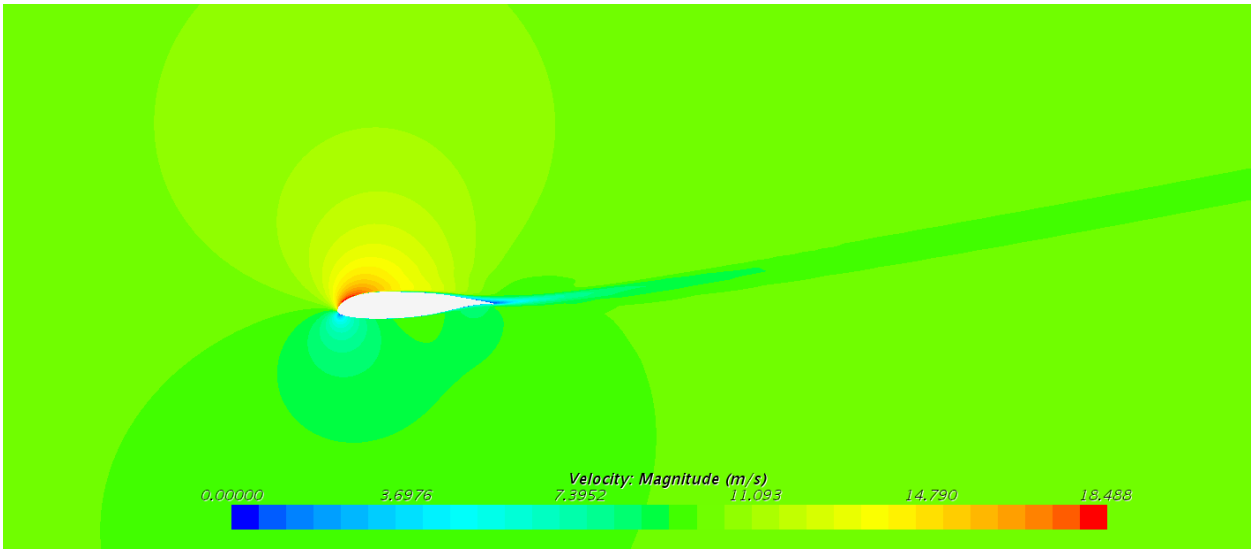

Figure 70. Velocity distribution for angle of attack 8°

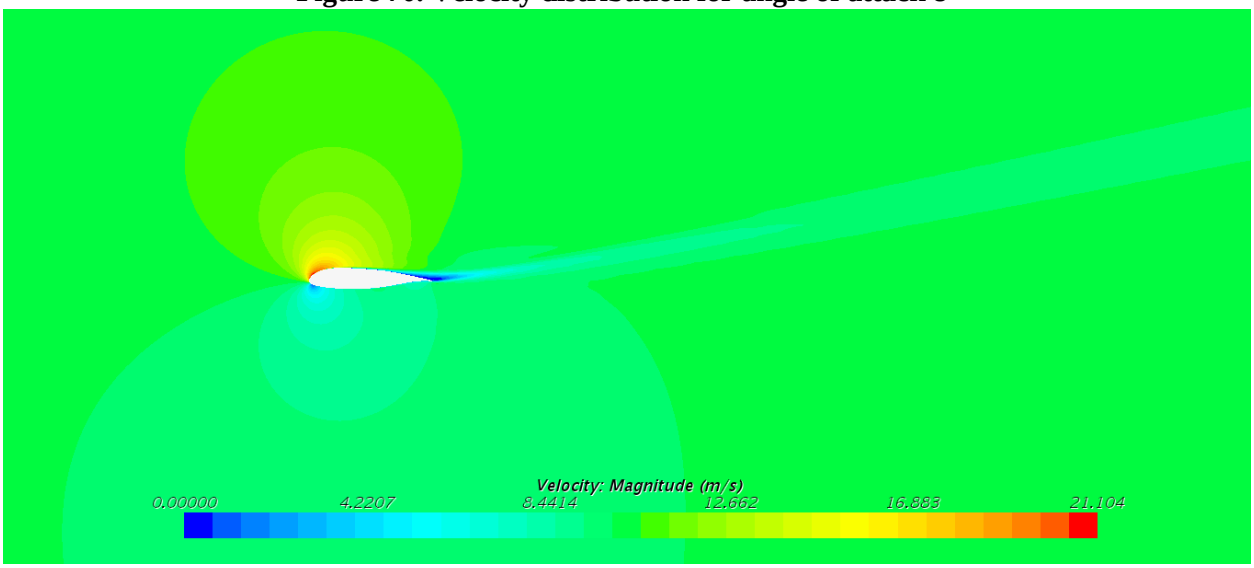

Figure 71. Velocity distribution for angle of attack 12°

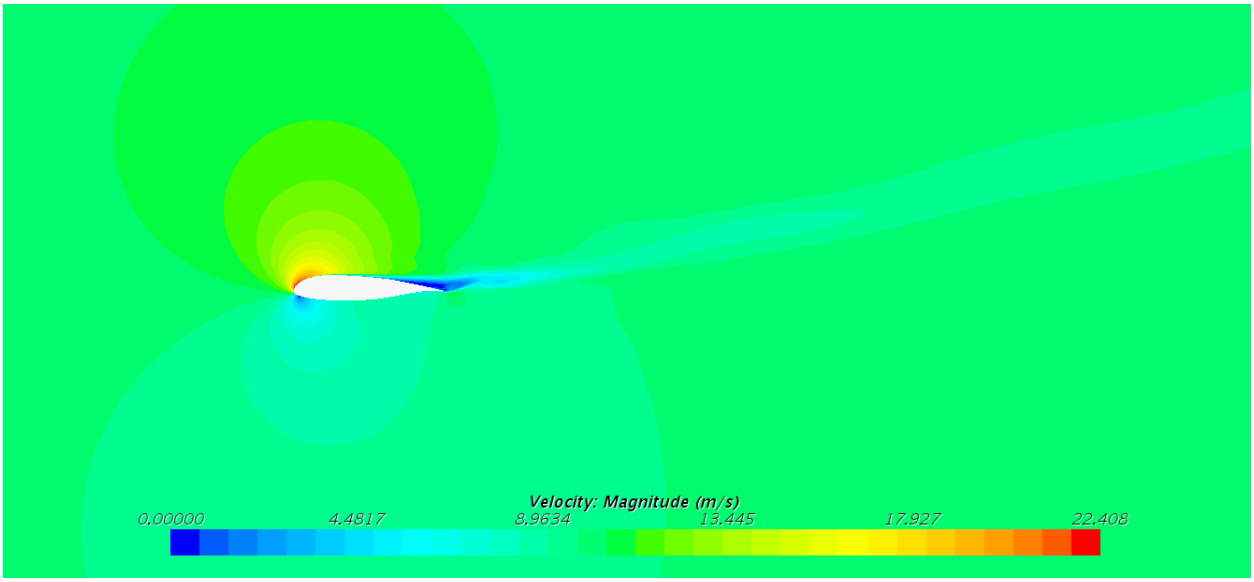

Figure 72. Velocity distribution for angle of attack 14°

A3. Pressure Distribution for NACA63621 airfoil with vortex generators at different angles of attack

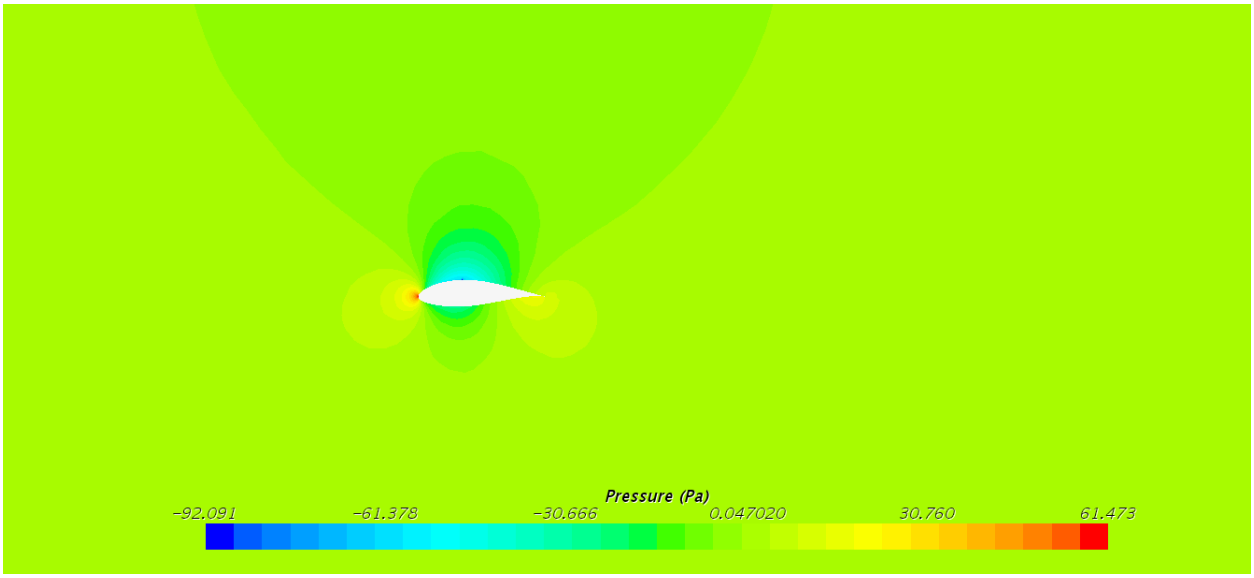

Figure 73. Pressure distribution for angle of attack 0°

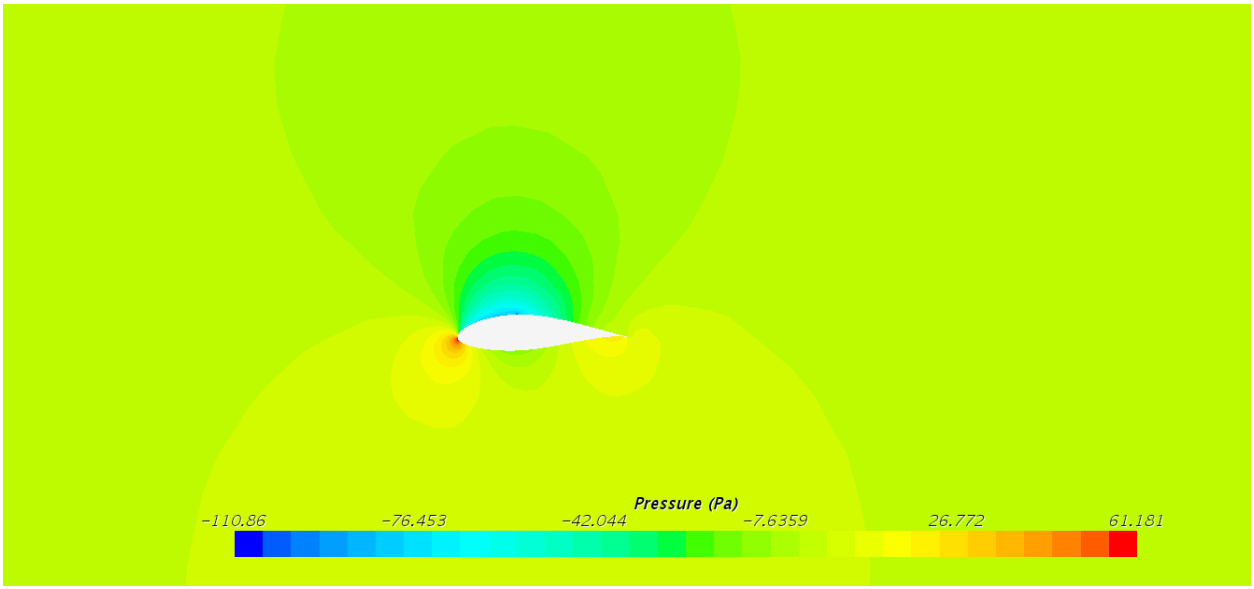

Figure 74. Pressure distribution for angle of attack 4°

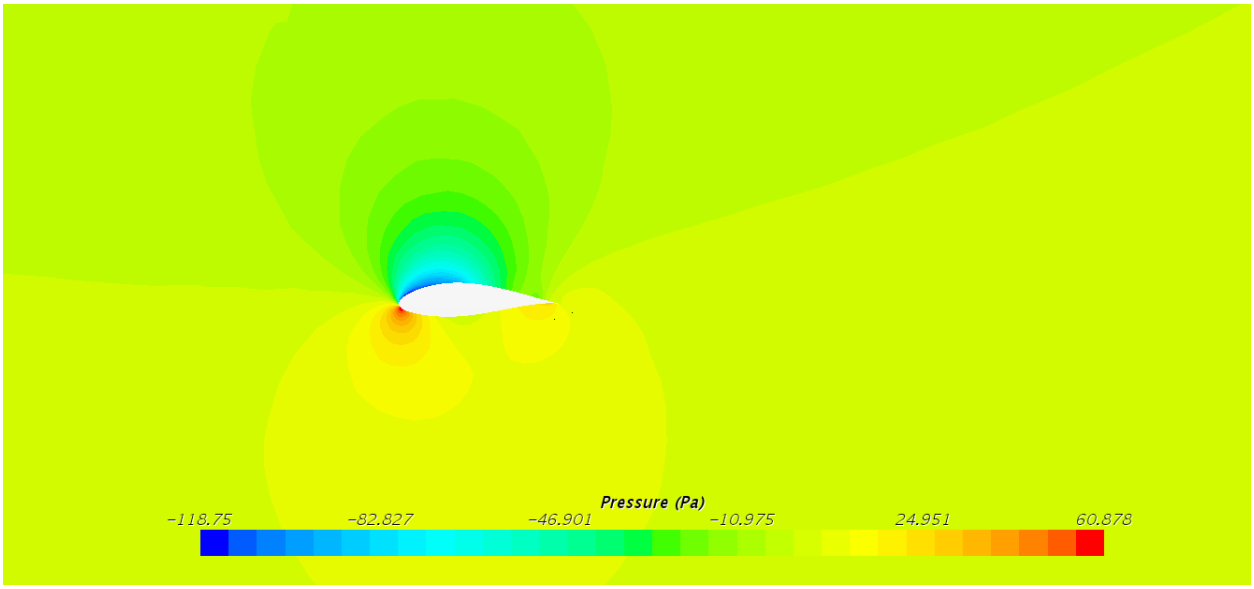

Figure 75. Pressure distribution for angle of attack 8°

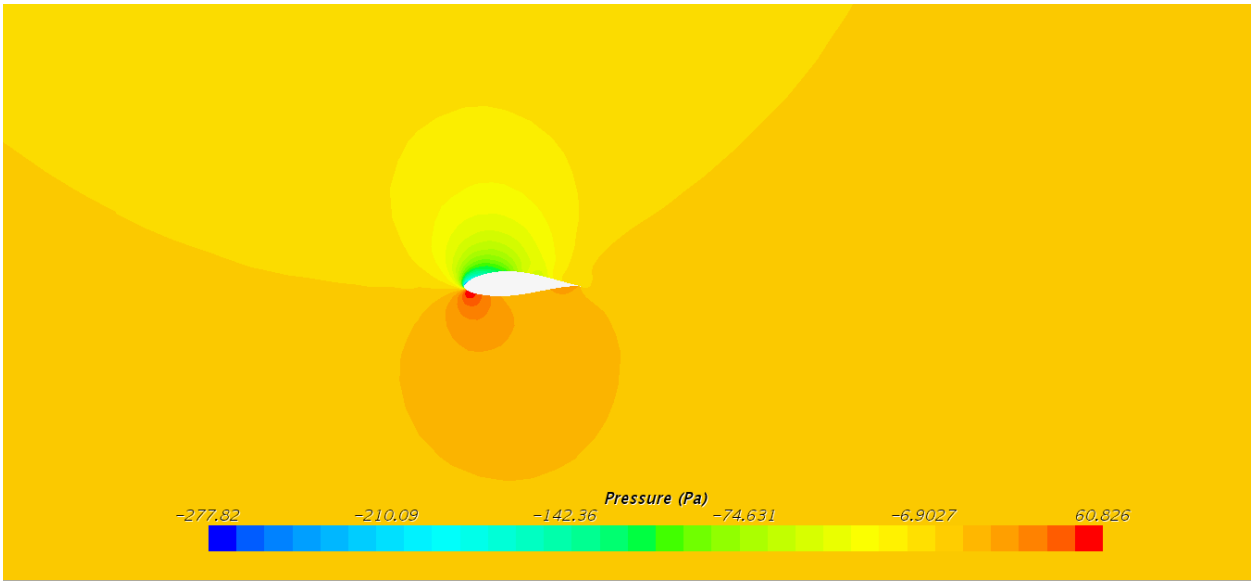

Figure 76. Pressure distribution for angle of attack 14°

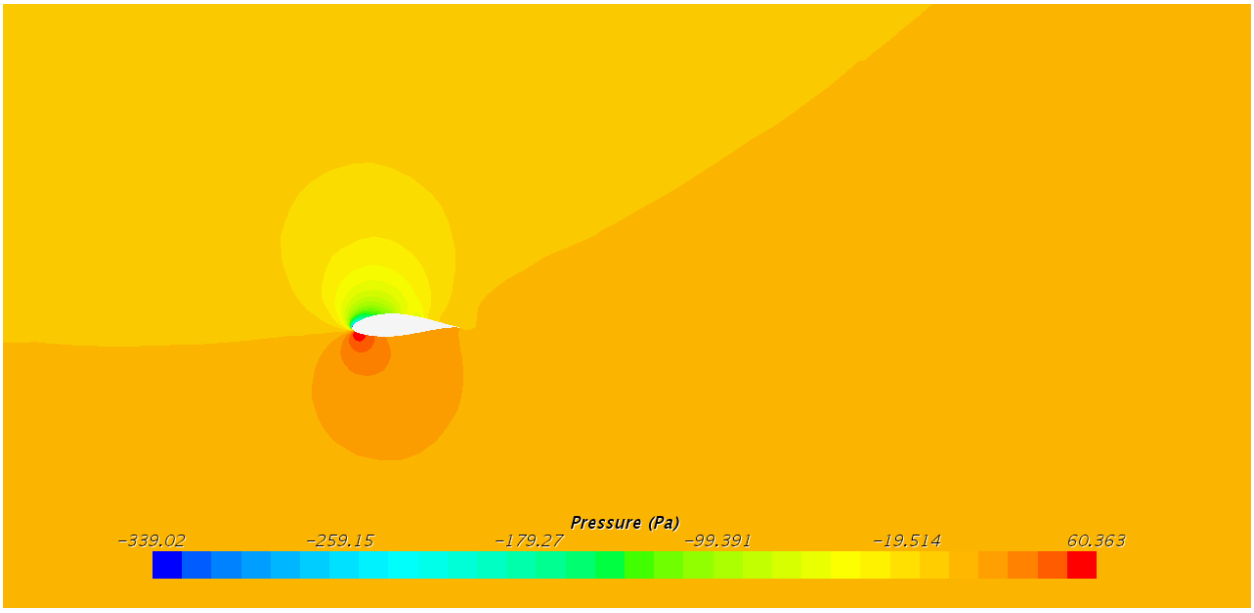

Figure 77. Pressure distribution for angle of attack 16°

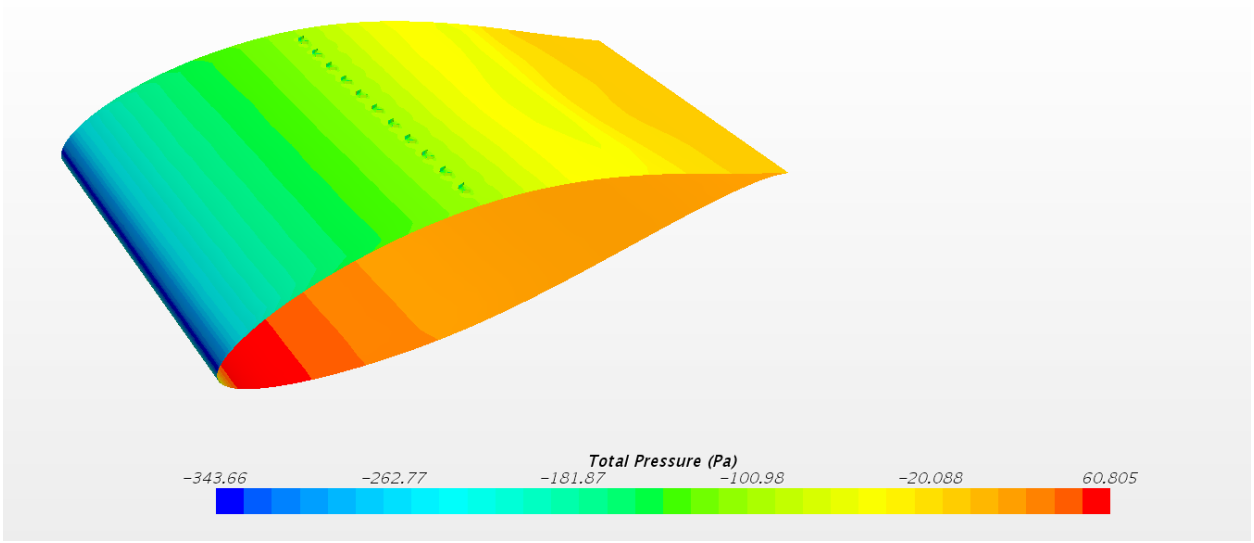

Figure 78. Pressure distribution (3D) for angle of attack 16°

A4. Velocity distribution for NACA63621 airfoil at different angles of attack

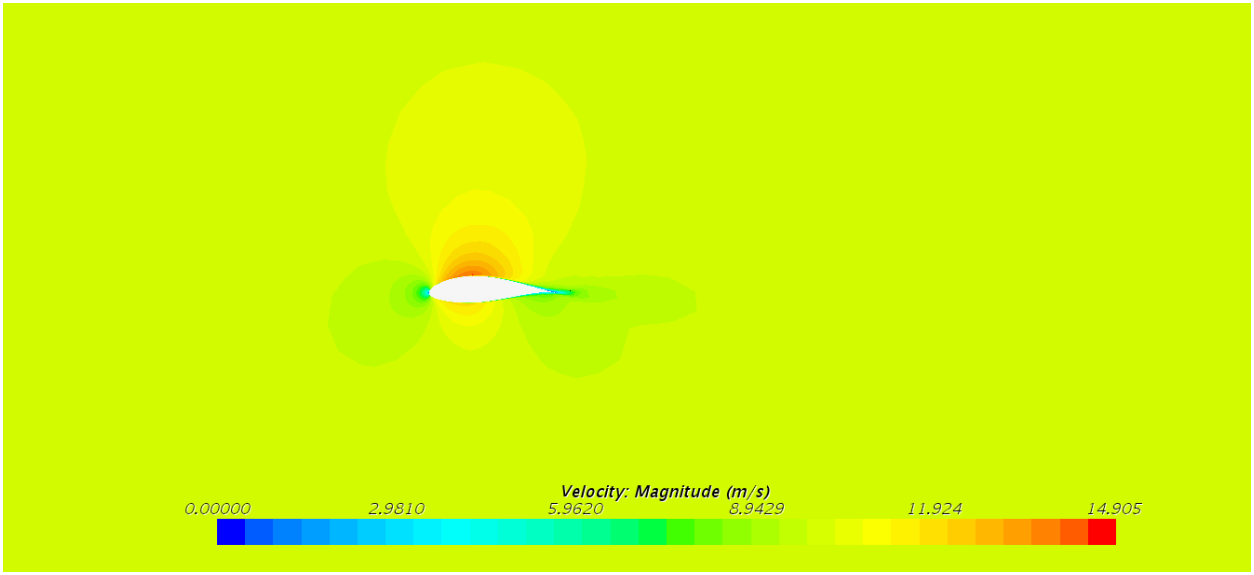

Figure 79. Velocity distribution for angle of attack 0°

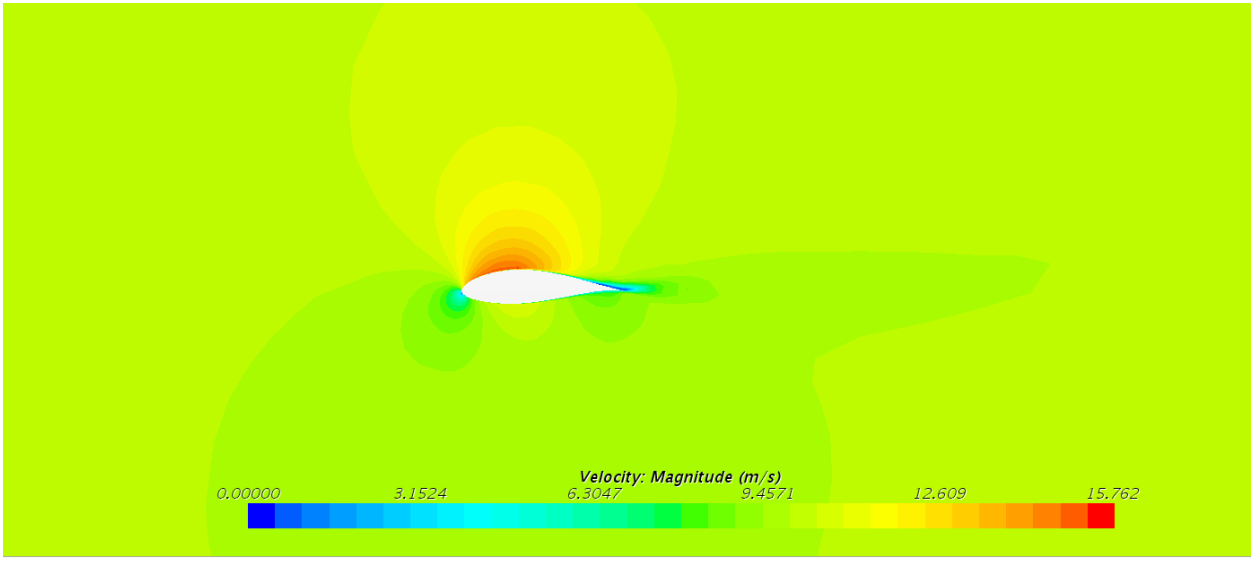

Figure 80. Velocity distribution for angle of attack 4°

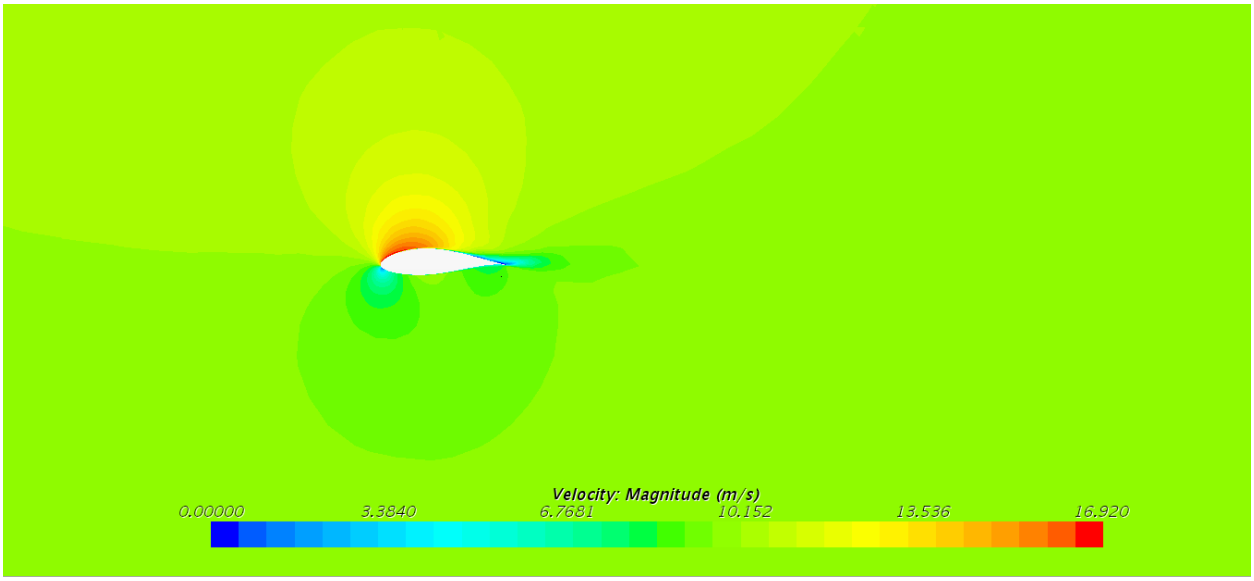

Figure 81. Velocity distribution for angle of attack 8°

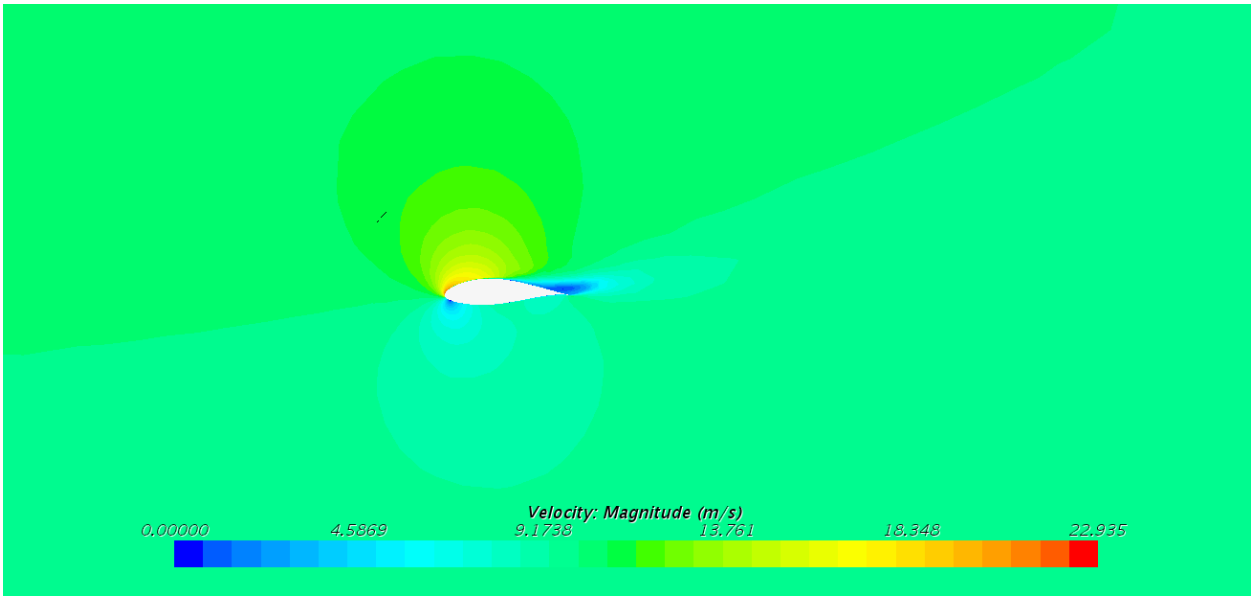

Figure 82. Velocity distribution for angle of attack 14°

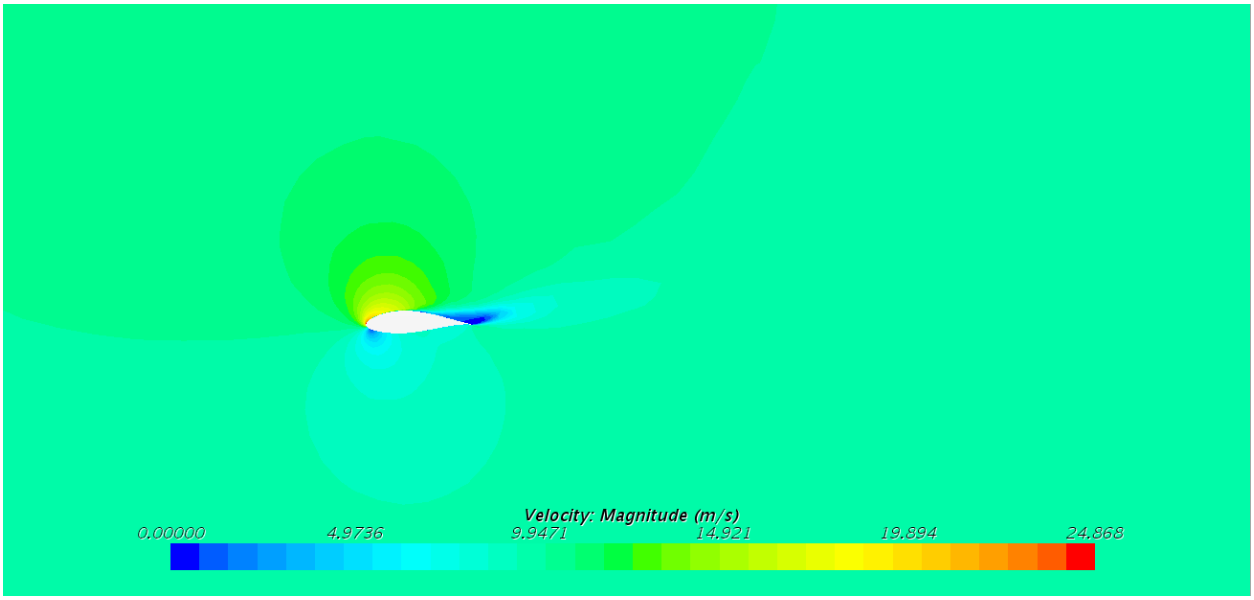

Figure 83. Velocity distribution for angle of attack 16°

A5. Pressure Distribution for FB47 airfoil with vortex generators at different angles of attack

Figure 84. Pressure distribution for angle of attack 0°

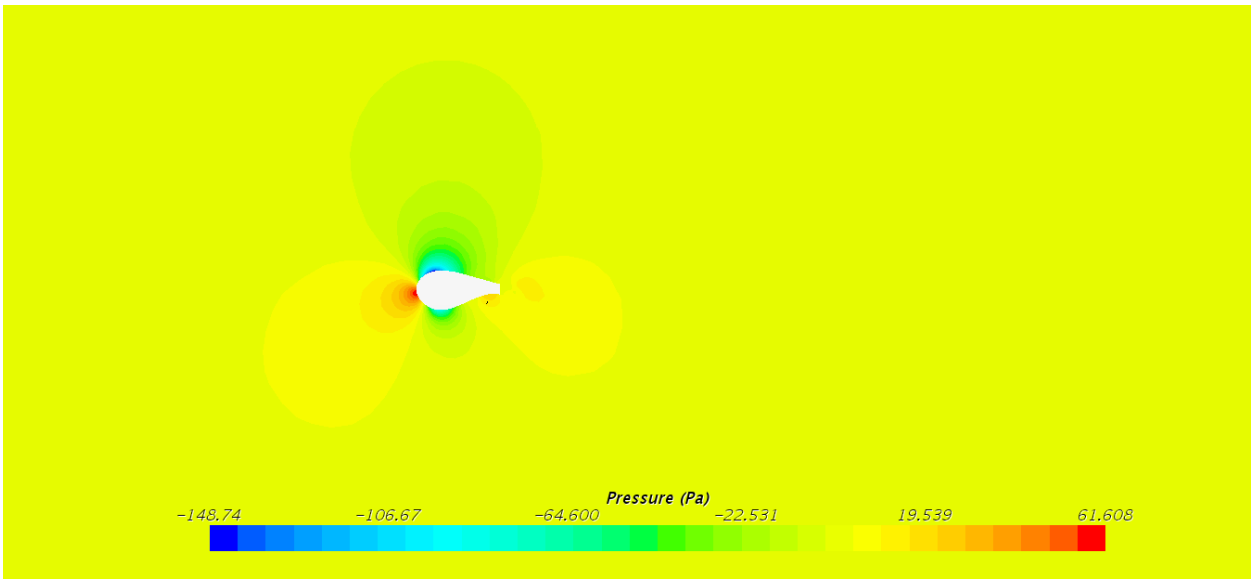

Figure 85. Pressure distribution for angle of attack 4°

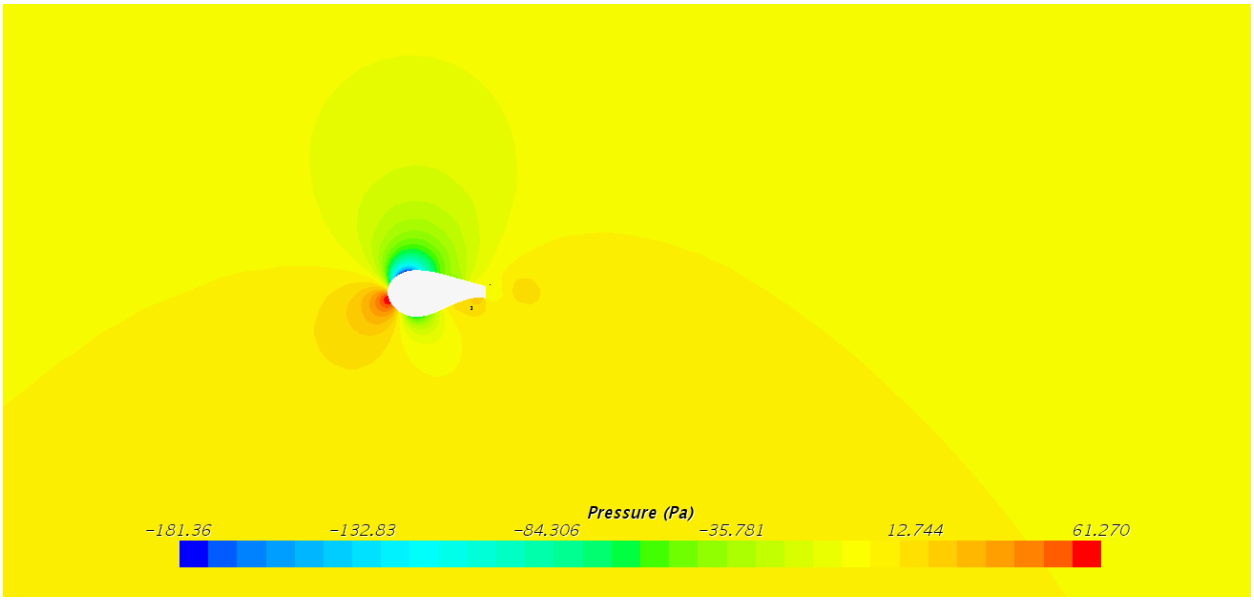

Figure 86. Pressure distribution for angle of attack 8°

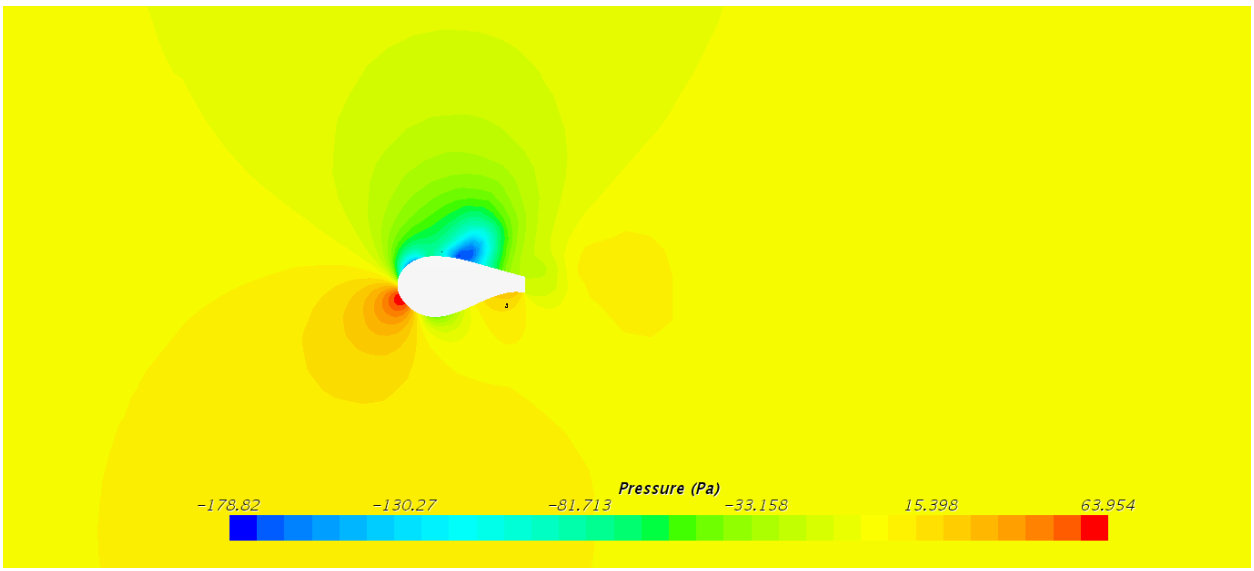

Figure 87. Pressure distribution for angle of attack 14°

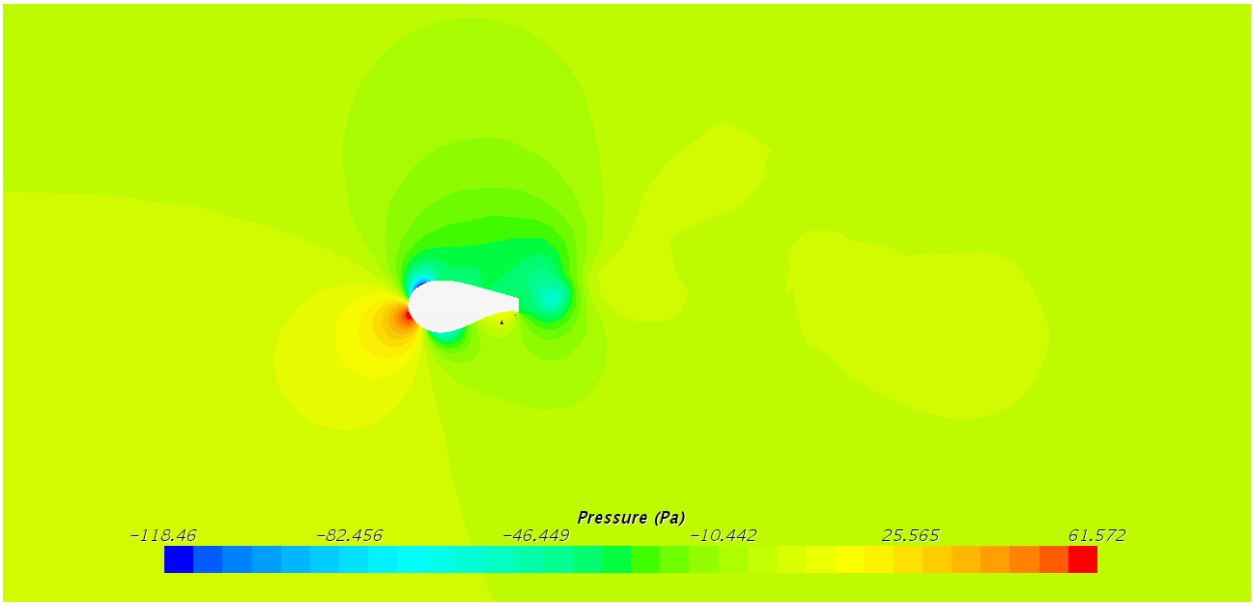

Figure 88. Pressure distribution for angle of attack 16°

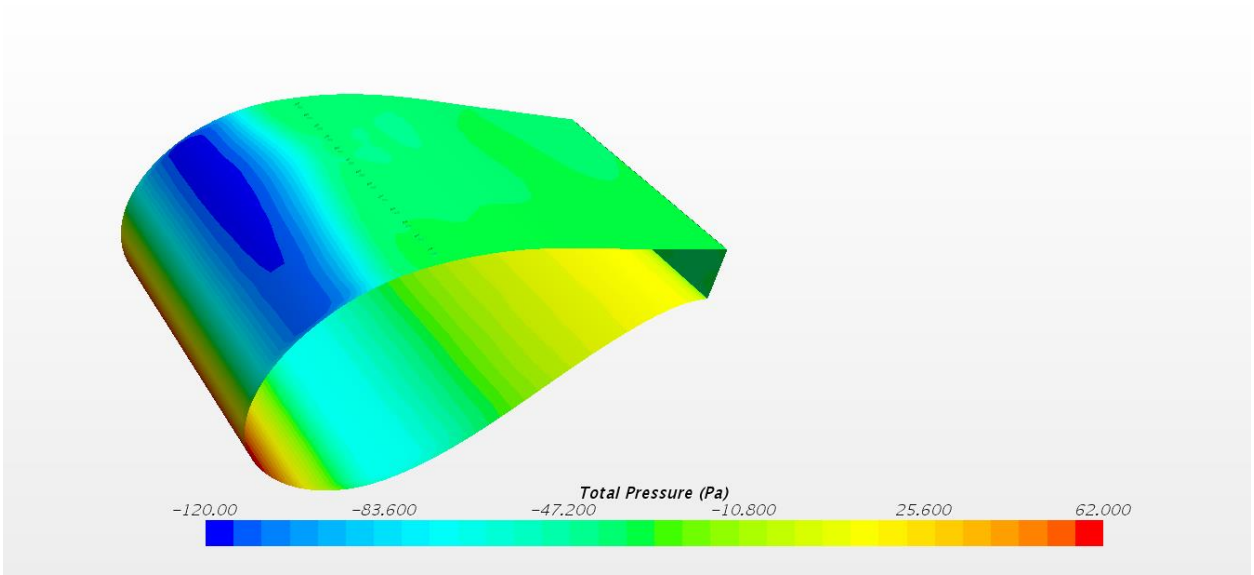

Figure 89. Pressure distribution (3D) for angle of attack 16°

A6. Velocity distribution for FB47 airfoil at different angles of attack

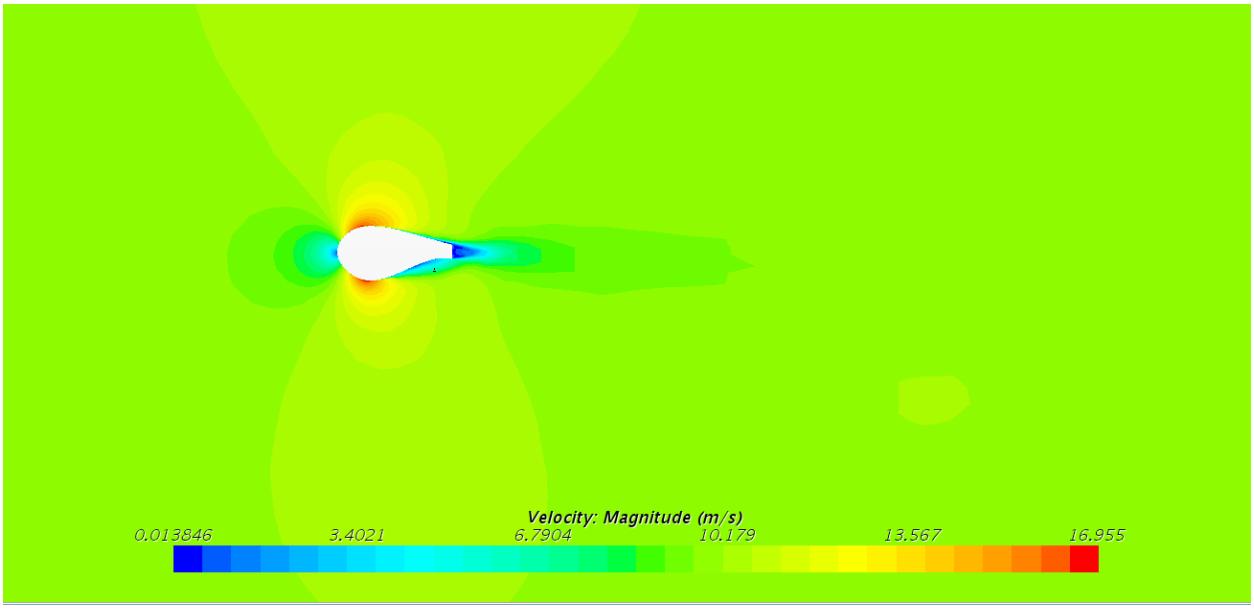

Figure 90. Velocity distribution for angle of attack 0°

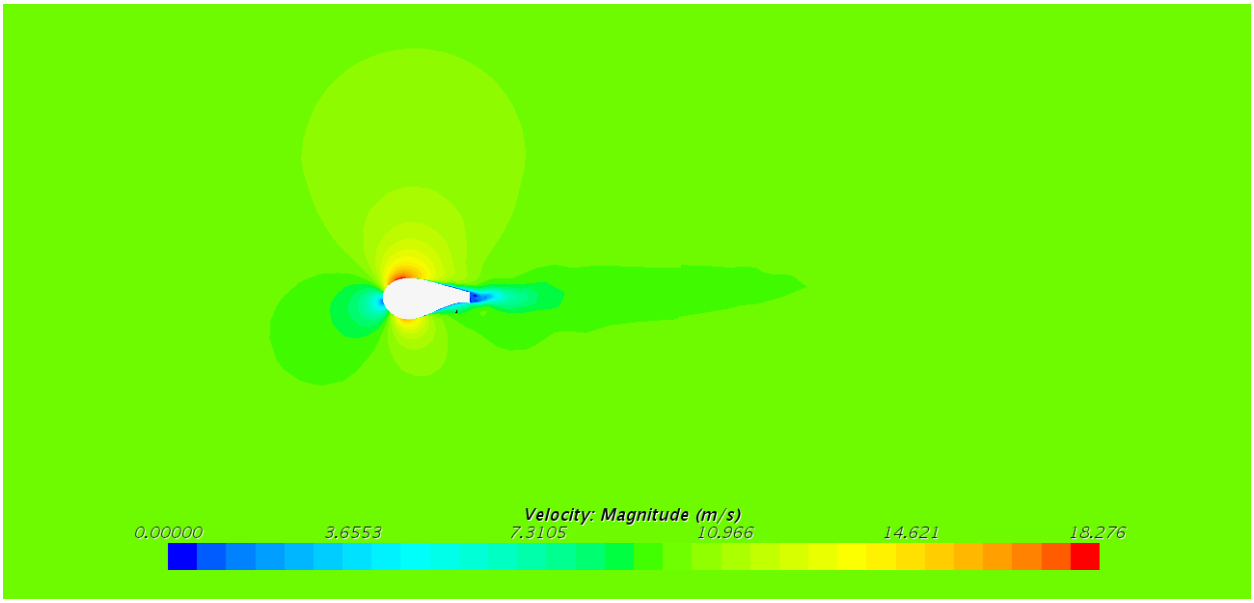

Figure 91. Velocity distribution for angle of attack 4°

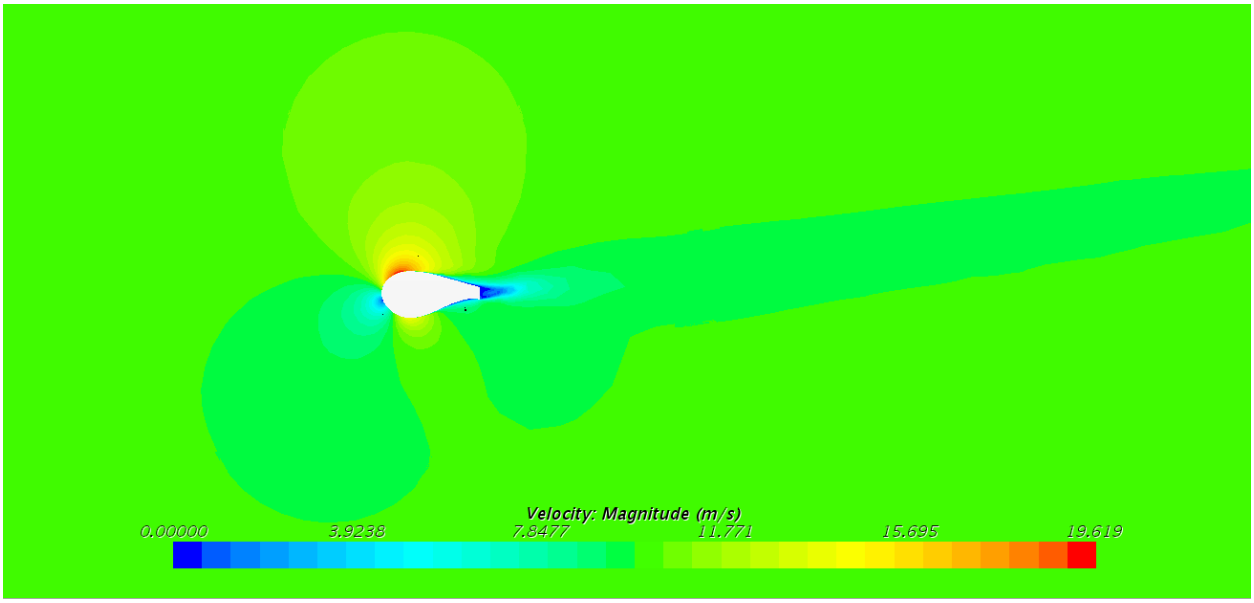

Figure 92. Velocity distribution for angle of attack 8°

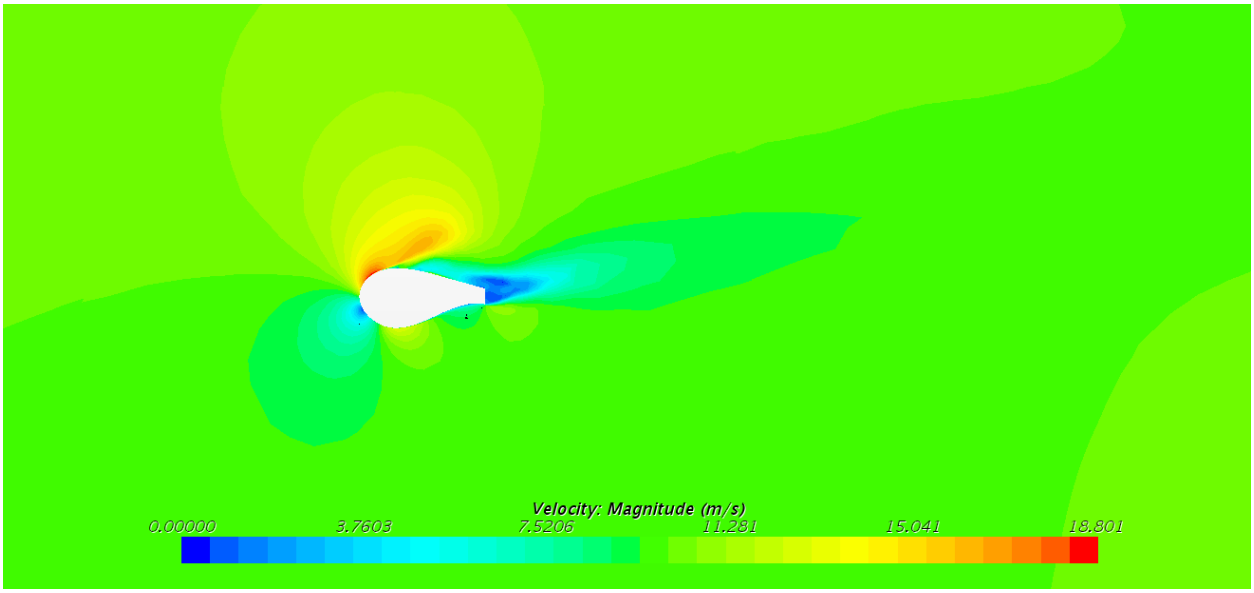

Figure 93. Velocity distribution for angle of attack 14°

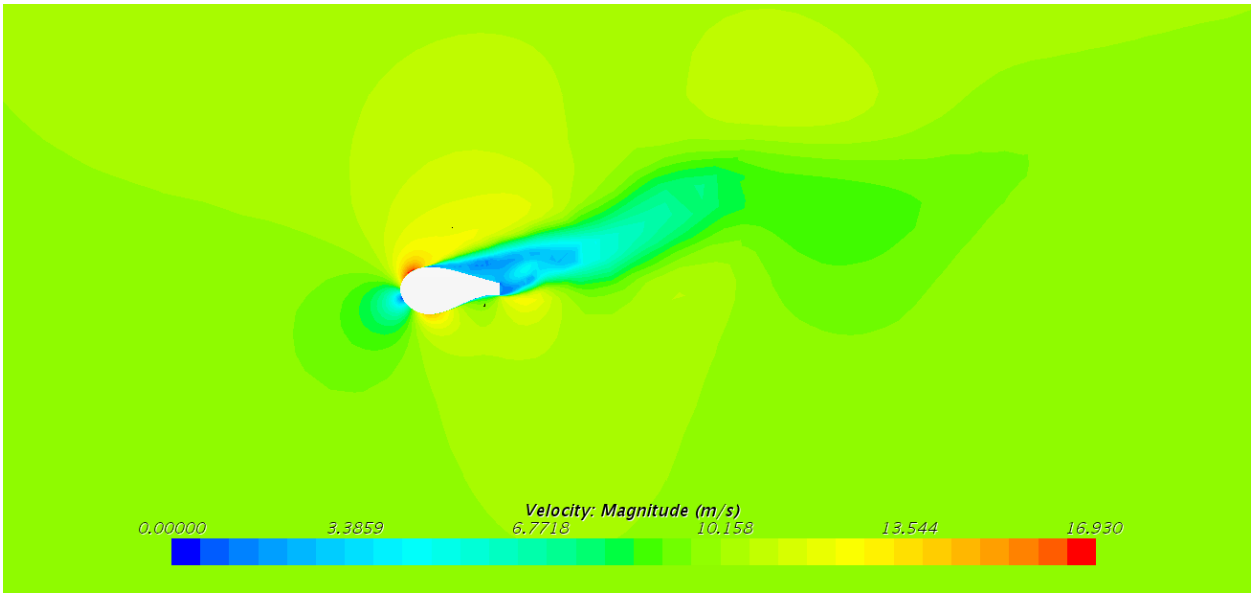

Figure 94. Velocity distribution for angle of attack 16°